RECEIVED
MAY 02 2000
OSTI

IS-T 1890

Wave Propagation in Ordered, Disordered, and Nonlinear Photonic Band Gap Materials

by

Lidorikis, Elefterios

PHD Thesis submitted to Iowa State University

Ames Laboratory, U.S. DOE

Iowa State University

Ames, Iowa 50011

Date Transmitted: December 10, 1999

PREPARED FOR THE U.S. DEPARTMENT OF ENERGY

UNDER CONTRACT NO. W-7405-Eng-82.

AVAILABILITY:

To DOE and DOE contractors: Office of Scientific and Technical Information
P.O. Box 62
Oak Ridge, TN 37831

prices available from: (615) 576-8401
FTS: 626-8401

To the public: National Technical Information Service
U.S. Department of Commerce
5285 Port Royal Road
Springfield, VA 22161

TABLE OF CONTENTS

CHAPTER 1. GENERAL INTRODUCTION

Our century is characterized by huge technological achievements, many of them being the result of understanding and controlling the electric conduction properties in materials. Ever since J. J. Thomson's discovery of the electron in 1897 and Drude's classical transport theory three years later, our technology continuously advanced with large steps, to today's modern telecommunication and digital computing world. Tailoring the conducting properties of semiconductors, which led to the transistor revolution in electronics, or the careful development of new alloys and ceramics, today's high-temperature superconductors, are among the most important examples of how materials are processed, or artificially created, in order to obtain the desired electric properties.

Over the last couple of decades, the need for more speed and bandwidth in the telecommunications and computer industry has turned researchers towards the search for ways to use light instead of electrons. Already, fiber-optic cables, lossless dielectric structures that simply guide light, have revolutionized the telecommunications industry and are in every day use. However, in order to replace the electrons with light, novel materials with optical properties similar to the electronic properties of the semiconductors would be needed; materials that would control the transmission of light, forbidding it for some frequencies, for all or some directions, thus perturbing the electromagnetic density of states. They should be able to be doped, creating donor and acceptor levels, and to localize light within them. What would be needed is materials with a "photonic band gap".

Photonic Band Gap (PBG) materials in one dimension are already in wide use. The familiar Bragg reflector is the basis for various devices, such as dielectric mirrors, Fabry-Perot filters, distributed feedback lasers etc. It consists of a periodic array of alternating layers of different dielectric constants. For light with the proper frequency and incidence angle, all waves reflected from different layers will interfere coherently, resulting in zero transmission. It wasn't however until 1987 when Yablonovitch at Bellcore Laboratories and John at Princeton University, suggested the existence of a complete, in all 4π directions, photonic band gap.

Electromagnetic waves in dielectric structures exhibiting three-dimensional periodicity will undergo multiple scattering if their wavelength is comparable to the lattice spacing. For some structures, due to coherent interference, there will be no propagating modes in any direction for a range of frequencies, giving rise to a photonic band gap. The physical picture is no different from the electronic case, where multiple scattering of the electrons from the periodic ionic potential gives rise to energy band gaps. For the band gap frequencies all states are completely suppressed, leading to a strong modification of the radiative dynamics inside the structure. New exciting possibilities have now opened: suppression of spontaneous emission from excited atoms inside the material; creation of high-Q microcavities when introducing defects or doping in the structure. It is worth noting that modification of the electromagnetic density of states may also be possible using metallic cavities, but not in the optical range due to absorption. The race was on, for the theorists to study these materials and obtain the optimal structure parameters, and for the experimentalists to construct them.

Photonic band gap structures can also be doped with nonlinear dielectric materials, i.e., materials having an intensity-dependent dielectric constant. The dynamic changes of the effective dielectric contrast inside the structure lead to a rich variety of exciting phenomena. Optical limiting, gap soliton formation, bistable and/or multistable input-output response are some of the most important features. Promising future novel applications include all-optical switches, logic gates, transistors, pulse shapers, as well as set-reset fast memory elements.

This dissertation aims to study two regimes of Photonic Band Gap materials. The first one focuses on the properties and dynamics of one-dimensional layered PBG structures doped with nonlinear material, while the second one focuses on the physical mechanisms that are behind the formation of the spectral gaps in two-dimensional Photonic Band Gap materials. In the next section we present an introduction to the literature, theoretical background, and numerical methods for photonic band gap materials, followed by a similar section for nonlinear optics in photonic band gap materials. Next, there is a small section stating the objectives that are fueling our work, followed by an preliminary introduction to the research effort that will be presented in the subsequent chapters.

Photonic band gap materials

The idea of a spectral gap is not new. It rather dates back to 1914, in the attempts to explain the observed large x-ray reflections in crystals and the development of the dynamical theory of x-ray diffraction [1, 2]. However, the observed gaps were very narrow and only along certain directions, due to the very small refractive index contrasts that x-rays effectively experience inside the crystal, and so the idea of a complete, in all directions, photonic band gap was never actually conceived, or at least never taken seriously enough.

The first suggestions for the possibility of a complete photonic band gap [1, 4, 5] in artificial dielectric structures exhibiting three-dimensional periodicity came in 1987, independently from Eli Yablonovitch at Bellcore labs [6] and Sajeev John at Princeton [7], each with a different motivation. Yablonovitch was looking for ways to control spontaneous emission. If the photon emitted by an excited atom inside a photonic band gap material fell inside the frequency gap, then spontaneous emission would be inhibited [8]. This opens many possibilities [9, 10, 11, 12]. Atoms or molecules inside a photonic band gap material could be locked into excited states. If one could tailor the frequency gap to overlap with the electronic band edge, then the electron-hole recombination process could be controlled in a photonic band gap material, enhancing the performance of semiconductor lasers or other solid state devices [6, 13, 14]. John on the other hand was interested in the possibility of observing Anderson localization for photons in a dielectric structure. The motivation for suggesting the photonic crystal was to strengthen his hypothesis that photon localization may occur in strongly scattering dielectrics; a photonic band gap can create strongly localized states of light.

Literature review

Yablovitch's actual initial idea was a three-dimensional analog of the distributed-feedback laser. In a distributed-feedback laser [15] the index of refraction is periodically modulated along the laser axis. Periodicity opens up a forbidden frequency gap for propagation perpendicular to the layers [16]. A small discontinuity will effectively work as a Fabry-Perot resonator [17] with the lasing frequency being the Fabry-Perot resonator mode. If the index of refraction could be periodically modulated along the other two dimensions as well, yielding a full photonic band gap, then the possible phase space for spontaneous emission would be drastically modified, enhancing laser efficiency.

The search was on for the geometry that would yield a gap for the smallest dielectric contrast. The first call was for a three-dimensional checkerboard structure, with a face-centered-cubic (*fcc*) lattice symmetry [6]. Bragg back-scattering at the Brillouin zone boundaries will lift the degeneracies, or at least some of them, and open a gap for any contrast value. If all these small gaps in the individual directions appeared in the same frequency, a full photonic band gap would open. This suggests that the structure with the most spherical Brillouin zone, the *fcc* lattice structure, would be the best candidate. Simple calculations for the *fcc* lattice put a lower limit of 1.21 [6] and 1.46 [7] to the necessary refractive index contrast for a gap to open up. Both approaches, however, used the one-dimensional simplification, and it was not clear what the actual lower limit should be. In fact, as we will see later, the *fcc* structure with spherical scatterers exhibits only a pseudogap between the first two bands, a small frequency region with strong reduction in the photonic density of states, but not a complete photonic band gap.

Besides the lattice symmetry, the spatial distribution of the dielectric material in real space still needed to be determined as well. Yablonovitch and Gmitter at Bellcore employed a "cut-and-try" method [18], where they fabricated many different *fcc* dielectric structures and then measured their transmission to see if a frequency gap existed. All experiments were done in the microwave regime, with the lattice constant around a few centimeters, to ease the manufacturing process. In 1989, after two years and some dozens of attempted structures, they identified only one structure with a complete photonic band gap [18]. This was an *fcc* arrangement of overlapping air spheres in dielectric material of refractive index 3.5 (they used the commercial low-loss dielectric Emerson & Cumming Stycast-12) with air filling ratio of 86%.

In the meantime theoretical interest started growing. The first attempts of solving the full three-dimensional problem employed a scalar wave approximation ignoring the vector nature of the electromagnetic field under the assumption that the two polarizations could be solved separately. The equivalent scalar Maxwell's equation, then, is cast into an infinite eigenvalue problem using a plane wave expansion of both the fields and the dielectric function [19, 20], or solved with other methods familiar from electronic band theory [21, 22]. The results indicated the existence of large gaps not only for the structure indicated by Yablonovitch, but also for the case of dielectric spheres in an *fcc* arrangement in air, contrary to the experimental results. In addition, even for the cases with qualitative agreement, they predicted different midgap frequency and gap width. It was apparent that neglect of the vector nature of light was way more important than initially thought.

The full vector solutions came shortly afterwards [23, 24, 25], using the plane wave expansion method modified to take into account the additional degree of freedom coming from the light polarization. Computations for Yablonovitch's proposed structure indicated that there was no complete gap between the lowest two bands, but only a pseudogap. The degeneracies at the **W** and **U** symmetry points of the *fcc* Brillouin zone were not lifted, resulting in just a strong reduction in the photonic density of states for these frequencies. The Iowa State group [25] however found a way to lift the symmetry induced degeneracies by changing the spatial distribution of the dielectric material inside the unit cell. They added a second air sphere in the unit cell creating a diamond lattice. For a refractive index of 3.6, they calculated gaps with as large as 15.7% midgap ratio ($\Delta\omega/\omega_g$) for dielectric spheres in air at filling ratio 37% and 28.8% for the case of air spheres with filling ratio 81%. It is amusing though that the *fcc* arrangement of air spheres did after all have a complete gap at higher frequencies [26, 27], between the 8th and 9th bands.

It became apparent that any non-spherical configuration for the dielectric material inside the *fcc* unit cell will lift the above-mentioned degeneracies and will produce a full gap [28]. Calculations for a number of different geometries with the underlying diamond symmetry group indicated wide gaps and a lower limit of 1.87 for the required index contrast. Yablonovitch quickly devised a way of constructing a dielectric diamond lattice by drilling cylindrical holes into the dielectric material [29]. The experimental results demonstrated for the first time a complete photonic band gap, in perfect agreement with the theoretical predictions [28]. This is a nice example of theoretical work guiding successfully the experimental work. Other geometries and fabrication techniques have also been used since then: a layer-by-layer structure [30, 3, 32], first proposed by the Iowa State group, or colloidal suspensions [33, 34].

A lot of work has also been done for two-dimensional photonic band gap structures[35, 36]. These systems are much easier to fabricate, and the photonic gaps should open wider and for smaller contrast. Assume the dielectric modulation to be only on the $x - y$ plane and in-plane wave propagation. The structure consisting of parallel, infinitely long air cylinders in a dielectric background, arranged in a triangular lattice, was shown to be the optimal case [37], together with the one consisting of dielectric cylinders in air arranged in the graphite structure [38]. Experiments done in the microwave regime [39, 40] showed excellent agreement with the theoretical predictions.

Although periodicity has been the important issue for the existence of photonic band gaps, it has been shown that the gap is sustained even in the presence of a fair amount of disorder [41]. In two dimensions, it was found that higher order photonic gaps close quickly with increasing disorder, while the lower order gaps, especially the first one, remain open for large values of the disorder [42]. For all frequencies however, light becomes localized. In three dimensions [43] similar disorder tolerance was found, provided the topology of the structure was not changed (e.g. for structures with network topology the gaps will disappear easily by breaking the network).

Exciting applications of photonic band gap materials in laser science would require their use as high-Q microcavities in the optical range. For example, a light-emitting diode (LED) surrounded by an optical cavity will have only a single electromagnetic mode available for the output spontaneous emission. Thus it can acquire many of the coherence properties of lasers, effectively operating as a threshold-less laser device. That means that photonic band gap materials should be able to be "doped" creating localized electromagnetic modes inside the gap, in a similar way that their electronic counterparts, the semiconductors, are doped. Indeed, adding dielectric material inside the photonic band gap structure introduces a localized defect "donor" mode inside the gap with its frequency close to the upper gap edge. On the other hand, removing dielectric material introduces an "acceptor" mode close to the lower gap edge [44, 45, 46].

Finally, there have been some theoretical studies on the modification of atomic interactions and processes in photonic band gap materials [21, 48]. It has been shown that if the photon emitted, by an excited atom in a photonic band gap material, has frequency inside the photonic gap, then after tunneling away for a couple of lattice constants, it would eventually return and get re-absorbed by the atom. The photon would be localized around the atom, resulting in an excited atom-photon stable bound state, similar to the electron-impurity bound states in semiconductors. If many atoms were put together in the photonic crystal, they would interact and couple together through their localized photons, creating a photonic impurity band inside the gap. Also studies on the emission power from electric dipoles [27, 11] showed total inhibition of emission in the photonic band gap as well as strong enhancement around the band edges.

Theoretical formulation and numerical methods

There are many similarities between electron waves in the periodic ionic potential of a crystal and electromagnetic waves in an artificial periodic dielectric structure. An electron of mass m is described by the scalar Schrödinger equation

$$\mathcal{H}_{el}\psi(\vec{r}) = \left\{ \frac{-\hbar^2}{2m}\nabla^2 + V(\vec{r}) \right\} \psi(\vec{r}) = E\psi(\vec{r}), \tag{1}$$

while the photon is described by the vector Maxwell equations [50]

$$\mathcal{H}_{ph}\vec{H}(\vec{r}) = \left\{ \nabla \times \frac{1}{\epsilon(\vec{r})}\nabla\times \right\} \vec{H}(\vec{r}) = \frac{\omega^2}{c^2}\vec{H}(\vec{r}). \tag{2}$$

The periodicity is expressed in the potential $V(\vec{r}+\vec{R}) = V(\vec{r})$ for the electron and in the dielectric function $\epsilon(\vec{r}+\vec{R}) = \epsilon(\vec{r})$ for the photon, where $\vec{R}$ represents lattice vectors. E and ψ stand for the energy eigenvalue and eigenfunction respectively for the electronic case while ω^2/c^2 and $\vec{H}$ for the square of the frequency eigenvalue and the eigenmode respectively for the photonic case. Both operators $\mathcal{H}$ are linear and Hermitian [14]. Periodicity, linearity, and Hermiticity of the problem means that all concepts of real crystals, such as, reciprocal space, Brillouin zones, dispersion relations, Bloch wavefunctions, Van Hove singularities, etc., will be applied successfully to the photon case as well. Then if the energies of the electrons in a crystal are arranged into energy bands separated by gaps [51], it is expected that for the appropriate structural parameters, the same should be true for photons in a photonic crystal.

The Plane Wave Expansion method follows very closely from the corresponding nearly free electron approximation and pseudopotential numerical methods used in electronic band theory [51]. Since the dielectric constant $\epsilon(\vec{r})$ is periodic, the solution is expanded in an infinite Bloch sum of plane waves [25, 26] for each wave vector $\vec{k}$ in the Brillouin zone

$$\vec{H}_{\vec{k}}(\vec{r}) = \sum_{\vec{g}} \sum_{\lambda=1}^{2} \mathrm{H}_{\vec{g},\lambda} \hat{\mathrm{e}}_{\lambda} e^{i(\vec{k}+\vec{g})\vec{r}}, \tag{3}$$

where the sum is over all reciprocal lattice vectors $\vec{g}$ and the two possible transverse polarization vectors $\hat{\mathrm{e}}_{1,2}$. Using the Fourier transform of the periodic dielectric constant

$$\begin{aligned} \epsilon(\vec{r}) &= \sum_{\vec{g}} \epsilon_{\vec{g}} e^{i\vec{g}\vec{r}}, & (4) \\ \epsilon_{\vec{g}} &= \frac{1}{V_{cell}} \int_{cell} \epsilon(\vec{r}) e^{-i\vec{g}\vec{r}} d\vec{r}, & (5) \end{aligned}$$

where V_{cell} is the volume of the Wigner-Seitz cell, and substituting into Eq. (2) we end up with an infinite eigenvalue problem

$$\sum_{\vec{g}'} |\vec{k}+\vec{g}||\vec{k}+\vec{g}'| \epsilon^{-1}_{\vec{g}-\vec{g}'} \begin{pmatrix} \hat{\mathrm{e}}_2\hat{\mathrm{e}}_{2'} & -\hat{\mathrm{e}}_2\hat{\mathrm{e}}_{1'} \\ -\hat{\mathrm{e}}_1\hat{\mathrm{e}}_{2'} & \hat{\mathrm{e}}_2\hat{\mathrm{e}}_{1'} \end{pmatrix} \begin{pmatrix} \mathrm{H}_{\vec{g}',1'} \\ \mathrm{H}_{\vec{g}',2'} \end{pmatrix} = \frac{\omega^2}{c^2} \begin{pmatrix} \mathrm{H}_{\vec{g},1} \\ \mathrm{H}_{\vec{g},2} \end{pmatrix} \tag{6}$$

In the infinite problem it should not make any difference if we used the Fourier transform $\eta_{\vec{g}-\vec{g}'}$ of the inverse of the dielectric function $\eta(\vec{r}) = 1/\epsilon(\vec{r})$ instead of $\epsilon^{-1}_{\vec{g}-\vec{g}'}$. However, it does make a difference when we truncate the problem into a finite eigenvalue problem in order to solve it. In most cases when reconstructing $\epsilon(\vec{r})$, $\epsilon^{-1}_{\vec{g}-\vec{g}'}$ provides a better representation than $\eta_{\vec{g}-\vec{g}'}$, and so a faster convergence as a function of the number of terms kept in the truncation [5].

The problem can also be cast in terms of the electric field

$$\nabla \times [\nabla \times \vec{E}(\vec{r})] = \frac{\omega^2}{c^2}\epsilon(\vec{r})\vec{E}(\vec{r}) \tag{7}$$

Substituting the Fourier expansions of $\vec{E}(\vec{r})$ and $\epsilon(\vec{r})$ into Eq. (7) we end up with an infinite generalized Hermitian eigenvalue problem

$$(\vec{k}+\vec{g}) \times [(\vec{k}+\vec{g}) \times \vec{\mathbf{E}}_{\vec{g}}] + \frac{\omega^2}{c^2}\sum_{\vec{g}'} \epsilon_{\vec{g}-\vec{g}'}\vec{\mathbf{E}}_{\vec{g}'} = 0 \tag{8}$$

Upon truncation it will yield the same results as the ones obtained by solving the problem cast in terms of $\vec{H}$, only if $\epsilon^{-1}_{\vec{g}-\vec{g}'}$ is used in the latter case [5].

In two dimensions the two polarizations can be decoupled, resulting in two scalar eigenvalue problems: one for the electric field polarized parallel to the axis of the cylinders (E_z or transverse magnetic (TM) polarization), expressed in terms of the electric field

$$|\vec{k}+\vec{g}|^2\mathbf{E}_{\vec{g}} = \frac{\omega^2}{c^2}\sum_{\vec{g}'} \epsilon_{\vec{g}-\vec{g}'}\mathbf{E}_{\vec{g}'}, \tag{9}$$

and one for the magnetic field parallel to the cylinders (H_z or TE-polarization), expressed in term of the magnetic field

$$\sum_{\vec{g}'} \epsilon^{-1}_{\vec{g}-\vec{g}'}(\vec{k}+\vec{g})(\vec{k}+\vec{g}')\mathbf{H}_{\vec{g}'} = \frac{\omega^2}{c^2}\mathbf{H}_{\vec{g}}, \tag{10}$$

where now the summation is over the two-dimensional reciprocal lattice vectors $\vec{g}$. In two dimensions, for cylinders of circular cross section with radius R and dielectric constant ϵ_a, embedded in a dielectric background ϵ_b with filling ratios f_a less than closed packed, $\epsilon_{\vec{g}}$ is easily evaluated analytically and is the same for any lattice arrangement

$$\epsilon_{\vec{g}} = \epsilon_b\delta_{\vec{g},0} + 2f_a(\epsilon_a - \epsilon_b)\frac{J_1(|\vec{g}|R)}{|\vec{g}|R} \tag{11}$$

where J_1 is the first order Bessel function. Both polarizations generally exhibit gaps but usually at different frequencies. A complete photonic band gap for both polarizations has been found for a triangular arrangement of air cylinders in dielectric [37] and for a graphite arrangement of solid dielectric cylinders in air [38].

The plane wave expansion method is very useful because of its simplicity. The only requirement is the calculation of the Fourier transform of the dielectric function in the unit cell or, if larger systems are to be studied, in a suitably chosen supercell. This calculation is usually done numerically. Problems, however, arise when the materials under study exhibit a frequency dependence in their dielectric constant. In the plane wave method one uses a fixed wave vector $\vec{k}$ and calculates the frequency eigenvalues $\omega(\vec{k})$ corresponding to it. What would be needed is a method that uses a fixed frequency ω and calculates the corresponding wave vectors.

This is achieved by the Transfer Matrix method, first introduced in 1992 [11, 53]. In this method one first discretizes space into a fine grid uniform cubic grid, on which the electric field and the dielectric constant function are defined. The magnetic field is defined on a similar inter-penetrating grid, such that both grids together form a *bcc* lattice. In such setting, $\vec{E}(\vec{r})$ and $\vec{B}(\vec{r})$ are not on the same point, but displaced by $\vec{d} = (a/2, a/2, a/2)$, where a is the separation distance between two grid points. On this grid we will solve the time-independent Maxwell's equations

$$\nabla \times \vec{E} = -i\omega\vec{B}, \qquad \nabla \times \vec{H} = i\omega\vec{D}, \tag{12}$$

or, transformed into $\vec{k}$ space

$$\vec{k} \times \vec{E} = \omega\vec{B}, \qquad \vec{k} \times \vec{H} = -\omega\vec{D}, \tag{13}$$

where $\vec{D}(\vec{r}) = \epsilon_0\epsilon(\vec{r})\vec{E}(\vec{r})$ and $\vec{B}(\vec{r}) = \mu_0\mu(\vec{r})\vec{H}(\vec{r})$. In the first of Eqs. (13) we approximate

$$k_x \approx (ia)^{-1}[\exp(ik_x a) - 1], \text{ etc.}, \tag{14}$$

and in the second,

$$k_x \approx (-ia)^{-1}[\exp(-ik_x a) - 1], \text{ etc.} \tag{15}$$

If now Eqs. (13) are transformed back into real space, we will get a set six difference equations. The z component of each field can be eliminated, since it is always related with the other two components. Making the substitution $\vec{H}' = (i/a\omega\epsilon_0)\vec{H}$ we finally arrive to four equations relating the x and y components of the two fields

$$\begin{aligned} E_x(\vec{r}+\vec{c}) &= \frac{a^2\omega^2}{c^2}\mu(\vec{r})H'_y(\vec{r}) + E_x(\vec{r}) + \epsilon^{-1}(\vec{r})[H'_y(\vec{r}+\vec{a}) - H'_y(\vec{r}) - H'_x(\vec{r}-\vec{b}) + H'_x(\vec{r})] \\ &- \epsilon^{-1}(\vec{r}+\vec{a})[H'_y(\vec{r}) - H'_y(\vec{r}+\vec{a}) - H'_x(\vec{r}+\vec{a}-\vec{b}) + H'_x(\vec{r}+\vec{a})], \text{ etc.,} \end{aligned} \tag{16}$$

$$\begin{aligned} &H'_x(\vec{r}+\vec{c}) = \epsilon(\vec{r}+\vec{c})E_y(\vec{r}+\vec{c}) + H'_x(\vec{r}) \\ -\ &\frac{c^2}{a^2\omega^2}\mu^{-1}(\vec{r}-\vec{a}+\vec{c})[E_y(\vec{r}+\vec{c}) - E_y(\vec{r}-\vec{a}+\vec{c}) - E_x(\vec{r}-\vec{a}+\vec{b}+\vec{c}) + E_x(\vec{r}-\vec{a}+\vec{c})] \\ +\ &\frac{c^2}{a^2\omega^2}\mu^{-1}(\vec{r}+\vec{c})[E_y(\vec{r}+\vec{a}+\vec{c}) - E_y(\vec{r}+\vec{c}) - E_x(\vec{r}+\vec{b}+\vec{c}) + E_x(\vec{r}+\vec{c})], \text{ etc.,} \end{aligned} \tag{17}$$

where the vectors $\vec{a}, \vec{b}, \vec{c}$ that define the cubic mesh are of length a and point to the x, y, z directions respectively. In this scheme, Eqs. (16) are used to find the electric field components on one plane of cells in terms of the electric and magnetic fields on the previous $(-\vec{c})$ plane, while Eqs. (17) are used to find the magnetic field in next plane of cells terms of the electric field on that plane and the magnetic fields on the previous one. Thus, given the initial fields on one side of the structure we can find the fields on the other one. The matrix connecting them is called the *transfer matrix.* If the structure is just the unit cell of a periodic system, then from the eigenvalues of the transfer matrix we can get the band structure $\vec{k}(\omega)$ [11].

The power of this method is that one can choose a slab finite in the z direction, set up the transmitted fields on one side, and numerically integrating Maxwell's equations along the z axis until the other side of the slab. Projecting the fields there into left and right propagating plane waves we can reconstruct the incident and reflected waves, thus obtaining the reflection and transmission coefficients of the finite slab, something the plane wave method can not provide. Besides that, it's numerical complexity scales better with size, since for a structure with $L \times L \times L$ grid cells, the transfer matrix has dimension $4L^2 \sim O(L^2)$ while for a plane wave method using a basis set of $L \times L \times L$ plane waves to describe the fields, the matrix for diagonalization has dimension $2L^3 \sim O(L^3)$, and the diagonalization of a matrix of dimension N scales as $O(N^3)$.

For periodic systems both previous methods perform fast enough. For larger supercell disordered systems, however, the computation time becomes too long. Also, they are both time-independent, and so they assume the existence of steady state solutions, leaving out the possibility for studying dynamical time-dependent phenomena. There is a third, time-dependent, 'order-N' method, that solves the problem efficiently fast, without the need for matrix diagonalization. This is the Finite-Difference-Time-Domain (FDTD) [9, 10] spectral method [57]. Maxwell's equations are again solved on a fine grid, but now in time domain. Assuming a cubic grid cell of side a, the three electric field components are defined on the middle of the cube's facets normal to them, while the magnetic field components are defined on the middle of the cube's edges parallel to them. Thus each electric field component is surrounded by a circulating magnetic field and *vice versa*, yielding a nice representation for Maxwell's integral equations as well. The corresponding difference equations for the space derivatives are then central-difference in nature and second-order accurate. The electric and the magnetic fields are also displaced in time, separated by half time step $\Delta t/2$, yielding central-difference, second-order accurate equations for the time derivatives as well. Maxwell's equations are then used to evolve, from time step n to time step $n+1$, the x component of electric field that is defined on grid point i, j, k

$$E_x|_{i,j,k}^{n+1} = E_x|_{i,j,k}^{n} + \frac{\Delta t}{a\ \epsilon_{i,j,k}} \left(H_z|_{i,j+1/2,k}^{n+1/2} - H_z|_{i,j-1/2,k}^{n+1/2} - H_y|_{i,j,k+1/2}^{n+1/2} + H_y|_{i,j,k-1/2}^{n+1/2} \right) \tag{18}$$

There are similar equations for the rest of the electric and magnetic field components [10]. Linear dispersion can be taken into account using explicitly the time convolution of the material's susceptibility tensor $\chi(t)$ with the electric field $\int \chi(t-t')\vec{E}(t')dt'$ [10, 58]. The photonic band structure is calculated as follows. For a suitably chosen supercell with applied periodic boundary conditions and for a particular wave vector $\vec{k}$ the magnetic field is initiated to

$$\vec{H}(\vec{r}) = \sum_{\vec{g}} \sum_{\lambda=1}^{2} \hat{e}_\lambda e^{i(\vec{k}+\vec{g})\vec{r}+i\phi(\vec{g})} \tag{19}$$

where $\phi(\vec{g})$ is a random phase, while the electric field is set to zero. During time marching, the electric field values at some sampling grid points are saved as a time series, and at the end they are numerically Fourier-transformed back to frequency space. The peaks found, correspond to the eigenfrequencies for the particular $\vec{k}$ [57]. It is worth noting, again, that due to the explicit knowledge of the system's time history, the frequency dependence of the dielectric constant is easily taken into account. This method is also powerful because one can easily use it to perform transmission "experiments" through a slab of the material, or make detailed simulations of wave propagation through such materials with specific source designs or requirements. For a large supercell, the spectrum for each $\vec{k}$ does not consist of well separated peaks, but rather by a plethora of them. By adding the spectra of all $\vec{k}$ of the irreducible first Brillouin zone we find that it reproduces remarkably well the photonic density of states, for both periodic and disordered systems. Finally, it is very useful for the study of nonlinear photonic band gap materials [58, 59, 60]. Transfer matrix time-independed methods assume the existence of steady state solutions for any system, leaving out the possibility of observing the rich dynamical response nonlinear materials have to intense radiation. The explicit time dependence of this method is its true power: any dynamical process involved in wave propagation can be taken into account.

Nonlinear optics in photonic band gap materials

The advent of optical fibers[61] has been an important milestone in the transition from electronics to photonics technology. Replacing the cooper wires in electronic circuits, optical fibers guide light, with a much larger bandwidth and low power losses and noise, revolutionizing today's telecommunications industry. The next step towards an all-optical digital technology would be the optical switch, capable of doing the routing and logic decisions in gate arrays. Since one light beam must interact with another for optical switching to occur, the optical material must be nonlinear [62, 63, 64, 1], because the photon-photon interaction cross section is almost zero in linear media.

Before the advent of the laser in 1960 [66] dielectric materials were thought to be essentially linear. Different light beams would not interact with each other in them and the material would remain unaffected by the light. The capability of intense coherent light beams that came with the laser however made it possible to go further into the nonlinear response regime of the materials. Intense light can change the properties of the medium, which, in turn, changes the light itself, resulting in a rich variety of exciting phenomena [67, 2, 69, 70, 71]. Different light beams can interact with each other yielding sums and differences of frequencies [72], or just harmonics of the single optical frequency [73]. Nonlinearity can also change the refractive index of the medium, resulting in excitations of solitons [74, 69] and bistable input-output response [2]. It is this last property that will be useful in designing all-optical switches.

Nonresonant optical nonlinearity is expressed in terms of field-dependent higher-order terms in the susceptibility tensor χ. The nature of this effect can be seen classically as the response of an electron to an anharmonic potential driven by an electromagnetic field. For driving fields much smaller than the interatomic fields the response is essentially linear, but for fields comparable to the interatomic ones the deformation of the electron clouds (or wavefunctions), and thus, of the medium polarization, becomes appreciable, and of course nonlinear. These nonresonant, virtual optical interactions can be extremely fast, as opposed to resonant interactions [64] like electron-hole pair production and recombination, opening the possibility for ultrafast, all-optical THz-rate switching. Unfortunately, they are also much weaker, requiring really intense electromagnetic fields.

The first-order linear term χ_1 is, in general, frequency dependent and is responsible for dispersion in the medium. The second-order susceptibility χ_2 introduces the field dependency to lowest order. Assuming a local, weakly dispersive χ_2, the induced dipole moment per unit volume is related to the applied electric field by $\vec{P} = \epsilon_0(\chi_1\vec{E}+\chi_2\vec{E}\vec{E})$. This term is responsible for the electro-optic effect [16, 64], second harmonic generation, and two wave frequency mixing [63, 64]. Incorporation of such materials into laser systems gives the possibility for constructing efficient sources of coherent radiation for any frequency [75]. As a third-rank tensor however, χ_2 must vanish if the medium is symmetric under inversion through a center of symmetry. Under this assumption, we will ignore this term throughout the rest of this work.

Most materials however exhibit a third-order susceptibility χ_3. This is responsible for third harmonic generation and three-wave frequency mixing, as well as for an intensity-dependent dielectric constant [64, 1]. The latter is the larger effect, and so ignoring the former and assuming a nondispersive χ_3, we have a medium described by a Kerr nonlinearity $\vec{P} = \epsilon_0(\chi_1 + \chi_3|\vec{E}|^2)\vec{E}$, or in terms of the electric displacement $\vec{D} = \epsilon_0(\epsilon_L + \epsilon_{NL}|\vec{E}|^2)\vec{E}$. In such materials, for a constant wave input, the input and output frequencies can be identical, but having an intensity dependent dielectric constant can cause the output intensity to be a multi-valued function of the input intensity. For certain input optical powers there may exist two distinct transmission branches forming a hysteresis, or bistable, loop. The particular state the system is in depends on the its history and can be controlled optically, forming an elementary all-optical switch.

Many all-optical switching devices have been proposed or demonstrated with materials exhibiting a Kerr, or other type, nonlinearity [2, 76]. One special case are the nonlinear periodic multilayer, or distributed feedback, systems [14, 13, 79]. Because of the periodic modulation of the linear part of the refractive index the waves undergo coherent backscattering, effectively working as an optical power feedback mechanism. This results in a great enhancement of the nonlinear effect, and so a reduction of the optical power threshold for observing it. In the low intensity limit these structures are essentially Bragg reflectors, characterized by frequency bands of high transmission separated by photonic band gaps. For high intensities and frequencies inside the transmission band, bistability results from the modulation of transmission by an intensity-dependent phase shift. For frequencies inside the photonic band gap, bistability originates from gap soliton formation [5, 7, 15, 9, 84, 14]. It is the latter that takes full advantage of the distributed feedback mechanism and can lead to very low optical power thresholds for switching [6].

A remarkable property of materials exhibiting a Kerr nonlinearity is the formation of solitons. In a linear dispersive medium, a pulse will broaden with time because of the different group velocities each frequency component has. In a nonlinear medium however, under appropriate conditions, this action can be balanced by the nonlinearity leading to self-sustained soliton solutions, pulse envelopes that are preserved as they propagate in the medium. In a one-dimensional layered photonic band gap material exhibiting a Kerr nonlinearity, the linear dispersion is provided by the periodic modulation of the refractive index, which is present even in the absence of any intrinsic material dispersion. This dispersion is largest for frequencies inside the photonic band gap of the corresponding linear structure, and the corresponding self-sustained soliton solutions are called gap solitons or solitary waves. Due to the strong Bragg reflections, gap solitons can have very small group velocities. When they are excited by an incident constant wave, under appropriate conditions, they may remain coupled to it, resulting in standing-wave stationary gap solitons.

For waves whose frequency lies within the gap, hysteresis forms as follows: For a low incident light intensity the structure acts as a Bragg reflector. Increasing the intensity after a threshold value I_{SU} results in the excitation of a stationary gap soliton. Because of the nonlinear refractive index change, the area below the soliton is effectively an allowed (or transparent) area. The incident wave couples to it and effectively tunnels through the structure, resulting in high transmission, even though its frequency lies within the forbitten gap. The system is now in the high transmission branch. Decreasing however the intensity will not force the system to switch-down at I_{SU}. The incident wave will still remain coupled to the soliton for the smaller intensities, and at some point it will even reach a resonant $T = 1$ transmission state. Decreasing the intensity further, below a threshold value I_{SD}, will cause the wave-soliton coupling to break. The soliton then becomes unstable, it propagates out of the structure, and the system switches back to the low transmission state.

Research objectives

This dissertation aims to study two regimes of photonic band gap materials. The first one focuses on one-dimensional layered PBG structures doped with a nonlinear, Kerr-type material. As pointed out earlier, such structures can exhibit bistability, an essential feature for an all-optical switching device. Our points of interest, both theoretical and practical, are to:

- Study existent, and/or develop our own, approximate structure models for solving the problem of constant wave propagation in such materials: how they compare to exact numerical solutions (or experimental data) of the real structure and what physical mechanisms are responsible for the differences there may exist.

- Architectures that can achieve low power thresholds for switching using a minimum amount of nonlinear material: use both approximate and realistic structure models, as well as both analytical and numerical techniques, to study and understand their properties.

- Externally controlled switching mechanisms: use exact numerical simulations to study, the dynamics of driving the system from one transmission state to the other by means of pulse injection, it's feasibility, as well as it's limitations.

The second regime of study focuses on two-dimensional photonic band gap materials. Generally, there exist two mechanisms that can be responsible for the formation of the spectral gaps. Bragg-like multiple scattering and excitation of single scatterer Mie resonances [8]. The first one resembles the nearly free electron picture, for which the gap is opened from the wave's coherent backscattering due to the periodic lattice, and is the one generally accepted. The second one resembles the strongly-localized, or tightly-bound, electron picture, in which the Mie resonances are thought as analogous the the electronic orbitals, and so transmission is achieved with resonance standing-waves hopping (tunneling) from one site to the other. Narrow transmission bands are then formed around the Mie resonance frequencies, which are separated by wide gaps. It is not clear which the dominant mechanism is in each different case (different lattice realization, wave polarization etc), and how the system's properties should depend on it. Our points of interest are to:

- Identify the mechanism responsible for the formation of the spectral gaps for each different case: develop a physical model for the "strongly-localized" photon picture (which has never been described before), and find in which cases it does provide an accurate description of the system's properties.

- Understand how the system's properties depend on the mechanism forming the spectral gaps: use numerical techniques to study, in each different case, the changes in the spectral gaps and in the transmission of waves whose frequency falls in them, as the periodicity of the structure is destroyed.

Dissertation organization

In this dissertation we follow an alternative thesis format permitting the inclusion of papers that are published (or submitted/to be submitted) in scholarly journals. Each subsequent chapter therefore consists of a single paper, presented exactly the way it was (or will be) published.

In the general introduction we provided the basic theoretical background, an extensive literature review, and some of the numerical methods commonly used for photonic band gap materials, as well as for nonlinear optics in photonic band gap materials. These should be enough for understanding the research effort that is going to be presented in the next chapters. The basic objectives for this effort have already been set in the previous section. Here we will provide a brief introduction to each paper to be presented.

In Chapter 2 we examine an approximate structure model for a 1D layered nonlinear structure. In this, the nonlinear material is concentrated in very thin, or δ-function layers, while the rest is linear. The model is tested against the more realistic case where the structure consists of alternating linear and nonlinear finite width layers. Differences are found, and the physical mechanisms responsible for them are identified. In Chapter 3 we use both the δ-function approximation and the realistic finite width case to study an alternative architecture that could provide low switching thresholds. This is, a single nonlinear layer sandwiched between two linear structures. Both analytical and numerical calculations are presented. The origins of the bistable behavior and the conditions under which low threshold switching can be achieved are found. Also, the differences between the approximate and exact structure models, and their physical origins, are identified. In Chapter 4 we use exact numerical simulations and identify the weaknesses of time-independent solutions. We also study the dynamics of switching a nonlinear layered system between different transmission state by pulse injections. We find that such switching is possible only under certain conditions. In Chapter 5 we develop an approximate structure model to explain recent experimental results that showed that colloidal crystals have a multistable response to intense radiation. Our first approximation consists of a one-dimensional simplification of the three-dimensional lattice. Incorporating an effective

Kerr-type interaction fails to reproduce the experimental results (which is expected since the colloidal materials do not exhibit any intrinsic nonlinearity), so we developed a more realistic lattice-light coupling model. Polarizable material feels a force from the inhomogeneous electric field, and so there is a dynamic coupling between the light and the colloidal lattice. The actual steady state corresponding to each incident power is found self-consistently. The experimental results are very well reproduced . This light-lattice interaction can be thought of as the classical analog of the electron-phonon interaction. In Chapter 6 we move into the two dimensions where we unfold the mechanism responsible for the formation of the gaps in one particular case: high dielectric cylinders in a low dielectric background with the electric field polarized parallel to the cylinders. The wave equation describing this polarization is a scalar one. Adopting the "strongly-localized" photon picture we develop a linear combination of Mie resonances model, following the ideas of it's electronic counterpart, the linear combination of atomic orbitals model. The model's parameters are fitted to *ab initio* results. Through various testings, it's performance is found to be excellent, justifying the picture we adopted for the photonic states. In Chapter 7 we use two different numerical techniques to study four different cases under disorder: high dielectric cylinders in air and *vise versa*, for both polarizations ($\vec{E}$ or $\vec{H}$ parallel to the cylinders). The different responses we find in each case are grouped into two categories, and it is shown that they can be attributed to the two different gap forming mechanisms. This way we can deduce which gap forming mechanism is the dominant one in each case. Finally, in the general conclusions in Chapter 8, we discuss what we have learned and what we have accomplished through this effort, as well as directions for future work.

Chapter 2 has been published as a brief report in Physical Review B **54**, 10249 (1996); chapter 3 has been published as a regular article in Physical Review B **56**, 15090 (1997); chapter 4 will be submitted for publication as a regular article in Physical Review E; chapter 5 has been published as a regular article in Physical Review E **55**, 3613 (1997); chapter 6 has been published in Physical Review Letters **81**, 1405 (1998); chapter 7 will be submitted for publication as a regular article in Physical Review B.

Bibliography

[1] C. G. Darwin, Phil. Mag. **27**, 675 (1914).

[2] William H. Zachariasen, *Theory of X-Ray Diffraction in Crystals* (Dover Publications, New York, 1945).

[3] For excellent reviews on photonic band gap materials see the proceedings of the NATO ARW, *Photonic Band Gaps and Localization*, ed. by C. M. Soukoulis, (Plenum, N.Y., 1993); *Photonic Band Gap Materials*, ed. by C. M. Soukoulis, NATO ASI, Series E, vol. 315.

[4] E. Yablonovitch, J. Phys.: Condens. Matter **5**, 2443 (1993);

[5] Pierre R. Villeneuve and Michel Piché, Prog. Quant. Electr. **18**, 153 (1994);

[6] Eli Yablonovitch, Phys. Rev. Lett. **58**, 2059 (1987).

[7] Sajeev John, Phys. Rev. Lett. **58**, 2486 (1987).

[8] R. G. Hulet, E. S. Hilfer, and D. Kleppner, Phys. Rev. Lett. **55**, 2137 (1985).

[9] Sajeev John, *Physics Today* **32**, 33 (1991).

[10] *Scattering and localization of Classical waves in Random Media*, ed. by P. Sheng (World Scientific, Singapore, 1990)

[11] J. Martorell and N. M. Lawandry, Phys. Rev. Lett. **65**, 1877 (1990).

[12] G. Kurizki and A. Z. Genack, Phys. Rev. Lett. **66**, 1850 (1991).

[13] For a review see the special issue of J. Opt. Soc. Am. B **10**, 280-408 (1993) on *Development of Applications of Materials Exhibiting Photonic Band Gaps.*

[14] J. D. Joannopoulos, R. D. Meade, and J. N. Winn *Photonic Crystals* (Princeton University Press, Princeton, 1995).

[15] H. Kogelnik and C. V. Shank, J. Appl. Phys. **43**, 2327 (1972).

[16] Amnon Yariv and Pochi Yeh *Optical Waves in Crystals*, (Wiley, New York, 1984).

[17] Max Born and Emil Wolf, *Principles of Optics* (Pergamon Press, New York, 1980).

[18] E. Yablonovitch and T. J. Gmitter, Phys. Rev. Lett. **63**, 1950 (1989).

[19] S. Satpathy, Ze Zhang, and M. R. Salehpour, Phys. Rev. Lett. **64**, 1239 (1990).

[20] K. M. Leung and Y. F. Liu, Phys. Rev. B **41**, 10188 (1990).

[21] Sajeev John and Raghavan Rangarajan, Phys. Rev. B **38**, 10101 (1988).

[22] E. N. Economou and A. Zdetsis, Phys. Rev. B **40**, 1334 (1989).

[23] K. M. Leung and Y. F. Liu, Phys. Rev. Lett. **65**, 2646 (1990).

[24] Ze Zhang and Sashi Satpathy, Phys. Rev. Lett. **65**, 2650 (1990).

[25] K. M. Ho, C. T. Chan, and C. M. Soukoulis, Phys. Rev. Lett. **65**, 3152 (1990).

[26] H. S. Sözüer, J. W. Haus, and R. Inguva, Phys. Rev. B **45**, 13962 (1992).

[27] Toshio Suzuki and Paul K. L. Yu, J. Opt. Soc. Am. B **12**, 570 (1995).

[28] C. T. Chan, K. M. Ho and C. M. Soukoulis, Europhys. Lett. **16**, 563 (1991).

[29] E. Yablonovitch, T. J. Gmitter and K. M. Leung, Phys. Rev. Lett. **67**, 2295 (1991); E. Yablonovitch and K. M. Leung, Nature **351**, 278 (1991).

[30] K. M. Ho, C. T. Chan, C. M. Soukoulis, R. Biswas, and M. Sigalas, Solid State Comm. **89**, 413 (1994); E. Ozbay, A. Abeyta, G. Tuttle, M. C. Tringides, R. Biswas, M. Sigalas, C. M. Soukoulis, C. T. Chan, and K. M. Ho, Phys. Rev. B **50**, 1945 (1994).

[31] S. Fan, P. R. Villeneuve, R. D. Meade, and J. D. Joannopoulos, Appl. Phys. Lett. **65**, 1466 (1994).

[32] G. Feiertag *et al.*, Appl. Phys. Lett. **71**, 1441 (1997).

[33] R. J. Hunter, *Foundations of Colloidal Science* (Clarendon, Oxford, 1993).

[34] İ. İnanç Tarhan and George H. Watson, Phys. Rev. Lett. **76**, 315 (1996).

[35] M. Plihal and A. A. Maradudin, Phys. Rev. B **44**, 8565 (1991).

[36] Pierre R. Villeneuve and Michel Piché, Phys. Rev. B **46**, 4969 (1992); *ibid* **46**, 4973 (1992).

[37] R. D. Meade, K. D. Brommer, A. M. Rappe, and J. D. Joannopoulos, Appl. Phys. Lett. **61**, 495 (1992).

[38] A. Barra, D. Cassagne, and C. Jouanin, Appl. Phys. Lett. **72**, 627 (1998).

[39] S. L. McCall and P. M. Platzman, Phys. Rev. Lett. **67**, 2017 (1991).

[40] W. M. Robertson, G. Arjavalingam, R. D. Meade, K. D. Brommer, A. M. Rappe, and J. D. Joannopoulos, Phys. Rev. Lett. **68**, 2023 (1992).

[41] S. Fan, P. R. Villeneuve, and J. D. Joannopoulos, J. Appl. Phys. **78**, 1415 (1995).

[42] M. M. Sigalas, C. M. Soukoulis, C. T. Chan, and D. Turner, Phys. Rev. B **53**, 8340 (1996).

[43] M. M. Sigalas, C. M. Soukoulis, C. T. Chan, and K. M. Ho in *Photonic Band Gap Materials*, p. 563, ed. by C. M. Soukoulis (Kluwer, Dordrecht, 1996).

[44] E. Yablonovitch, T. J. Gmitter, R. D. Meade, A. M. Rappe, K. D. Brommer, and J. D. Joannopoulos, Phys. Rev. Lett. **67**, 3380 (1991).

[45] R. D. Meade, K. D. Brommer, A. M. Rappe, and J. D. Joannopoulos, Phys. Rev. B **44**, 13772 (1991).

[46] E. Ozbay, G. Tuttle, M. M. Sigalas, C. M. Soukoulis, and K. M. Ho, Phys. Rev. B **51**, 13961 (1995).

[47] S. John and J. Wang, Phys. Rev. Lett. **64**, 2418 (1990); S. John, Physica B **175**, 87 (1991); S. John and J. Wang, Phys. Rev. B **43**, 12772 (1991).

[48] G. Kurizki, Phys. Rev. A **42**, 2915 (1990).

[49] J. P. Dowling and C. M. Bowden, J. Opt. Soc. Am. B **10**, 353 (1993).

[50] John David Jackson, *Classical Electrodynamics* (Wiley, New York, 1962).

[51] N. W. Ashcroft and N. D. Mermin, *Solid State Physics* (Saunders College, Philadelphia, 1976).

[52] J. B. Pendry and A. MacKinnon, Phys. Rev. Lett. **69**, 2772 (1992).

[53] N. Stefanou, V. Karathanos and A. Modinos, J. Phys.: Condens. Matter **4**, 7389 (1992).

[54] J. B. Pendry, J. Phys.: Condens. Matter **8**, 1085 (1996).

[55] K. S. Yee, IEEE Trans. Antennas and Propagation **14**, 302 (1966).

[56] Allen Taflove, *Computational Electrodynamics: The Finite-Difference Time-Domain Method* (Artech House, Boston, 1995).

[57] C. T. Chan, Q. L. Yu, and K. M. Ho, Phys. Rev. B **51**, 16635 (1995).

[58] Cheryl V. Hile and William L. Kath, J. Opt. Soc. Am. B **13**, 1135 (1996).

[59] Peter M. Goorjian and Allen Taflove, Opt. Lett. **17**, 180 (1992).

[60] Richard W. Ziolkowski and Justin B. Judkins, J. Opt. Soc. Am. B **10**, 186 (1993).

[61] Edward A. Lacy, *Fiber Optics* (Prentice-Hall, Englewood Cliffs, N. J., 1982).

[62] Y. R. Shen, *The Principles of Nonlinear Optics* (Wiley, New York, 1984).

[63] Max Schubert and Bernd Wilhelmi, *Nonlinear Optics and Quantum Electronics* (Wiley-Interscience, New York, 1986).

[64] P. N. Butcher and D. Cotter, *The Elements of Nonlinear Optics* (Cambridge University Press, New York, 1990).

[65] Alan C. Newell and Jerome V. Moloney, *Nonlinear Optics* (Addison-Wesley, Redwood City, CA, 1992).

[66] T. H. Maiman, Nature **187**, 493 (1960).

[67] N. Bloembergen, *Nonlinear Optics* (Benjamin, Reading, Massachusetts, 1965).

[68] Hyatt M. Gibbs, *Optical Bistability: Controlling Light with Light* (Academic, Orlando, FL, 1985).

[69] A. Hasagawa, *Optical Solitons* (Springer-Verlag, Berlin, 1989).

[70] G. P. Agrawal, *Nonlinear Fiber Optics* (Academic Press, Boston, 1989).

[71] Govind P. Agrawal and Robert W. Boyd, *Contemporary Nonlinear Optics* (Academic, San Diego, CA, 1992).

[72] M. Bass, P. A. Franken, A. E. Hill, C. W. Peters, and G. Weinrich, Phys. Rev. Lett. **8**, 18 (1962).

[73] P. A. Franken, A. E. Hill, C. W. Peters, and G. Weinrich, Phys. Rev. Lett. **7**, 118 (1961).

[74] N. Zabusky and M. D. Kruskal, Phys. Rev. Lett. **15**, 240 (1965).

[75] Matrin M. Fejer, Physics Today **47** No. 5, 25 (1994).

[76] Mohammed N. Islam, Physics Today **47** No. 5, 34 (1994).

[77] H. G. Winful, J. H. Marburger, and E. Garmire, Appl. Phys. Lett **35**, 379 (1979); H. G. Winful, and G. D. Cooperman, Appl. Phys. Lett **40**, 298 (1982).

[78] N. D. Sankey, D. F. Prelewitz, and T. G. Brown, Appl. Phys. Lett. **60**, 1427 (1992).

[79] J. He, M. Cada, M.-A. Dupertuis, D. Martin, F. Morier-Genoud, C. Rolland, A. J. SpringThorpe, Appl. Phys. Lett. **63**, 866 (1993).

[80] Wei Chen and D. L. Mills, Phys. Rev. B **36**, 6269 (1987); Phys. Rev. Lett. **58**, 160 (1987).

[81] D. L. Mills and S. E. Trullinger, Phys. Rev. B **36**, 947 (1987).

[82] C. Martijn de Sterke and J. E. Sipe, Phys. Rev. A **42**, 2858 (1990).

[83] A. B. Aceves, C. De Angelis and S. Wabnitz, Opt. Lett. **17**, 1566 (1992).

[84] Sajeev John and Neşet Aközbek, Phys. Rev. Lett. **71**, 1168 (1993); Neşet Aközbek and Sajeev John, Phys. Rev. E **57**, 2287 (1998).

[85] B. J. Eggleton, C. Martijn de Sterke, R. E. Slusher, J. Opt. Soc. Am. B **14**, 2980 (1997).

[86] C. Martijn de Sterke and J. E. Sipe, in *Progress in Optics*, edited by E. Wolf (Elsevier, Amsterdam, 1994), Vol. 33.

[87] G. Mie, Ann. Phys. (Leipzig) **25**, 377 (1908); C. F. Bohren and D. R. Huffman, *Absorption and Scattering of Light by Small Particles* (J. Wiley, New York, 1983).

CHAPTER 2. WAVE PROPAGATION IN NONLINEAR MULTILAYER STRUCTURES

A paper published in the journal of Physical Review B [1]

E. Lidorikis, Qiming Li, and C. M. Soukoulis

Abstract

We investigate the adequacy of the Kronig-Penney δ-function model in describing the electromagnetic wave propagation in periodic structures consistent of thin layers of materials with an intensity-dependent dielectric constant. We find the model captures the most essential features of nonlinear response to radiation. Excellent agreement is found between the results from the δ-function model and the exact solutions of nonlinear wave equations. However, discrepancies do exist below the bottom of transmission bands due to the rigidness of the band edge in the δ-function model. Consequently, gap solitons cannot form in the δ-function model when the nonlinear Kerr coefficient is positive.

Introduction

The presence of nonlinearity is known to lead to much richer and more complex optical response to radiation. One such phenomenon known as bistability, in which two possible output states exist for a single input, promises important potential applications in ultrafast optical switches[1]. Bistable response can be observed in simple structures such as the traditional nonlinear Fabry-Perot etlons[2] or in distributed feedback structures such as multilayered systems

---

[1] PRB **54**, 10249 (1996)

consisting of alternating nonlinear dielectric materials[3]. In essence, the bistable response results from the modulation of transmission by an intensity-dependent phase shift. The multilayer structure can also act as a Bragg reflector and offers additional transmission modes known as 'gap solitons' within the stop band[4]. The optimal coupling of these localized modes to radiation may lead to switching thresholds orders of magnitude smaller than achievable in the transmission band[15].

Recently, the global transmission diagrams of multilayer structures with a Kerr nonlinearity were investigated within a Kronig-Penney δ-function model[6]. It was found that the effectiveness of the nonlinearity is strongly modified by the frequency. In addition the nonlinear responses of the positive and the negative nonlinear media are distinctly different due to the modulation of the dispersion relation by the superlattice. Many dominant features were understood through the analysis of stable periodic orbits of the corresponding nonlinear mapping as well as the analysis of various spectrum and stability bounds of the nonlinear difference and the corresponding differential equations. A simple and intuitive picture of the formation of gap solitons and soliton trains, based on a mechanical analogy, was also presented. These understanding may prove useful for incorporating nonlinearity in systems of higher dimensions, for example, in photonic band gap structures[7].

All these results were based on the Kronig-Penney δ-function model. Such a model offers the advantage of being amenable for some analytical treatment and is expected to work well when the nonlinear layer is thin compared with the wavelength of the incident wave. However, to our knowledge, its general adequacy as well as its limitations has not been previously investigated. In this brief report, we compare the results derived from the Kronig-Penney $\delta-$function model with direct numerical solutions of wave propagation in nonlinear superlattices of finite thickness. We find the Kronig-Penney δ-function model captures most of the essential features of the nonlinear response in superlattice structures. The global transmission diagrams from the two methods are in excellent agreement with each other. However, some disagreement does exist, most significantly below the bottom of the transmission band. This difference is entirely due to the rigidness of the band edge in the Kronig-Penney δ-function model, an unphysical feature that affects the conclusion regarding the existence of gap solitons when the Kerr nonlinearity is positive.

Formalism

The formulation of the steady state plane wave transmission problem in nonlinear superlattices has been described in detail elsewhere[6]. The structure consists of alternating layers of two dielectric materials, one of which has an intensity-dependent Kerr nonlinearity, $\epsilon = \epsilon_0 + \alpha_2 |E|^2$. For normal incidence of a plane wave, the electric field amplitude E(x) satisfies the equation

$$\frac{d^2E(x)}{dx^2} + \frac{\omega^2}{c^2}\epsilon(x)E(x) = 0, \tag{1}$$

where ω is the optical frequency, and c is the vacuum speed of the light. $\epsilon(x)$ is the dielectric constant which varies along the structure and depends on the local field intensity at nonlinear layers. The transmission characteristics are obtained by solving Eq. (1) under the boundary condition,

$$E(x,t) = \begin{cases} E_0 e^{i(kx-\omega t)} + E_r e^{-i(kx+\omega t)} & \text{for } x < 0 \\ E_t e^{i(kx-\omega t)} & \text{for } x > L \end{cases}, \tag{2}$$

where E_0,E_t, and E_r are the amplitude of the incident, transmitted, and reflected wave, respectively. Wave vector $k = \omega/c$, and L is the total length of the structure. The transmission coefficient T is defined as $T = |E_t|^2/|E_0|^2$.

Eq. (1) can be solved[4] by matching at the layer interfaces analytical solutions in each nonlinear layer, which may be expressed in terms of the Jacobi elliptic functions[4]. A much simpler numerical approach, however, is to first discretize the structure and then iterate the difference equation numerically across the sample, starting from the output field E_t. Our numerical results are obtained this way.

The Kronig-Penney δ-function model, on the other hand, describes an system with infinitesimally thin nonlinear layers[6]. In this model, the electric field obeys,

$$\frac{d^2E(x)}{dx^2} + \frac{\alpha\omega^2}{c^2}\sum_{n=1}^{N}(1+\lambda|E(x)|^2)E(x)\delta(x-n) + k^2E(x) = 0. \tag{3}$$

This can be easily rewritten[6] as a difference equation in terms of the field at the nonlinear layers, E_n,

$$E_{n+1} + E_{n-1} = (2\cos k - \alpha k \sin k(1 + \lambda |E_n|^2))E_n, \tag{4}$$

where $\alpha = \epsilon_0 a$ and $\lambda = \alpha_2/\alpha$. a is the thickness of the nonlinear layers. We have assumed the linear medium is a vacuum ($\epsilon = 1$), and the distance between the neighboring nonlinear layers, d=a+b, is taken as one unit length. The δ-function model can be viewed as an approximation when the nonlinear layer is thin compared with the effective wavelength within it.

Results and discussion

In order to compare the results obtained for the δ-function model with the results obtained for the finite width nonlinear layers, we have solved numerically the wave equation Eq. (1) for a system with nonlinear layers of width 0.1 unit length and linear layers ($\epsilon = 1$) of width 0.9 unit length. The global transmission diagrams in the $k - E_t$ plane for the positive Kerr coefficient is shown in Fig. 1(b) as a grey scale plot, along with the results from the δ-function model (Fig. 1(a)). The general features are remarkably similar. Good agreement is also obtained when the Kerr nonlinear coefficient is negative (Fig. 2). These transmission diagrams show features that have been understood through analysis of stable periodic orbits and various spectrum and stability bounds[6].

A remarkable phenomenon occurred in the nonlinear response of superlattice structures is the existence of localized gap soliton solutions in the stop band of the linear regime[4]. In the previous study[6] with the δ-function model, only in the negative Kerr media did we find gap soliton solutions. This is in disagreement with the conclusion of Chen and Mills that soliton solutions exist regardless of the sign of the nonlinearity[4]. In Figure 3, we show the transmission diagram within the stop band for superlattice of finite widths with a positive nonlinear coefficient. Clearly, resonant trajectories exists. Examination of the solutions show well localized waves symmetrically distributed at the center of the structure. Different resonance bands correspond to solutions containing different number of solitons, analogous to the situation with negative nonlinearity. Here, the inadequacy of the δ-function model shows up, by not giving soliton solutions in the gap. For negative nonlinear coefficient, the transmission diagram of the superlattice structure again is in good agreement with that of the δ-function model (see Fig. 4).

To understand why the δ-function model fails to describe the formation of gap soliton in superlattices with positive nonlinear coefficient, we have to examine the physical mechanism in which gap solitons form when nonlinearity is incorporated in the model. This was elucidated with a mechanical analogy in the previous work[6]. The soliton forms only when the frequency is in the forbidden region of the spectrum in a linear system, i.e., in the gap. As the wave intensity varies along the structure, the dielectric constant of the nonlinear layers changes accordingly. Consequently the location of the effective transmission bands moves. For the soliton to form, the linearized transmission band has to shift in the right direction such that the incident frequency merges into it. This is illustrated in Fig. 5 in which we show a single soliton profile (Fig. 5(a)) in the stop band. The corresponding effective transmission band edges are shown in Fig. 5(b), calculated from the linear dispersion relation using the local dielectric constant. Clearly, as the soliton intensity increases, the effective transmission band shifts towards the incident frequency and eventually takes it completely in the vicinity of the center of the soliton.

Examination of the effective transmission bands as a function of the effective dielectric constant in the nonlinear layers shows clearly the difference between the δ-function model and the more realistic multilayer system (Fig. 6). For the negative nonlinearity (the portion below the dotted line), the collapse of the gap is described well with the δ-function (Fig. 6(a)). But for positive nonlinearity (the portion above the dotted line), the shift of bottom of the bands towards lower frequency in the real system is completely missed in the δ-function. This is not surprising, since the bottom of the band in the δ-function model is always located at $k = m\pi$. Thus, the rigidness of the band edge in the δ-function model prevents the frequency below the bottom of the band from merging into the effective transmission band when the field intensity increases and therefore hinders the formation of gap solitons.

In Fig. 7, we compare the transmission coefficient as a function of the transmitted amplitude obtained from the exact solution (Fig. 7(b)) and from the δ-function model (Fig. 7(a)), for a negative nonlinearity with frequency below the bottom of the second band. Again, qualitative features are the same. Notice the total transmission peaks at the resonance of gap soliton solutions[8].

We have also investigated systems with thicker nonlinear layers and found qualitatively similar behavior. Qualitative agreement of course worsens as the nonlinear layer thickness increases. However, the essential features remain the same. Thus the δ-function model seems to be sufficiently adequate for a qualitative study of nonlinear response to radiation.

Conclusions and acknowledgments

In conclusion, we have examined many aspects of the nonlinear response in multilayer structures and found the δ-function model quite adequate, aside from the obvious deficiency of processing a rigid bottom band edge. The model captures the most essential features in the transmission characteristics and therefore should be widely used due to its simplicity.

Ames Laboratory is operated for the U. S. Department of Energy by Iowa State University under contract No. W-7405-ENG-82. This work is supported by the Director of Energy Research, Office of Basic Energy Science, and Advanced Energy Projects.

Bibliography

[1] H. M. Gibbs, *Optical Bistability: Controlling Light with Light* (Academic, Orlando, FL, 1985).

[2] H. M. Gibbs, S. L. McCall, and T. N. C. Venkatesant, Phys. Rev. Lett. **36**, 1135 (1976).

[3] H. G. Winful, J. H. Marburger, and E. Garmire, Appl. Phys. Lett. **35**, 379 (1979).

[4] Wei Chen and D. L. Mills, Phys. Rev. B **36**, 6269 (1987); Phys. Rev. Lett. **58**, 160(1987).

[5] C. Martine de Sterke and J. E. Sipe, in *Progress in Optics*, Vol. 33. edited by E. Wolf, (Elsevier, Amsterdam, 1994).

[6] Qiming Li, C. T. Chan, K. M. Ho, and C. M. Soukoulis, Phys. Rev. B**53**, (1996)

[7] *Photonic Band Gaps and Localization*, edited by C. M. Soukoulis (Plenum, New York, 1993); and Proceeding of the NATO ASI on "Photonic Band Gap Materials" (unpublished).

[8] In Fig. 8-9 of Ref. 6, total transmission was not reached in some cases, due to an inappropriate boundary condition. This, however, does not affect any of the conclusions.

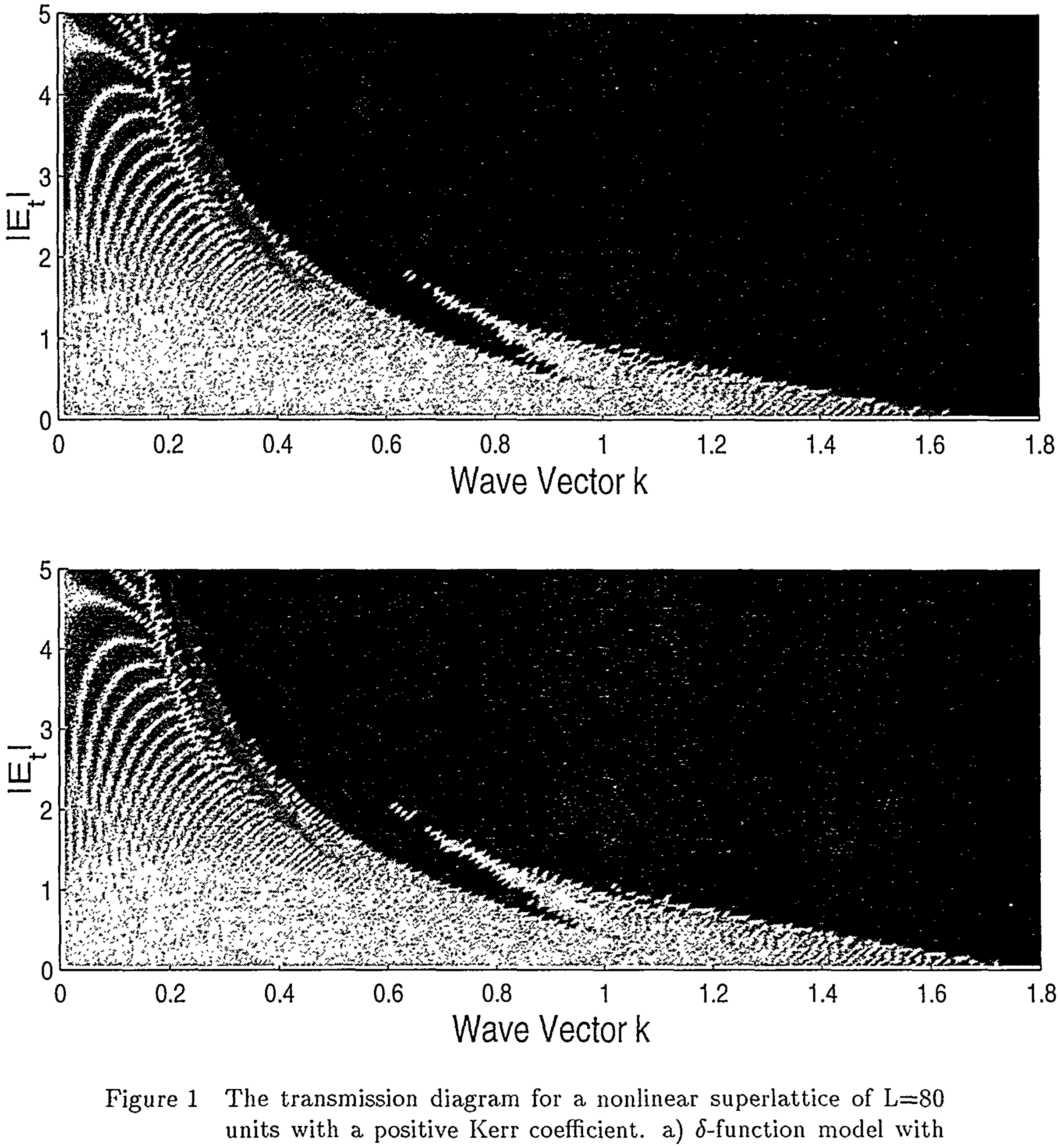

Figure 1 The transmission diagram for a nonlinear superlattice of L=80 units with a positive Kerr coefficient. a) δ-function model with $\alpha = 1$, and b) exact solutions with linear layers of thickness 0.9, $\epsilon = 1$, and nonlinear layers of thickness 0.1 and $\epsilon_0 = 10$. Higher bands (not shown) show similar behavior.

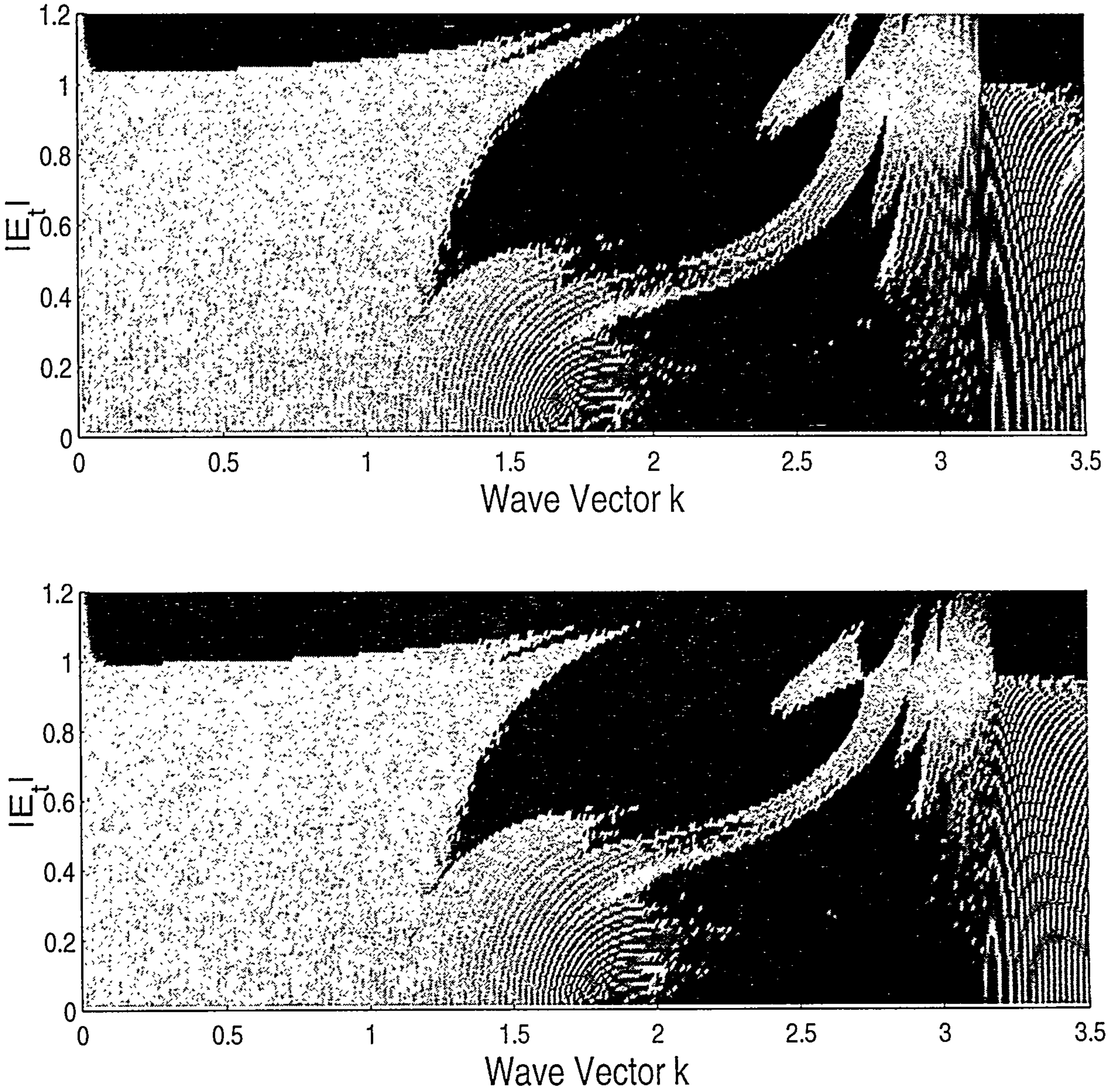

Figure 2 The transmission diagram for a nonlinear superlattice of L=80 units with a negative Kerr coefficient. a) δ-function model with $\alpha = 1$. b) linear layers of thickness 0.9, $\epsilon = 1$, and nonlinear layers of thickness 0.1 and $\epsilon_0 = 10$.

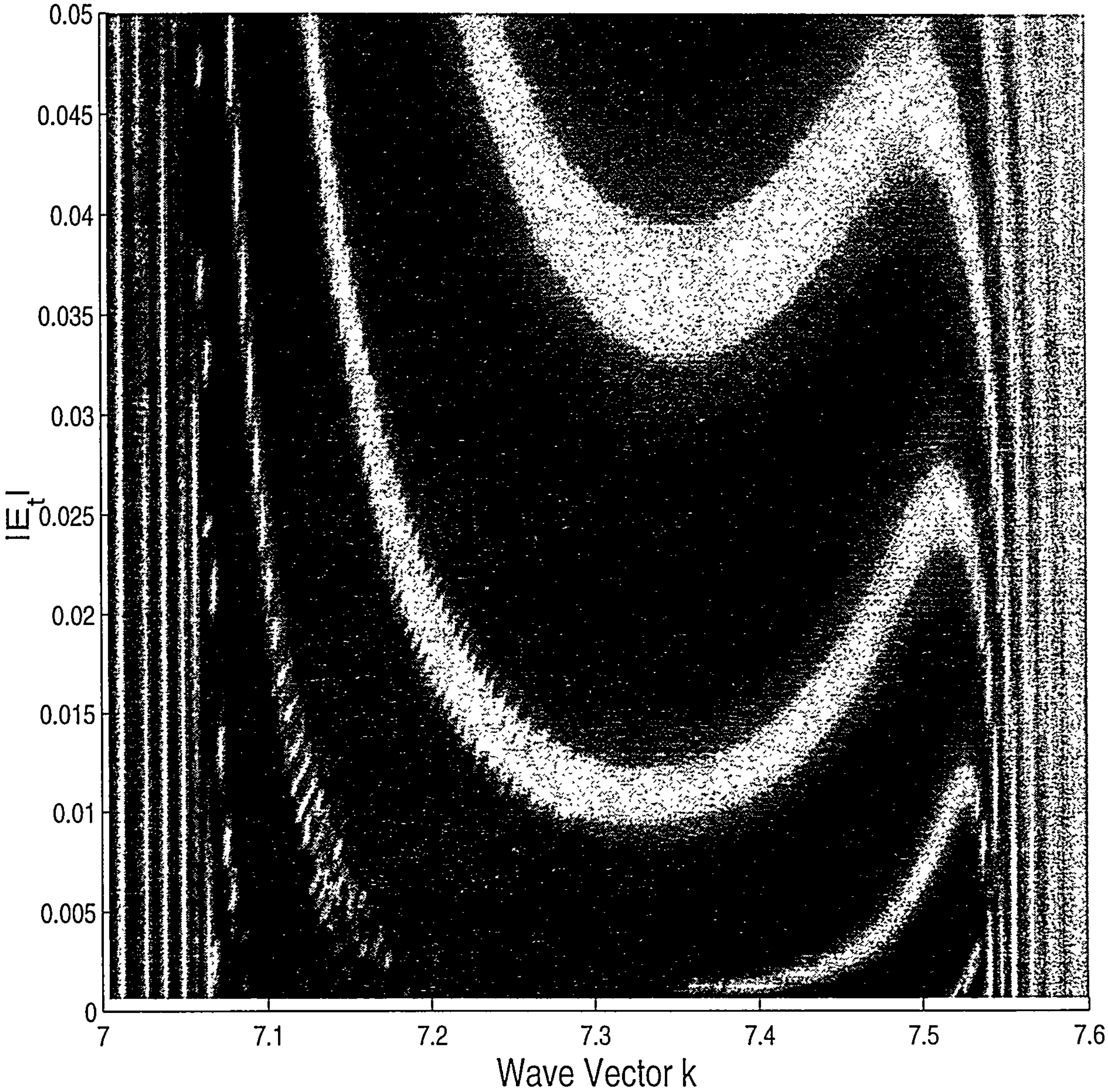

Figure 3 The resonant transmission trajectories of single and multiple solitons in the third stop-band of a nonlinear finite thickness superlattice of L=80 units with a positive Kerr coefficient. Linear layers of thickness 0.9, $\epsilon = 1$, and nonlinear layers of thickness 0.1 and $\epsilon_0 = 16$.

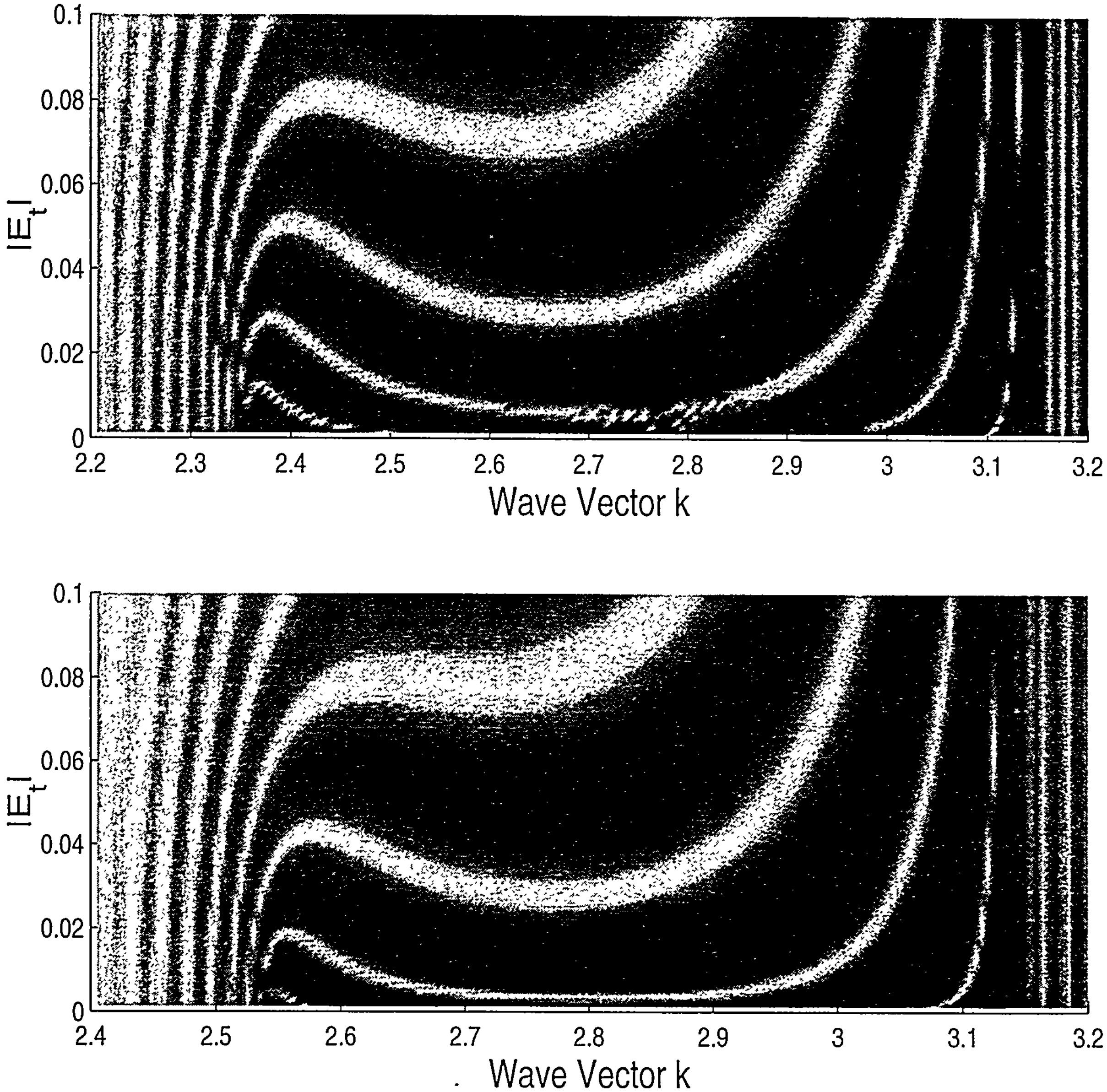

Figure 4 The resonant transmission trajectories of single and multiple solitons in the first stop-band of a L=80 multilayer system with a negative Kerr coefficient. a) δ-function model with $\alpha = 0.35$. b) finite thickness bilayers with linear layers of thickness 0.9, $\epsilon = 1$, and nonlinear layers of thickness 0.1 and $\epsilon_0 = 3.5$.

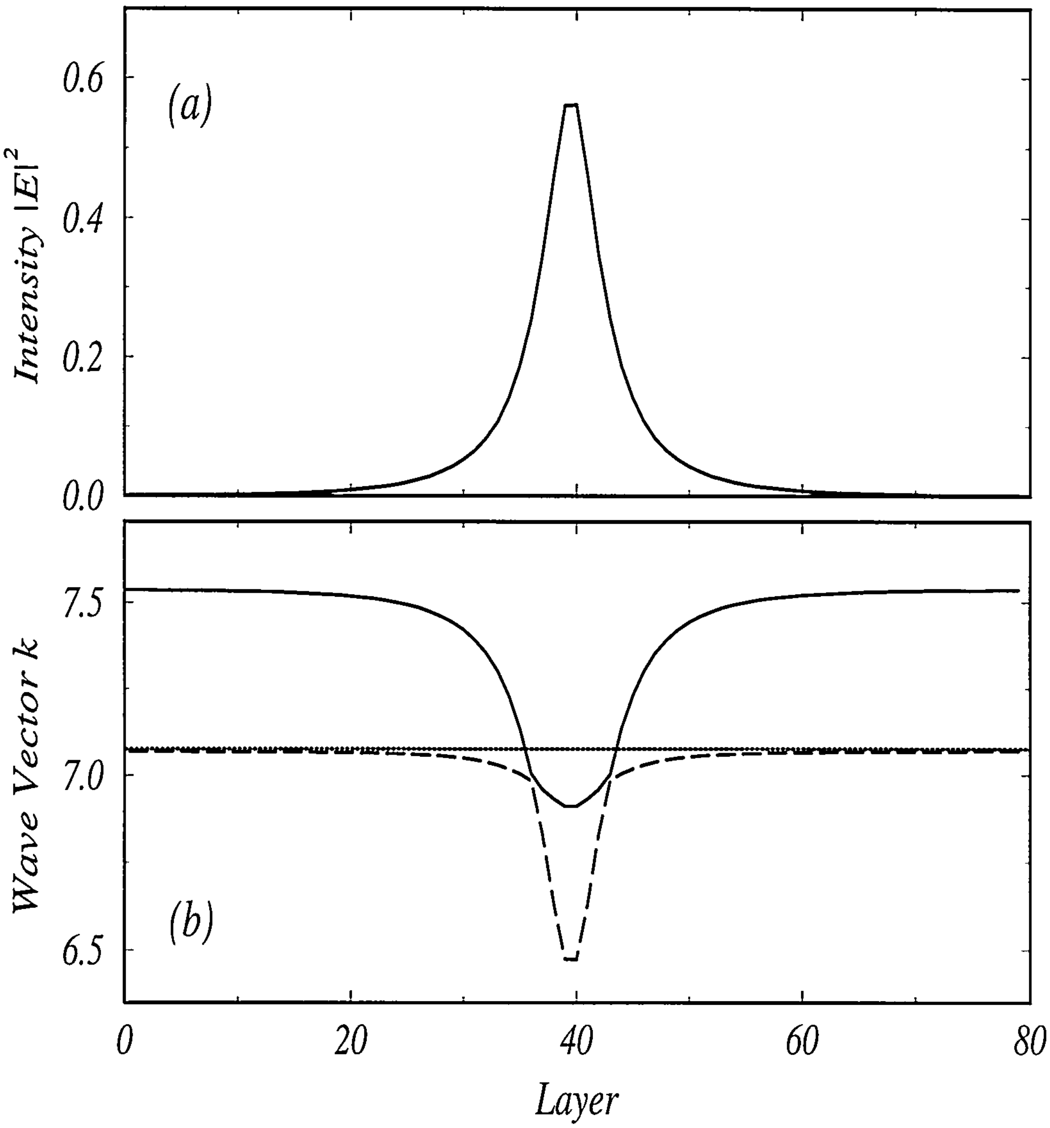

Figure 5 Illustration of gap soliton formation in a system with L=80 layers with positive nonlinearity. Linear layers of thickness 0.9, $\epsilon = 1$, and nonlinear layers of thickness 0.1 and $\epsilon_0 = 16$. k=7.07369 and E_t=0.01. a) profile of a gap soliton, and b) the local effective stop-band edges as determined from the soliton profile. The stop-band extends from the dashed line (low frequency stop-band edge) to the solid line (high frequency stop-band edge). The thin line is the incident frequency. Clearly, the incident frequency merges inside the effective transmission band around the center of the soliton.

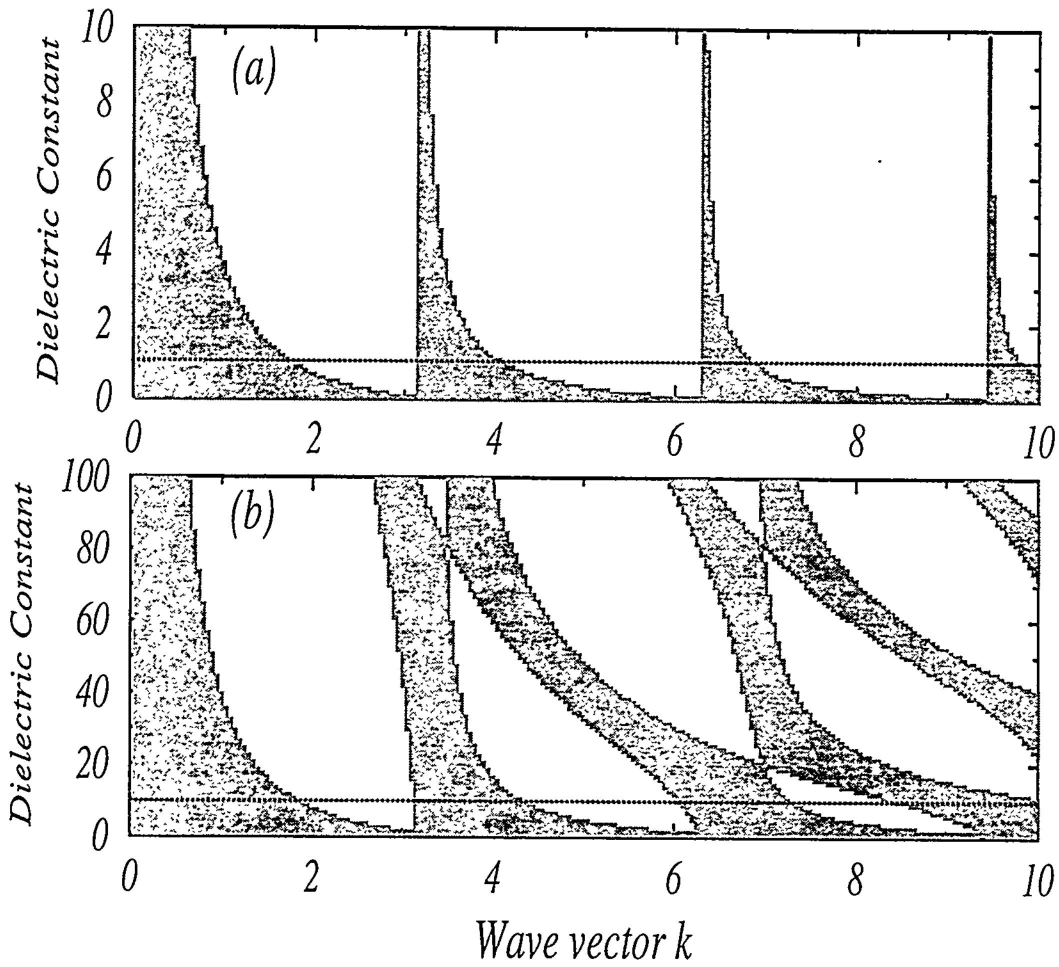

Figure 6 The transmission band as a function of the effective dielectric constant at the nonlinear layers. L=80 a) δ-function model with $\alpha = 1$. b) linear layers of thickness 0.9, $\epsilon = 1$, and nonlinear layers of thickness 0.1 and $\epsilon_0 = 10$. The horizontal line indicates the bands in the linear regime.

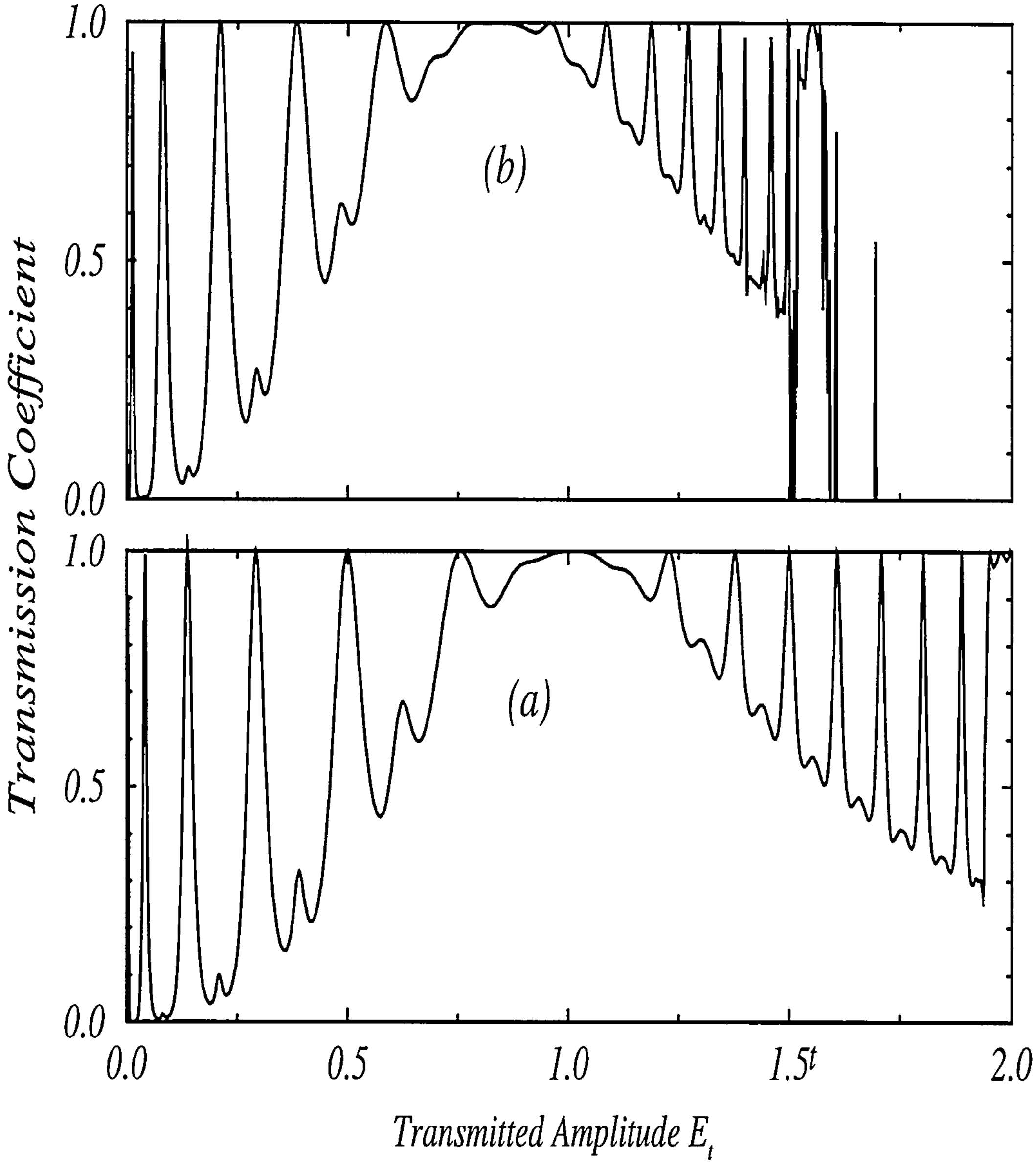

Figure 7 Transmission coefficient as a function of the transmitted amplitude E_t, for L=80 layer system with a negative nonlinearity. k=3.0. a) δ-function model with $\alpha = 0.35$. b) linear layers of thickness 0.9, $\epsilon = 1$, and nonlinear layers of thickness 0.1 and $\epsilon_0 = 3.5$.

CHAPTER 3. OPTICAL NONLINEAR RESPONSE OF A SINGLE NONLINEAR DIELECTRIC LAYER SANDWICHED BETWEEN TWO LINEAR DIELECTRIC STRUCTURES

A paper published in the journal of Physical Review B [1]

E. Lidorikis, K. Busch [2], Qiming Li, C. T. Chan [3], and C. M. Soukoulis

Abstract

We consider the general problem of electromagnetic wave propagation through a one dimensional system consisting of a nonlinear medium sandwiched between two linear structures. Special emphasis is given to systems where the latter comprise Bragg-reflectors. We obtain an exact expression for the nonlinear response of such dielectric superlattices when the nonlinear impurity is very thin, or in the δ-function limit. We find that both the switching-up and switching-down intensities of the bistable response can be made very low, when the frequency of the incident wave matches that of the impurity mode of the structure. Numerical results for a nonlinear layer of finite width display qualitatively similar behavior, thus confirming the usefulness of the simpler δ-function model. In addition, an analytical solution for the resonance states of an infinitely extended finite width superlattice with a finite width nonlinear impurity is presented.

---

[1] PRB **56**, 15090 (1997)

[2] Universität Karlsruhe, Germany. Also carried out most of the work in the second part.

[3] Hong Kong University, China

Introduction

Dielectric materials with an intensity-dependent dielectric constant are well known for their complex response to radiation. Exciting features such as bistability, multistability, optical limiting etc. have been predicted theoretically [1, 2] and observed experimentally [3, 4, 5]. Promising future applications include optical switches and transistors, pulse shapers as well as memory elements. Already quite simple structures like the traditional Fabry-Perot etalons [3] or multilayered structures of alternating nonlinear dielectric materials [3] exhibit such a behavior. The common characteristic of all nonlinear optical devices is the feedback mechanism, necessary to enhance the nonlinear effects. Crudely speaking, there exist two types of realizations: In the case of a "localized" feedback structure a homogeneous nonlinear medium is placed between two reflectors (mirrors [3, 4] or Bragg- reflectors [5]), while "distributed" feedback mechanisms are realized through a periodic modulation of the linear part of the nonlinear materials' refractive index [1]. Similar studies have been done for the electronic response in a one-dimensional nonlinear lattice [9, 10, 11], as well as for a linear lattice with nonlinear impurities[12].

The linear (or low intensity) properties of the feedback mechanism are important for the nonlinear response of the device. For instance, a distributed feedback structure brings about a photonic band gap [9, 14], where certain modes are forbidden while others propagate freely. For frequencies inside the transmission band, bistability results from a modulation of transmission by an intensity dependent phase shift. For frequencies inside the stop gap of the linear system, bistability and resonance transmission is achieved via gap soliton formation [10, 16]. However, nonlinear media are usually quite lossy and, thus, it is important to find ways of keeping the amount of nonlinear material small while still retaining sizable nonlinear effects. Furthermore, the successful use of optical switches depends crucially on a low threshold, i.e. low "switching" intensities. The above considerations lead to the question whether a single nonlinear layer, suitably supplied with a feedback mechanism, may be sufficient for optical switching devices. In this paper we present the results of our investigation of this and several related problems.

The paper is divided into two parts: The first part deals with the general case of a "localized" feedback structure when the nonlinear layer is very thin, or in the δ-function approximation. We will give arguments why a system consisting of a nonlinear layer sandwiched between Bragg-reflectors may be considered the most efficient "localized" feedback structure, as well as which parameters of the system determine the bistability threshold. We also demonstrate the usefulness of the δ-function approximation by comparing with numerical results for a nonlinear layer of finite width. However, a finite nonlinear layer always exhibits multistability. This is illustrated in the second part of this paper, where we present an analytical solution for the resonance states of an infinite superlattice with a finite width nonlinear impurity layer. These are modulated band gap impurity modes and correspond to the the transmission resonances in the multistable input vs output diagram. Finally, a comparison between the analytical solution for the infinite superlattice with numerical results for a finite superlattice shows very good agreement.

Very thin nonlinear layer

Many features of wave propagation through one dimensional nonlinear structures can most conveniently be investigated and understood within a nonlinear Kronig-Penney δ-function model [11]. Although discrepancies with the more realistic finite width models do exist, it has been demonstrated that the δ-function model captures most of the essential features of nonlinear response to radiation [12]. In this section we will consider a very thin nonlinear layer centered at the origin. The nonlinearity is expressed in first order by an intensity dependent term in the dielectric function $\epsilon(x)$:

$$\epsilon(x) \approx \epsilon_0 (1 + \lambda |E(x)|^2)\, \delta(x) \tag{1}$$

Here ϵ_0 is defined as the limit $n^2 d \to \epsilon_0$ for $n \to \infty,\ d \to 0,$ of a finite width layer of extent d and index of refraction n, and $\epsilon_0 \lambda$ is the corresponding nonlinear Kerr coefficient.

We will first discuss the problem of a single nonlinear δ-function. More insight is obtained from a general discussion of a δ-function nonlinear layer sandwiched between two linear structures. It will be shown that the equation relating input and output intensities has the same form as for a single nonlinear δ-function except for a parameter renormalization. Also, a very useful phase diagram for the onset of bistability in terms of the linear properties of the system will be derived. From this it follows that the most interesting physics appears when the linear structures on the two sides of the nonlinear layer are identical Bragg- reflectors. Assuming the latter to consist of very thin layers, we arrive at a remarkably simple but very rich result for the input- output intensity relation.

Single nonlinear δ-function

We first consider electromagnetic wave propagation through a single δ-function with an intensity dependent dielectric strength as given by Eq. (1). This is schematically depicted in Fig. 1. Our interest lies in the steady state response of the system. Let a plane wave $E_0 e^{-ikx}$ with wave number $k = \omega/c$ be incident from the right. This gives rise to a reflected wave, $E_r e^{ikx}$, as well as to a transmitted wave, $E_t e^{-ikx}$. Solving the Maxwell equation with a single nonlinear δ- function layer at $x = 0$ will yield a relationship between the incident and transmitted intensity, $Y = |E_0|^2$ and $X = |E_t|^2$, respectively:

$$Y = X\left[1 + \tau\,(1 + \lambda X)^2\right] \quad , \tag{2}$$

where $\tau \equiv \epsilon_0^2 k^2/4$ is related to the transmission coefficient $|T_0|^2$ of the corresponding linear (λ=0) system, $\tau = (1 - |T_0|^2)/|T_0|^2$. The system will exhibit bistability if we can have more than one output for a given input. This will be true if Y is a non-monotonic function of X. We find a physical solution for $dY/dX = 0$ only for $\lambda < 0$ and $\tau > 3$:

$$X_\pm = \frac{2 \pm \sqrt{1 - 3/\tau}}{3|\lambda|} \tag{3}$$

The absence of bistability for a positive Kerr-coefficient is one of the artifacts of the δ-function approximation. We will see later that this restriction is lifted, once the nonlinear δ- function is placed between two linear systems with nonzero reflection coefficients. The nonlinear response of such a system with negative λ is shown in the input vs output diagram in Fig. 2a for various values of τ and λ.

The switching-up and switching-down intensities are given by $Y_\pm = Y(X_\mp)$, respectively. For $\tau = 3$ and $\lambda < 0$ we have the onset of bistability at $Y_+ = Y_- = 8/(9|\lambda|)$. As τ gets larger,

$Y_- \to 1/|\lambda|$ while $Y_+ \sim \tau/|\lambda|$. Note that for $Y = X = 1/|\lambda|$ we have resonance transmission. Thus for large τ (or equivalently for low linear transmission) the switching down intensity and the resonance intensity are the same. Clearly, the larger $|\lambda|$ is, the smaller the switching intensities are. Note further, that the resonance transmission intensities $Y = X = 1/|\lambda|$ correspond to $\epsilon(0) = 0$, i.e. the index mismatch between the δ-function and the background effectively disappears, leading to total transmission. On the other hand, for a finite width linear layer with dielectric constant $\epsilon = n^2$, the condition for resonance transmission is $2d = m\lambda_f$, where d is the width of the layer and $m\lambda_f$ is an integer multiple of the wavelength inside the dielectric material ($\lambda_f = 2\pi c/n\omega$) [3]. If we incorporate a nonlinear coefficient in the dielectric constant ($\epsilon(x) = n^2(1 + \lambda|E(x)|^2)$), then for suitable choices of the parameters we can have bistability (and even multistability) for both negative and positive Kerr medium. For example, if $2d < \lambda_f$ and $\lambda > 0$, then effectively the dielectric constant will get larger, yielding a smaller average effective wavelength $\langle\lambda_f\rangle$. For some intensity we should expect the resonance condition to be "effectively" satisfied, and, as a consequence, get a transmission resonance. Higher order resonances are also expected giving rise to multistability. For a negative Kerr-coefficient and $2d < \lambda_f$ we should not expect bistability, as correctly pointed out by Chen and Mills [2], unless we allow the unphysical situation at which the intensities become large enough to make $\langle n_{\text{eff}}^2\rangle \leq 1$. Only then we would get bistability, and this would be the exact correspondence to the δ-function case. For a positive Kerr-coefficient, however, bistability should always be expected (although some times only at unrealistically high intensities), a feature that is absent in the δ-function model.

In Fig. 2b we show the transmission diagram for a finite width dielectric slab for $d = 0.6\lambda_f$ and various values of linear transmission coefficient and nonlinear Kerr coefficient. Although this is not the exact analog of Fig. 2a, it is remarkable that both models show a similar dependence on their linear transmission properties. We also find that for larger intensities the negative nonlinear medium does not exhibit multistability, while a positive nonlinear medium will always exhibit multistability, as can be seen in the inset graph in Fig. 2b.

The unphysical condition for resonance transmission in the single nonlinear δ-function case can be lifted if we sandwich the δ-function between two linear systems. Bistability will then occur as a result of the intensity dependent phase shift that the δ-function will introduce between the two linear systems, which will alter their transmission characteristics. As we will see in the next section, this arrangement is also optimal for obtaining lower switching intensities.

Nonlinear δ-function sandwiched between two linear systems

Let us now consider a more general geometry as shown in Fig. 3, where a nonlinear δ-function is sandwiched between two linear systems, characterized by the reflection and transmission amplitudes, r_i and t_i $(i = 1, 2)$, respectively. Generally, for a linear system, with incident and reflected plane waves from it's left Ae^{ikx} and Be^{-ikx} respectively, and incident and reflected plane waves from it's right De^{-ikx} and Ce^{ikx} respectively, the relation between the field amplitudes is described by the transmission matrix:

$$\begin{pmatrix} C \\ D \end{pmatrix} = \begin{pmatrix} 1/t^* & -r/t \\ -(r/t)^* & 1/t \end{pmatrix} \begin{pmatrix} A \\ B \end{pmatrix} \tag{4}$$

Just as before, we assume this composed object to be illuminated from the right by a plane wave with amplitude E_0. The corresponding reflected and transmitted wave amplitudes are denoted by E_r and E_t, respectively. Then, the relation between the output intensity $X = |E_t|^2$ and the input intensity $Y = |E_0|^2$ can be obtained straightforwardly by properly matching the values of the fields at the origin:

$$Y = X\left[\gamma + \tau'\left(1 + \lambda' X\right)^2\right] \quad . \tag{5}$$

Note that Eq. (5) has exactly the same structure as Eq. (2). Thus, we have shown that the introduction of the linear structures leads to a renormalization of the quantities in Eq. (2): $1 \to \gamma$, $\tau \to \tau'$ and $\lambda \to \lambda'$. The quantities γ, τ' and λ' are given by the following expressions

$$\gamma = \frac{1/\left(|T|^2\,|T_0|^2\right) - \mathrm{Re}^2\left[1/\left(T^* T_0\right)\right]}{|1/T_0 - 1/T|^2} \tag{6}$$

$$\tau' = \frac{\left(1/\,|T_0|^2 - \mathrm{Re}\left[1/(T^* T_0)\right]\right)^2}{|1/T_0 - 1/T|^2} \tag{7}$$

$$\lambda' \;=\; \lambda \, |1/t_1 - r_1^*/t_1^*|^2 \, |1/T_0 - 1/T|/\sqrt{\tau'} \;\;, \tag{8}$$

where T is the linear transmission amplitude for the system without the δ-function at the origin ($\epsilon_0 \equiv 0$):

$$\frac{1}{T} = \frac{1}{t_1\, t_2} + \frac{r_1^*\, r_2}{t_1^*\, t_2} \;\; . \tag{9}$$

Similarly, T_0 is the *linear* transmission amplitude for the case with the δ-function at the origin ($\lambda \equiv 0$),

$$\frac{1}{T_0} = \frac{1}{T} - i\,\frac{k\,\epsilon_0}{2}\left(\frac{1}{t_1} - \frac{r_1^*}{t_1^*}\right)\left(\frac{1}{t_2} + \frac{r_2}{t_2}\right) \tag{10}$$

The conditions for bistability from Eq. (5) now read as:

$$\frac{\gamma}{\tau'} \;<\; \frac{1}{3}\;, \tag{11}$$

$$\lambda' \;<\; 0 \;\;, \tag{12}$$

thus, allowing bistability for positive Kerr-coefficients as well. We want to stress that the conditions for bistability depend on the transmission amplitudes of the linear systems with and without δ-function only. They can conveniently be rewritten in terms of the quantities R and θ which are defined via $1/T_0 = R\, e^{i\theta}/T$:

$$\frac{\sin^2\theta}{(R - \cos\theta)^2} \;\leq\; \frac{1}{3}\;, \tag{13}$$

$$\mathrm{sign}(\lambda)\left(1 - \frac{\cos\theta}{R}\right) \;<\; 0 \tag{14}$$

Fig. 4 shows the phase diagram for the onset of bistability derived from Eqs. (13) and (14). Obviously, the insertion of the linear part of the nonlinear δ-function has to sufficiently alter the total transmission amplitude $1/T$ in order for bistability to occur. This alteration may be achieved by a change in the total transmission, i.e. by changing R, and/or by introducing a phase shift θ.

One can get more explicit and transparent results when the linear systems each consist of a periodic arrangement of N linear δ- functions with a spacing a equal to the distance between the nonlinear δ-function and the two linear systems. We first consider the linear problem of N equally spaced δ-functions of dielectric strength ϵ_0. Between any two δ-functions in the linear structure the solution consists of two plane waves traveling in opposite directions. Using the boundary conditions we can eliminate the waves in the intermediate space and obtain a difference equation in terms of the field at the δ-function sites [11]

$$E_{n+1} + E_{n-1} = (2\cos k - \epsilon_0 k \sin k) E_n, \tag{15}$$

where we have assumed the space between two δ-functions to be vacuum and their separation to be a=1. Upon expressing all lengths in units of the lattice period ($a = 1$) and using the Bloch's theorem $E(x+1) = e^{iq}E(x)$ we arrive at the band structure equation which defines the Bloch wave vector q

$$\cos q = \cos k - \frac{1}{2}\epsilon_0\, k\, \sin k \tag{16}$$

The transmission bands are found by setting $|\cos q| \leq 1$.

We can easily generalize the above method to the present problem of $2N$+1 δ-functions utilizing the transfer matrix of each layer

$$\begin{pmatrix} E_{-N-1} \\ E_{-N} \end{pmatrix} = \mathcal{M}^N \begin{pmatrix} 2\cos q' & -1 \\ 1 & 0 \end{pmatrix} \mathcal{M}^N \begin{pmatrix} E_N \\ E_{N+1} \end{pmatrix} \tag{17}$$

where

$$\mathcal{M} = \begin{pmatrix} 2\cos q & -1 \\ 1 & 0 \end{pmatrix} \tag{18}$$

and $2\cos q' = 2\cos k - \epsilon_0'(1 + \lambda|E(0)|^2)k\sin k$, comes from the nonlinear δ-function at x=0. E_{-N} and $E_{-(N+1)}$ are given by the output field

$$E_{-N} = E_t\, e^{-iNk}\ , \qquad E_{-(N+1)} = E_t\, e^{-i(N+1)k}\ . \tag{19}$$

E_N and E_{N+1} are related to the incoming and reflected fields by

$$E_N = E_0\, e^{-iNk} + E_r\, e^{iNk}, \tag{20}$$

$$E_{N+1} = E_0\, e^{-i(N+1)k} + E_r\, e^{i(N+1)k} \tag{21}$$

The intensity at the nonlinear site $|E(0)|^2$ can be expressed in terms of the transmitted intensity $|E_{-N}|^2 = X$ as $|E(0)|^2 = CX$, where

$$C = 1 \mp \epsilon_0\, k \sin k\, \frac{\sin Nq\, \sin(N+1)q}{\sin^2 q}\ . \tag{22}$$

In Eq. (22) q should be replaced by $i|q|$ for $|\cos q| > 1$, and the lower sign in C is used when $\cos q < -1$. After some algebra we arrive at the final result

$$Y = X\left[1 + \tau'\left(1 + \lambda' X\right)^2\right] \ , \tag{23}$$

where $\tau' = \tau\,\alpha^2\,\frac{\sin^2(2N+1)q}{\sin^2 q}$, $\lambda' = \lambda\,\frac{\epsilon_0'}{\epsilon_0}\,\alpha^{-1}\,\frac{C^2 \sin q}{\sin(2N+1)q}$ and $\alpha = (1 + \frac{(\epsilon_0' - \epsilon_0)\,C\,\sin q}{\epsilon_0 \sin(2N+1)q})$. Of course, this result can also be obtained from Eqs. (6) through (8) by specifying the respective expressions for the reflection and transmission amplitudes, r_i and t_i ($i = 1, 2$). Since Eq.(2) and Eq. (23) have the same form, all the analysis done in section II. A applies. However, due to the renormalization of the parameters τ and λ, interesting features arise: τ' is related to the total linear (λ=0) transmission coefficient of the system $\tau' = (1 - |T_{\text{TOTAL}}|^2)/|T_{\text{TOTAL}}|^2$, and the condition $\tau' > 3$ implies $|T_{\text{TOTAL}}|^2 < .25$. Also, the constraint $\lambda < 0$ is now relaxed since it requires only $\lambda' < 0$.

In Fig. 5a we plot the switching up and down intensities for the case $\epsilon_0' = \epsilon_0$ and for frequencies close to the first band gap. We note that the sign of λ required to obtain bistability, between successive lobes of the linear (λ=0) transmission curve, is alternating from $\lambda < 0$ to $\lambda > 0$. We can understand this by means of the field configuration that characterize these lobes for the linear lattice. Every lobe corresponds to a transmission resonance for which the intensity envelope is $|E(x)|^2 \propto \sin^2(mx/L)$ where L is the length of the structure, $0 \leq x \leq L$, and $m = 1, 2, 3, \ldots 2N + 1$ starting from the upper band edge and moving to lower frequencies [19]. When m is odd, the intensity at the middle of the structure will have a maximum, while when m is even, it will have a minimum. If we now turn on the nonlinearity ($\lambda \neq 0$) in the δ-function in the middle of the structure, it will introduce an appreciable phase shift only when the incident wave is tuned close to an "odd" lobe's frequency. This phase shift will change the intensity envelope, and thus the resonance frequencies, resulting in an effective frequency "shift" for the "odd" lobes. For some intensity, the incident wave's frequency will match to the "shifted" lobe's frequency, and a transmission resonance will be obtained. This is where the bistable behavior originates from. The condition on τ' sets the allowed frequencies for observing bistability in between the transmission lobes. Also, a negative nonlinearity ($\lambda < 0$) will cause the odd lobes to shift to higher frequencies, while a positive nonlinearity ($\lambda > 0$) will cause them to shift to lower frequencies [19]. This is shown in Fig. 6 for both the δ-function and finite width models. Note that lobes closer to the gap shift at lower intensities, indicating that for those frequencies smaller switching thresholds should be expected. With these features, the bistability diagram in Fig. 5a is fully understood.

An important consequence of the introduction of the two linear systems is the presence of resonances. The phase shift introduced by the nonlinear δ-function must be enough to tune the incident wave with the shifted lobe. The same transmission lobes are found in the linear transmission diagram of a finite superlattice. Then, from the point of view of induced phase shifts, there should be no real qualitative difference between the δ-function model and the finite layer superlattice, at least for the first bistable loop. The finite layer system differs qualitatively from the nonlinear δ-function model insofar as it always exhibits multistability (the nonlinear δ-function system is strictly bistable), a point which will be discussed in section III. But when considering the first bistable loop only, the very thin layer approximation may be viewed as a reliable guide to more realistic systems involving finite width nonlinear layers. This is shown in Fig. 5b where we plot the switching up and down intensities of the first bistable loop, for a finite width layered model with a finite width nonlinear impurity layer, having it's system parameters defined in correspondence with the δ- function model by $\epsilon_0 = dn^2$. In order to stress the similarity, we have chosen the nonlinear layer to equal to half a lattice period. We see that the δ-function model indeed captures most of the essential features of the more realistic finite width superlattice.

Similar behavior is obtained for the $\epsilon_0' \neq \epsilon_0$ impurity case for frequencies inside the transmission band. In Fig. 7 we show the switching intensities of both the δ-function layer and finite width layer systems for a weak impurity $\epsilon_0' < \epsilon_0$. For these values, the linear (λ=0) impurity mode, which is actually the $m = 1$ transmission lobe being shifted inside the band gap [19], is very close to the transmission band. For $\epsilon_0' > \epsilon_0$, no gap impurity mode exists in the δ-function model so the response of the two systems inside the gap is different. For $\epsilon_0' < \epsilon_0$, both systems exhibit an impurity mode inside every band gap [14]. When the fields are turned on, a positive nonlinearity in the middle of the structure will shift the impurity mode to lower frequencies, while a negative nonlinearity will shift it to higher frequencies. As a consequence, when $\lambda > 0$ bistability is observed at frequencies lower than that of the linear impurity mode, while for $\lambda < 0$ we must use higher frequencies.

The switching up and down intensities are generally $Y_{-} \sim 1/|\lambda'|$ and $Y_{+} \sim \tau'/|\lambda'|$, and for band gap frequencies it is generally $\tau' \gg \lambda' \gg 1$, yielding extremely low switching down intensities and very high switching up intensities. Nevertheless, for frequencies relatively close to the linear defect frequency, it is $\lambda' \gg \tau' \gg 1$, yielding extremely small switching up intensities as well. As can be seen in Fig. 8, where we plot the switching intensities for a large impurity (linear impurity mode deep inside the band gap), the order of magnitude for a $N = 20$ system is well below 10^{-20}, and becomes exponentially small as N gets larger. To get a feeling for this number, assume that typical electronic nonlinearities are of the order of $|\lambda| \sim 10^{-15}\text{cm}^2/\text{W}$. Then $Y_{\pm} \sim 10^{-5}\text{W}/\text{cm}^2$. Furthermore, the intensity at the nonlinear defect layer is small enough, to secure that the nonlinearity is well described as a Kerr nonlinearity: The nonlinear effect does not saturate and the nonlinear layer will not get damaged from intense fields. However, the price one has to pay to achieve low power thresholds, is to maintain extreme accuracy in the incident frequency, due to the extremely high Q of the mode. For the system described in Fig. 8 this accuracy is of the order of $\Delta k/k \sim 10^{-10}$. This is quite unrealistic. In addition, this ratio gets exponentially small for increasing N. Thus, for a realistic application it is the laser's line-width which determines the power thresholds for bistability and in general compromise has to be found.

Dielectric superlattice with nonlinear impurity: resonance states

In the previous section, we have investigated the response of a very thin layer of nonlinear material sandwiched between two linear Bragg reflector structures. We demonstrated that such a structure can exhibit bistability with very low switching threshold as a result of coupling to the impurity mode in the stop gap of the linear structure. In this section, we consider the situation when the nonlinear layer is not thin. There are qualitative differences between the response of a nonlinear finite width layer and a nonlinear δ-function layer. We have seen that a single finite width dielectric layer exhibits bistability for both positive and negative Kerr-coefficients (Fig. 2a), whereas the single nonlinear δ-function exhibits bistability for negative Kerr-coefficient only. Similarly and in contrast to the strictly bistable δ-function model, dielectric superlattices with a nonlinear impurity always exhibit multistability. This, we will show, has to do with the fact that impurity modes exist for each value of $\Delta\epsilon$. We can understand all these properties qualitatively if we view the finite nonlinear layer as consisting of a sequence of of nonlinear δ-functions. Then, resonance phenomena allow to bypass the limited behavior of a single nonlinear δ-function. However, multistability is much harder to detect than bistability, because the field values at the nonlinear layer may be very large and oscillating, thus requiring extremely high precision.

Let us first investigate the localized mode solution for a finite width nonlinear layer sandwiched between two Bragg-reflectors. The nonlinear wave equation inside the impurity layer is given by

$$\frac{d}{d\,x^2}E(x) + k_0^2\left(1 + \lambda|E(x)|^2\right)E(x) = 0 \quad , \tag{24}$$

where $k_0 = n^2(\omega/c)$. This equation may be solved by means of the following ansatz [3]:

$$E(x) = E_0\, g(x)\, e^{i\phi(x)} \tag{25}$$

Inserting this ansatz into Eq. (24) leads to a separation of the amplitude and phase function, $g(x)$ and $\phi(x)$, respectively:

$$\frac{d}{d\,x}\phi(x) = \frac{W}{g^2(x)} \tag{26}$$

$$\left(\frac{d\,g(x)}{d\,x}\right)^2 + \frac{W}{g^2(x)} + k_0^2\, g^2(x) + \frac{1}{2}\,\tilde{\lambda}\, k_0^2\, g^4(x) = A \tag{27}$$

where $\tilde{\lambda} = \lambda\,|E_0|^2$ is the effective nonlinearity and A and W are constants to be determined. Upon introducing $I(x) = g^2(x)$, the solution may be cast in the deceptively simple form:

$$\int_{I(x_0)}^{I(x)} \frac{dI}{\left(AI - k^2I^2 - \frac{1}{2}\tilde{\lambda}k^2I^3 - W^2\right)^{1/2}} = \pm 2(x - x_0) \tag{28}$$

$$\phi(x) = \phi(x_0) + W\int_{x_0}^{x} dx'\,\frac{1}{I(x')} \tag{29}$$

The four unknowns A, W, $\phi(x_0)$, $I(x_0) \equiv g^2(x_0)$ have to be determined from the boundary conditions at x_0. In particular, W is related to the energy flux through the layer as can be seen by evaluating the Poynting "vector" $S = -c^2/8\pi\omega\,\mathrm{Re}\,[i\,E^*(x)(d\,E(x)/dx)] = c^2|E_0|^2W/8\pi c$. In the case of $\lambda = 0$ it is an easy exercise to obtain the linear solutions from Eq. (28). For $\lambda \neq 0$, despite the apparent simplicity of Eq. (28), a closed form solution cannot be obtained in general. The reason for this difficulty is seen as follows: The solution of Eq. (28) comes down to finding the roots of the denominator, where A and W depend on the boundary values in a complicated way. This task can be accomplished in two special circumstances only: If $d\phi(x_0)/dx = 0$, then, according to Eq. (27) we already have one root, leaving us with the simple exercise of solving a quadratic equation. Similarly, if $W = 0$ we immediately have the root $I = 0$, again reducing the problem to a quadratic equation. The first case was exploited by Chen and Mills [3] in solving the transmission problem through a single finite width nonlinear layer only, without the superlattices on both sides.

We, however, are interested in the second situation. Apparently, $W = 0$ implies $S = 0$. This corresponds to a spatially symmetric situation, i.e., a situation where parity is a good "quantum" number. Speaking in terms of the transmission experiment we have in mind, this amounts for solving for the stationary or resonance states for which input equals output. This distinction is of no importance in the linear problem, because there we can construct any state by an appropriate superposition of stationary states. Obviously, this cannot be done in a nonlinear problem. Consider now the case where the nonlinear layer, centered at $x = 0$, is sandwiched between two infinitely extended linear superlattices of alternating layers of dielectric constants ϵ_a and ϵ_b and widths $a - d$ and d, respectively (cf. Fig. 9): Since the stationary states have parity $p = \pm 1$ we may impose the following values of the electrical field $E(0)$ and its derivative $E'(0)$, i.e. the magnetic field, at the origin:

Even Solution ($p = 1$):

$$E(0) = E_0 \neq 0 \quad \Rightarrow \quad \phi(0) = 0, \quad g(0) = 1$$

$$E'(0) = 0 \quad \Rightarrow \quad g'(0) = 0$$

Odd Solution ($p = -1$):

$$\begin{aligned} E(0) = 0 \quad &\Rightarrow \quad \phi(0) = 0, \;\; g(0) = 0 \\ E'(0) = E_0\, k_0 \sqrt{1 + \tilde{\lambda}/2} \neq 0 \quad &\Rightarrow \quad g'(0) = k_0 \sqrt{1 + \tilde{\lambda}/2} \end{aligned}$$

Here, we have chosen the non-zero value of the field's derivative for the odd solution in a particular convenient form (compare with the later calculations for the constant A).

To compare with numerical studies, the above equations define the value of E_0 and, thus, the effective nonlinearity $\tilde{\lambda}$. Consequently, for a given frequency we need to search for the symmetric states (resonant states) in the transmission problem and compute the field E_0 at the origin. For given λ we then get the effective nonlinearity $\tilde{\lambda} = \lambda\,|E_0|^2$.

The computation of the parameter A in (27) is now straightforward and due to the "tricky" definitions is the same for both parities:

$$A = k_0^2 \left(1 + \frac{1}{2}\tilde{\lambda}\right) \tag{30}$$

In addition, we can compute the missing roots of the cubic expression in (28):

$$\begin{aligned} I_1 &= 0 \\ I_2 &= -\frac{2+\tilde{\lambda}}{\tilde{\lambda}} \\ I_3 &= 1 \end{aligned}$$

In order to finally solve Eq.(28), we have to distinguish four cases: The solution to depends on parity and the sign of one root , namely I_2 depends on the sign of $\tilde{\lambda}$ (cf. [16]).

We begin with $\tilde{\lambda} > 0$:

Define the quantities

$$\kappa = \sqrt{\frac{\tilde{\lambda}}{2 + 2\tilde{\lambda}}} \tag{31}$$

$$\alpha = \begin{cases} K(\kappa) & p = 1 \\ 0 & p = -1 \end{cases} , \tag{32}$$

where K denotes the Complete Elliptic Integral of the first kind. Then, the solution to Eq. (28) reads as:

$$I(x) = \frac{\mathrm{sn}^2\left(\pm k_0 x\sqrt{1+\tilde{\lambda}} + \alpha; \kappa\right)}{1 + \frac{\tilde{\lambda}}{2+\tilde{\lambda}}\mathrm{cn}^2\left(\pm k_0 x\sqrt{1+\tilde{\lambda}} + \alpha; \kappa\right)}$$

Here, sn and cn are the Jacobian Elliptic Functions. These results may be simplified by the use of the addition theorems of the Jacobian Elliptic Functions.

$p = 1$:

$$I(x) = \mathrm{cn}^2\left(k_0 x\sqrt{1+\tilde{\lambda}}; \kappa\right) \tag{33}$$

$p = -1$:

$$I(x) = \left(\frac{1+\frac{1}{2}\tilde{\lambda}}{1+\tilde{\lambda}}\right)\frac{\mathrm{sn}^2\left(k_0 x\sqrt{1+\tilde{\lambda}}; \kappa\right)}{\mathrm{dn}^2\left(k_0 x\sqrt{1+\tilde{\lambda}}; \kappa\right)}\ , \tag{34}$$

where $\mathrm{dn} = \sqrt{1-\kappa^2\mathrm{sn}^2}$. Similar solutions emerge in the case of a negative Kerr-coefficient, $\tilde{\lambda} < 0$:

Define the quantities

$$\eta = |\tilde{\lambda}| \tag{35}$$

$$\kappa = \sqrt{\frac{\eta}{2-\eta}} \tag{36}$$

$$\beta = \begin{cases} K(\kappa) & p = 1 \\ 0 & p = -1 \end{cases} \tag{37}$$

Then the solution to (28) reads as:

$$I(x) = \mathrm{sn}^2\left(\pm k_0 x\sqrt{1 - \frac{1}{2}\eta} + \beta; \kappa\right)$$

These results may, again, be simplified by the use of the addition theorems of the Jacobian Elliptic Functions:

$p = 1$:

$$I(x) = \frac{\mathrm{cn}^2\left(k_0 x\sqrt{1-\frac{1}{2}\eta}; \kappa\right)}{\mathrm{dn}^2\left(k_0 x\sqrt{1-\frac{1}{2}\eta}; \kappa\right)} \tag{38}$$

$p = -1$:

$$I(x) = \mathrm{sn}^2\left(k_0 x\sqrt{1-\frac{1}{2}\eta}; \kappa\right)\ . \tag{39}$$

Outside the nonlinear layer the waves obeys the Bloch-Floquet theorem. We employ the "traveling wave" description [17], which decomposes the field $E(x)$ and (implicitly) its derivative $E'(x)$ into left and right moving waves:

$$\vec{E}(x) = \begin{pmatrix} A_r\, e^{ikx} \\ A_l\, e^{-ikx} \end{pmatrix} \tag{40}$$

Within this formalism, the Bloch-Floquet condition for a defect state inside the photonic band gap, created by the linear superlattice, may be written as (connecting the fields in the middle of one linear A-layer at $x = s$ to the fields at $x = a + s$, where a is a lattice constant):

$$(\mathcal{M} \pm e^{-\gamma_a}\mathcal{E})\ \vec{E}(s) = 0 \tag{41}$$

where the matrix elements of $\mathcal{M}$ are well-known:

$$\mathcal{M}_{11} = e^{ik_a(a-d)}\left(\cos(k_b d) + \frac{i}{2}\left(\frac{k_b}{k_a} + \frac{k_a}{k_b}\right)\sin(k_b d)\right)$$

$$\mathcal{M}_{12} = \frac{i}{2}\left(\frac{k_b}{k_a} - \frac{k_a}{k_b}\right)\sin(k_b d)\ .$$

were $k_a = \frac{\omega}{c}\sqrt{\epsilon_a}$, $k_b = \frac{\omega}{c}\sqrt{\epsilon_b}$ and $\mathcal{M}_{11} = \mathcal{M}_{22}^*$, $\mathcal{M}_{12} = \mathcal{M}_{21}^*$. Inside the nonlinear layer we know the field and its derivative at the origin. Using the solutions Eqs. (33) through (39), we can now calculate the field and its derivative at the interface to the A-material, translate the results into the traveling wave formalism (field and derivative are continuous at the boundary!) and propagate them to the middle of the A-layer, i.e. we obtain $\vec{E}(s)$:

$$(\vec{E})_1(s) = e^{ik_a s}\sqrt{I(l/2)} - \frac{i}{k_a}e^{ik_a s}\frac{d}{dx}\sqrt{I(l/2)} \tag{42}$$

$$(\vec{E})_2(s) = \left((\vec{E})_1(s)\right)^*\ , \tag{43}$$

where $s = (a - l)/2$ and l is the thickness of the nonlinear layer. Thus, (41) constitutes two linear equations, the second being the complex conjugate of the first. Upon separating this complex equation into real and imaginary part, we observe that the real part does not contain γ and may thus be used to determine ω:

$$\begin{aligned} &\sin(k_a(a-d))\cos(k_b d) + \\ &+\frac{1}{2}\left(\frac{k_b}{k_a} + \frac{k_a}{k_b}\right)\cos(k_a(a-d))\sin(k_b d) + \\ &+\frac{1}{2}\left(\frac{k_b}{k_a} - \frac{k_a}{k_b}\right)\sin(k_b d)\psi(\omega) = 0 \end{aligned} \tag{44}$$

Here, $\psi(\omega)$ contains the information about the nonlinear layer. If we define

$$\begin{aligned}
\chi^{(0)}(x) &= \frac{\sqrt{I(x)}}{k_a}\,\frac{d\left(\sqrt{I(x)}\right)}{dx} \\
\chi^{(+/-)}(x) &= I(x) \pm \frac{1}{k_a^2}\left(\frac{d\left(\sqrt{I(x)}\right)}{dx}\right)^2
\end{aligned}$$

Then $\psi(\omega)$ is given as:

$$\psi(\omega) = \frac{\cos(k_a s)\,\chi^{(-)}(l/2) + 2\sin(k_a s)\,\chi^{(0)}(l/2)}{\chi^{(+)}(l/2)} \tag{45}$$

where $s = a - d + l$ (a = lattice constant; d = thickness of the B layers; l = thickness of the nonlinear layer). $\sqrt{I(l/2)}$ and $d\left(\sqrt{I(l/2)}\right)/dx$ have to be evaluated according to the sign of $\tilde{\lambda}$ and parity.

Eq. (44) defines the solution for the impurity modes for our structure. These impurity modes manifest themselves as resonances in the nonlinear multistable response, for frequencies inside the gap of the linear superlattice. In the δ-function model we had only one such resonance, as required from it's strictly bistable character. As discussed above, for a nonlinear impurity of finite width in an infinitely extended linear superlattice we now expect multistable behavior. For practical applications, the linear superlattices cannot be infinitely extended. However, as long as the number of the layers is large enough to have a well defined localized solution, the resonant frequencies should be given exactly by Eq. (44).

Fig. 10 shows the resonance state frequencies as a function of $\tilde{\lambda}$ for a linear superlattice consisting of equally wide layers of alternating dielectric constant $\epsilon_a = 1$ and $\epsilon_b = 5$. The nonlinear layer is described by $n^2 = 8$, $l = d$ and $\lambda = 1$. Solid lines represent the analytical solution according to Eq. (44), while the circles correspond to the results of a numerical simulation using 20 bilayers on each side of the nonlinear layer. In addition, the parity of the resonance states is indicated. Evidently, the agreement between the two methods is excellent, thus illustrating the multistable behavior. This feature (multistability) is explicitly shown in Fig. 11, where we show the input-output diagram for the same configuration. Finally, in Fig. 12 we show the intensity configuration for two resonance states with different parities.

Each resonance state is characterized by the intensity configuration inside the nonlinear layer. The first has one lobe, the second two, the third three e.t.c. In the δ-function case, the possibility of different intensity configurations inside the nonlinear medium is absent. Thus, only one resonance state would be allowed, which is the analogue of the first resonance state of the finite width case shown in Fig. 12a.

Conclusions

We have investigated the general problem of electromagnetic wave propagation through a one dimensional system consisting of a nonlinear layer sandwiched between any two linear systems. Our studies provide a general frame within which calculations can be done, based on the transmission characteristics of the linear systems. In the case of a very thin layer, we have shown that a δ-function approximation is adequate. It follows from our analysis that a nonlinear layer sandwiched between two identical Bragg-reflectors can be regarded as the most efficient "localized" feedback structure. For this system, a cubic equation has been derived, describing the nonlinear bistable response, with normalized parameters that characterize the experimental situation. We obtain bistability in the gap of the linear system, via the impurity mode, and find that the switching thresholds can be made very small by enlarging the structure and/or widening the gap. In addition, we have obtained an analytic solution for the localized resonance modes in the band gap for a nonlinear impurity of finite extent in an otherwise linear dielectric superlattice. The solution shows multistable behavior, the basic feature absent in the δ- function model. Our numerical studies agree extremely well with these solutions.

Acknowledgments

Ames Laboratory is operated for the U.S. Department of Energy by Iowa State University under Contract No. W-7405-Eng-82. This work was supported by the Director for Energy Research office of Basic Energy Sciences and Advanced Energy Projects and by NATO Grant No. 940647. K. Busch acknowledges financial support from the German-Israeli Foundation (GIF).

Bibliography

[1] H. G. Winfull, J. H. Marburger, and E. Garmire, Appl. Phys. Lett. **35**, 379 (1979).

[2] W. Chen and D. L. Mills, Phys. Rev. B **35**, 524 (1987).

[3] H. M. Gibbs, S. L. McCall, and T. N. C. Venkatesan, Phys. Rev. Lett. **36**, 1135 (1976).

[4] B. Xu and N. B. Ming, Phys. Rev. Lett. **71**, 3959 (1993).

[5] C. J. Herbert, W. S. Capinski, and M. S. Malcuit, Opt. Lett. **17**, 1037 (1992).

[6] W. Chen and D. L. Mills, Phys. Rev. B **36**, 6269 (1987).

[7] F. S. Felber and J. H. Marburger, Appl. Phys. Lett. **28**, 731 (1976).

[8] M. Okuda and K. Onaka, Jpn. J. Appl. Phys. **16**, 769 (1977).

[9] F. Deylon, Y. Levy, and B. Souillard, Phys. Rev. Lett. **57**, 2010 (1986).

[10] Yi Wan and C. M. Soukoulis, Phys. Rev. B **41**, 800 (1990).

[11] D. Henning, H. Gabriel, G. P. Tsironis, and M. Molina, Appl. Phys. Lett. **64**, 2934 (1994).

[12] M. I. Molina and G. P. Tsironis, Int. J. Mod. Phys. B **9**, 1899 (1995).

[13] For a recent review, see C. M. Soukoulis, ed., "Photonic Band Gap Materials," (Kluwer, Dordrecht, 1996).

[14] D. R. Smith *et al.*, J. Opt. Soc. Am. B **10**, 314 (1993).

[15] W. Chen and D. L. Mills, Phys. Rev. Lett. **58**, 160 (1987).

[16] C. Martine De Sterke and J. Sipe, in *Progress in Optics*, Vol. 33, edited by E. Wolf, (Elsevier, Amsterdam, 1994).

[17] Qiming Li, C. T. Chan, K. M. Ho, and C. M. Soukoulis, Phys. Rev. B **53**, 15577 (1996).

[18] E. Lidorikis, Qiming Li, and C. M. Soukoulis, Phys. Rev. B **54**, 10249 (1996).

[19] R. P. Stanley, R. Houdre, U. Oesterle, M. Ilegems and C. Weisbuch, Phys. Rev. A **48**, 2246 (1993).

[20] P. F. Byrd and M. D. Friedman: “Handbook of Elliptic Integrals for Engineers and Scientists”, Springer 1971

[21] K. Busch, C. T. Chan and C. M. Soukoulis, NATO ASI, Series E **315**, 465 (1996)

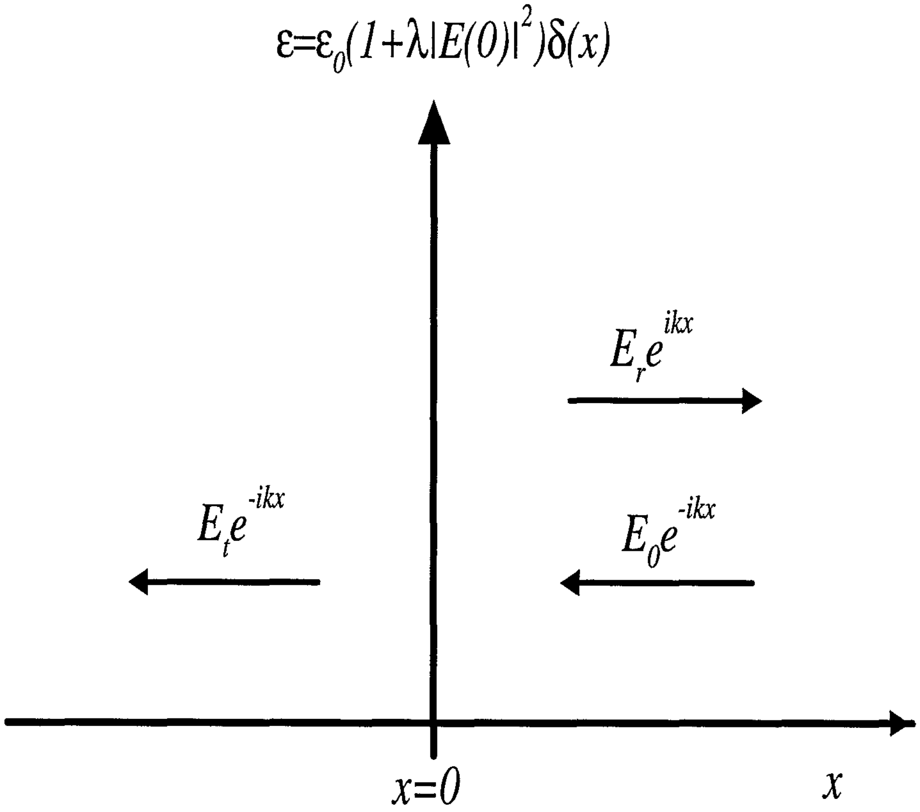

Figure 1 Geometry considered in this section. A plane wave of amplitude E_0 strikes a nonlinear δ-function, giving rise to a reflected and a transmitted wave.

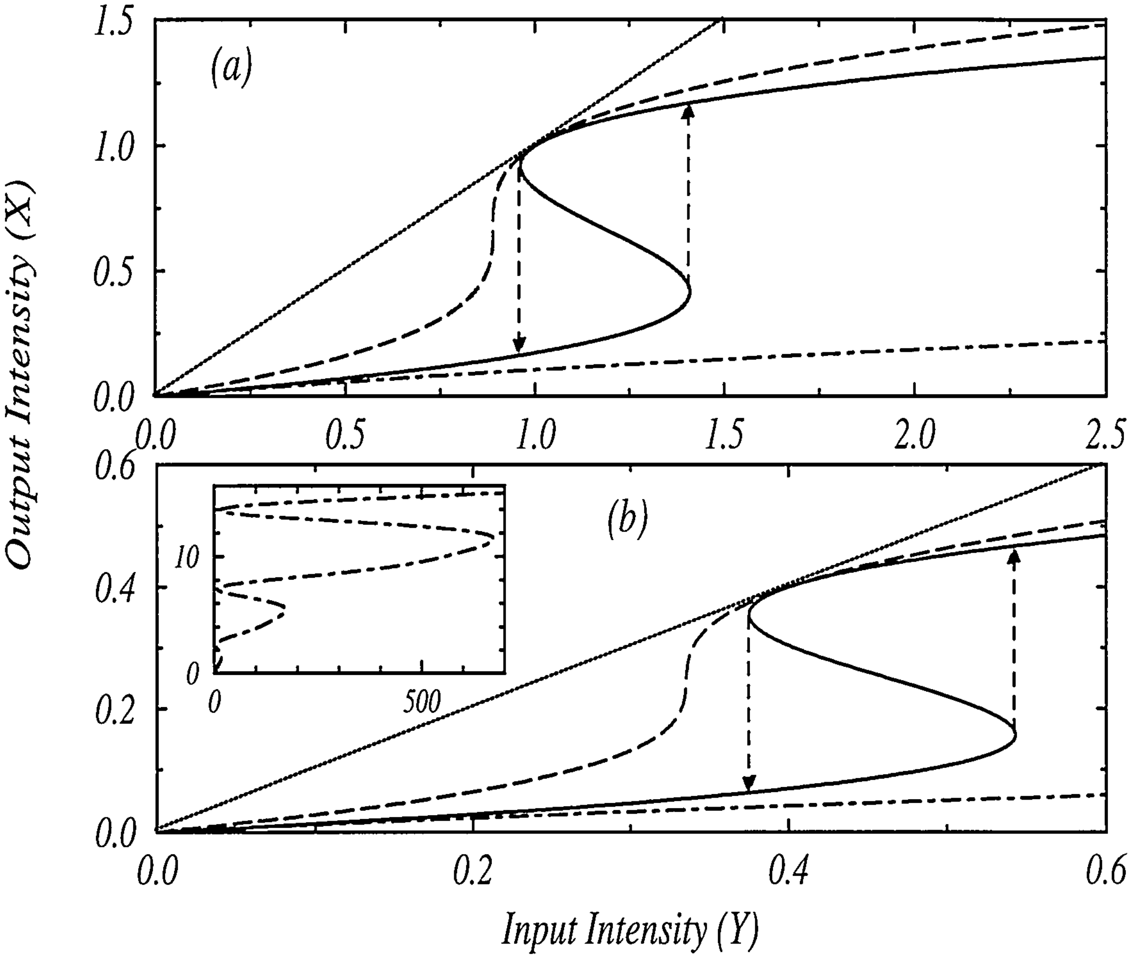

Figure 2 Transmitted intensity versus incident intensity for a) a nonlinear δ-function and b) a nonlinear dielectric slab of width $d = 0.6\lambda_f$. In both cases, the dashed line corresponds to $\lambda = -1$ and linear transmission $|T_0|^2 = 0.25$, the solid line to $\lambda = -1$ and linear transmission $|T_0|^2 = 0.125$, and the dot-dashed line to $\lambda = +1$ and linear transmission $|T_0|^2 = 0.125$. Note that the bistability onset happens for the same system parameters. However, for large intensities the finite layer system with $\lambda > 0$ will always display multistable behavior (inset graph in (b), for the same parameters: $\lambda = +1$, $|T_0|^2 = 0.125$). The dotted line is the total transmission relation $Y = X$.

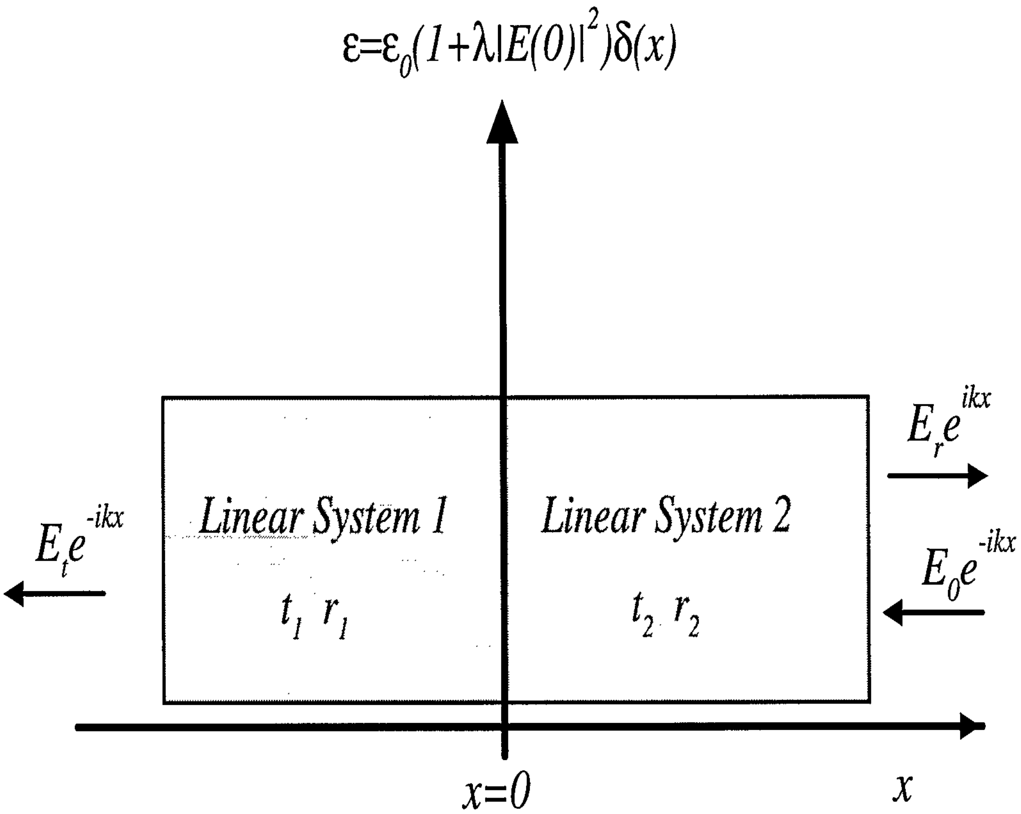

Figure 3 The general geometry considered in this section. A nonlinear δ-function is sandwiched between two general linear systems characterized by the reflection and transmission amplitudes r_i and t_i, $i = 1, 2$. A plane wave of amplitude E_0 incident upon the system from the right, results in a transmission amplitude E_t and a reflection amplitude E_r .

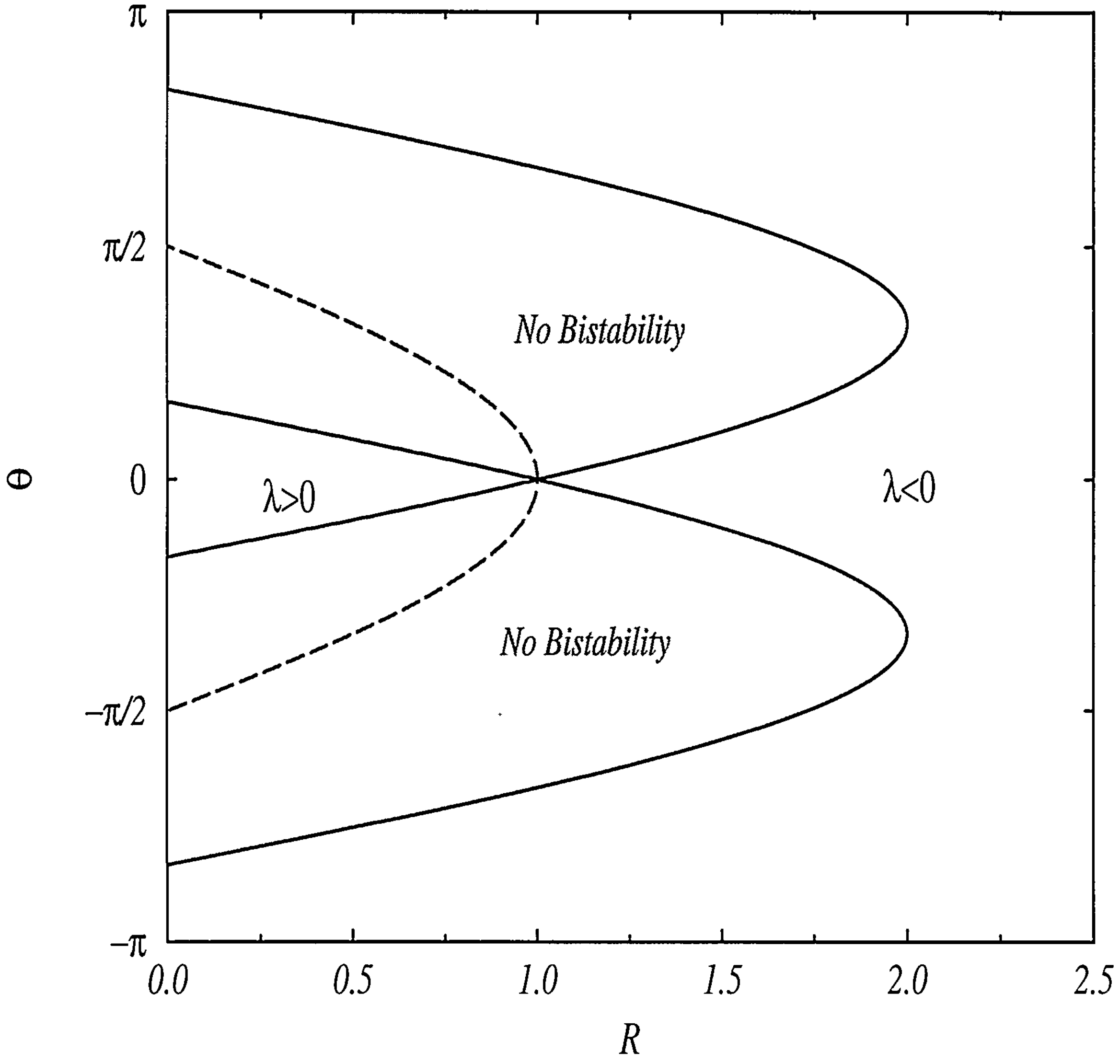

Figure 4 The phase diagram for the onset of bistability for a δ-function sandwiched between two linear systems, as derived from Eqs. (13) and (14). θ and R are defined through $1/T_0 = Re^{i\theta}/T$ where T_0 is the total linear transmission amplitude of the two linear structures with the δ-function in the middle ($\lambda \equiv 0$) and T is the total transmission amplitude without the δ-function ($\epsilon_0 \equiv 0$). Eq. (13) sets the values of R and θ for which we can observe bistability, outside the gray areas, while Eq. (14) (dashed line) sets the sign of the nonlinear coefficient λ for which we will observe bistability.

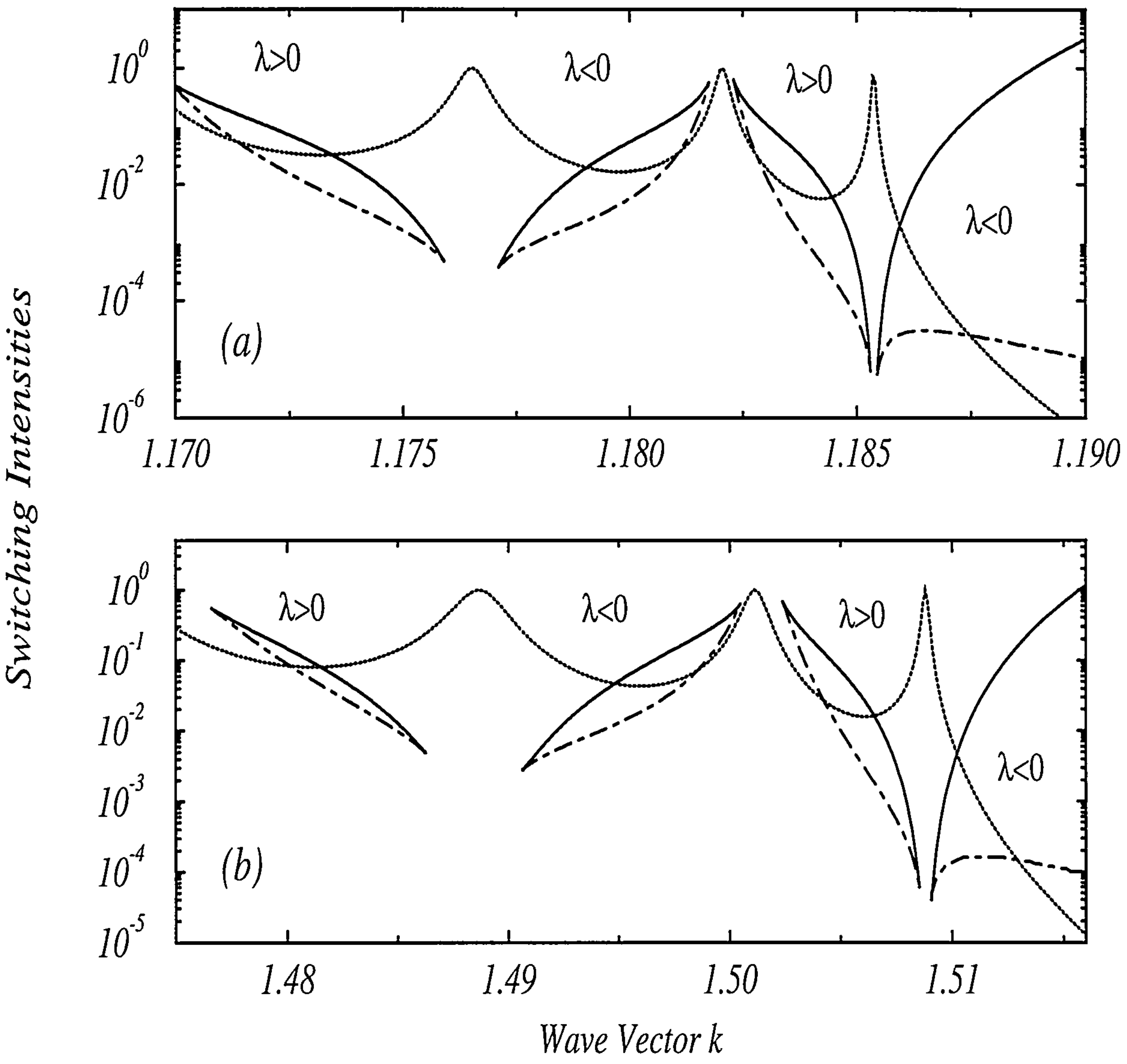

Figure 5 Switching up (solid line) and switching down (dot-dashed line) intensities for a nonlinear impurity system sandwiched between two linear structures. The linear structures consist of a) δ-functions with N=20, $\epsilon_0' = \epsilon_0 = 2.5$ and spacing $a = 1$, and as a comparison, b) a system of 41 dielectric bilayers with $d_a = d_b = 0.5$ and $n_a^2 = 1, n_b^2 = 5$ in analogy with the δ-function system: $d_b n_b^2 = \epsilon_0$. The b layer in the middle of the structure is nonlinear with $\epsilon_b(x) = n_b^2(1 + \lambda|E(x)|^2)$. In both cases we used $\lambda = \pm 1$. The dotted line in both graphs is the linear transmission coefficient of the structure. The band gap starts around k=1.186 for the δ-function model and k=1.51 for the finite width model, as can be seen from the large transmission drop. The exact value of the band edge can be found by using Eq. (16).

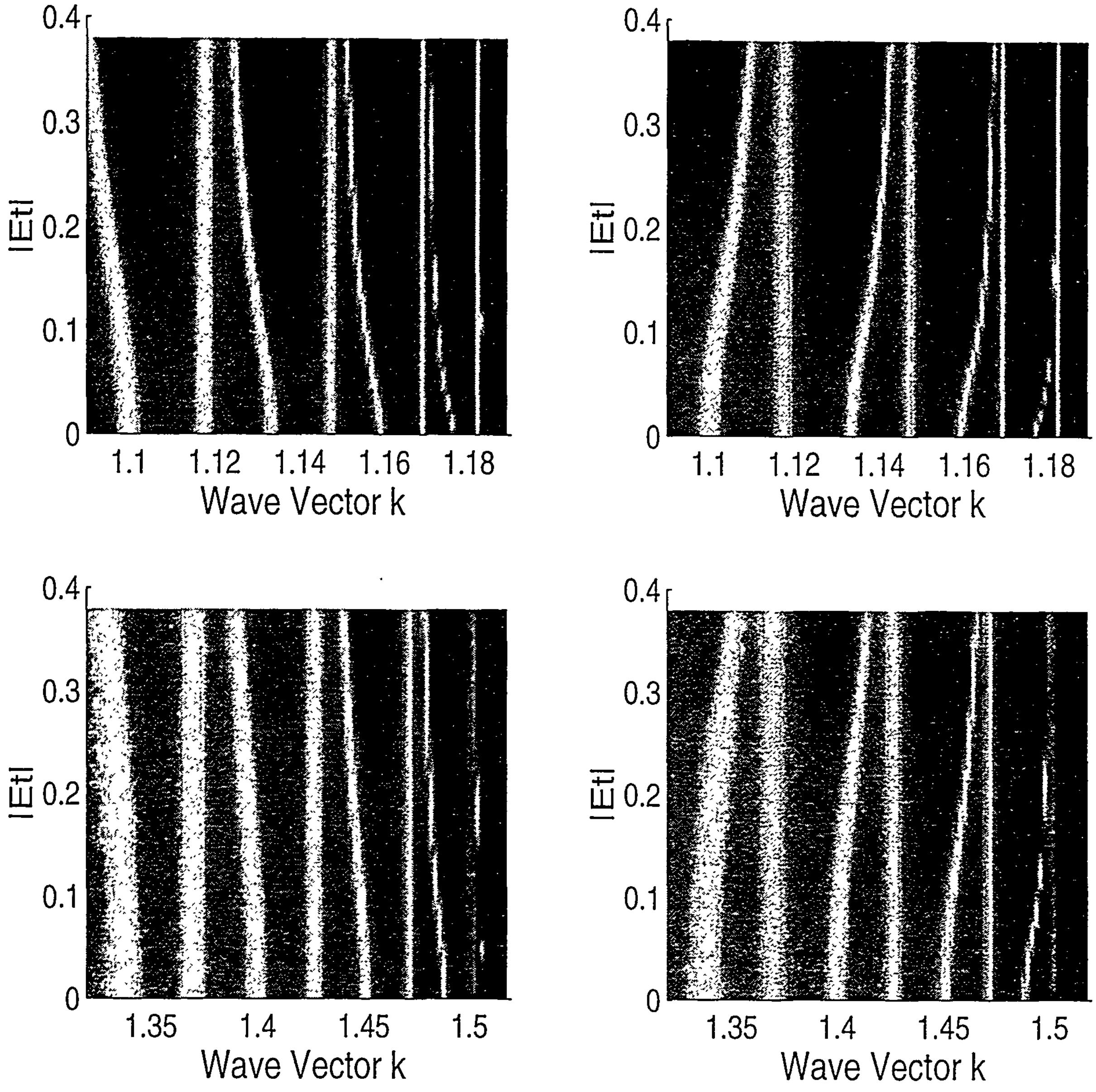

Figure 6 Gray scale plots of the transmission coefficient versus the wave vector k and the transmitted amplitude $|E_t|$ for frequencies inside the transmission band. Dark areas indicate low transmission. The two upper graphs correspond to the δ-function model described in Fig. 5a, for $\lambda = 1$ (left) and $\lambda = -1$ (right). The two lower graphs correspond to the finite width model described in Fig. 5b, for $\lambda = 1$ (left) and $\lambda = -1$ (right). The transmission lobes and their frequency shift are clearly shown, except for the first one right on the band edge, which can barely be distinguished for the $\lambda = 1$ case, while for $\lambda = -1$ it shifts inside the band gap.

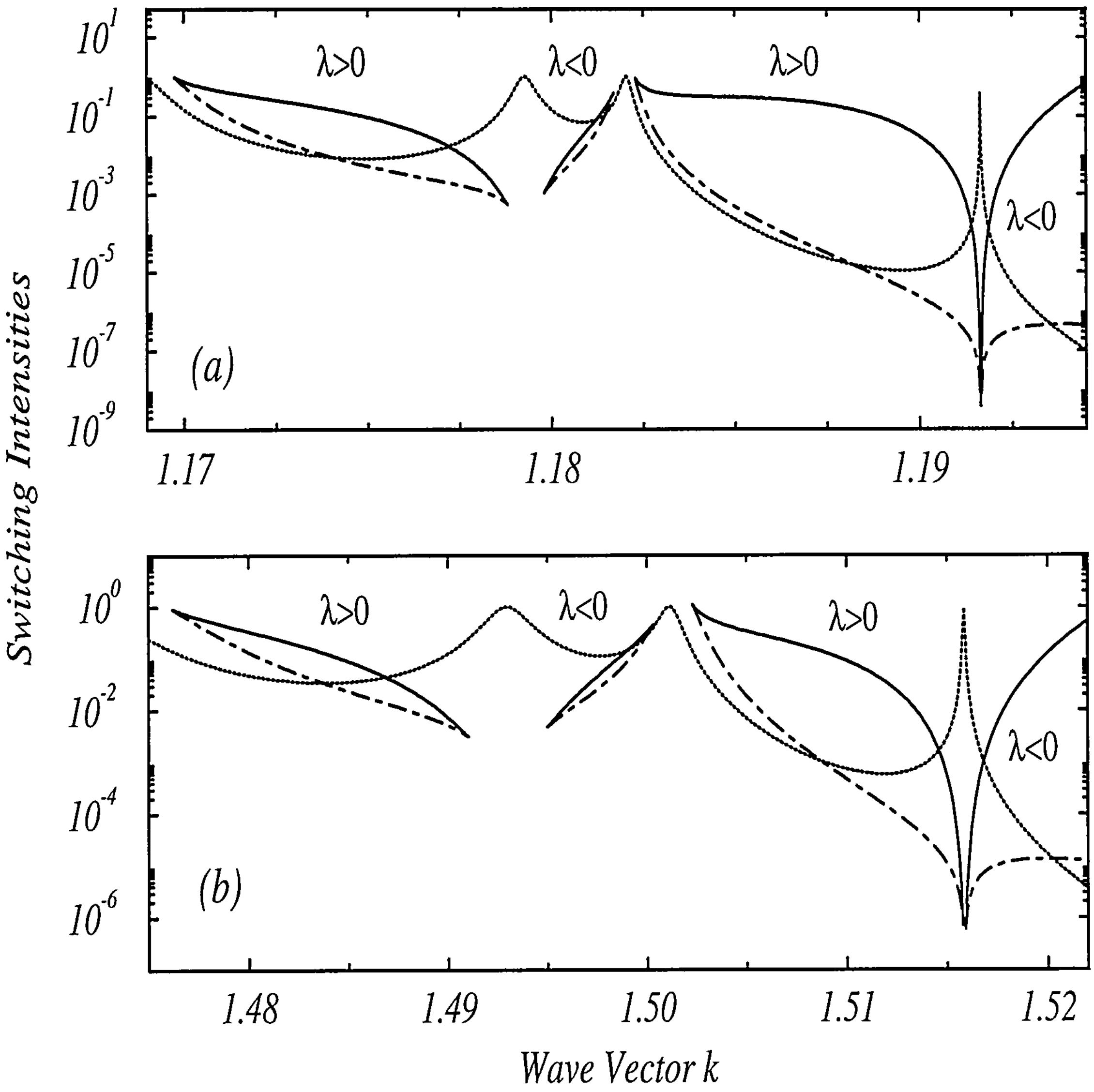

Figure 7 The switching intensities for the same systems as described in Fig. 5, but now the nonlinear impurity is a) a nonlinear δ-function with $\epsilon_0' = 2.2$ and b) a nonlinear layer $\epsilon(x) = n_d^2(1 + \lambda|E(x)|^2)$ with $n_d^2 = 4.4$. We again used $\lambda = \pm 1$. The first lobe, that shifted in the gap and is now the linear (λ=0) impurity mode, is clearly seen in both cases. Note how the switching intensities dropped about three orders of magnitude around this mode.

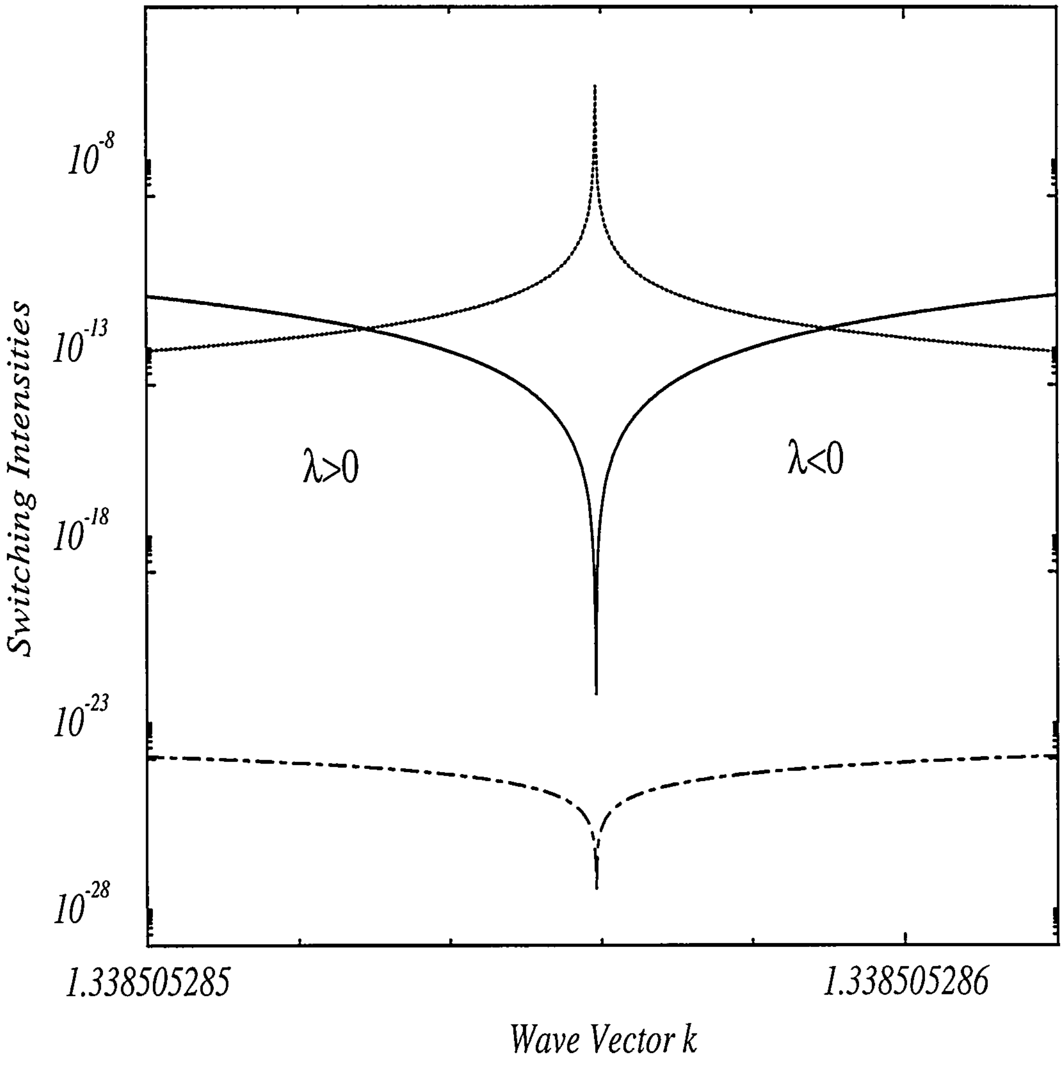

Figure 8 The switching intensities (solid and dot-dashed lines for switching up and down respectively) for the same system of Fig. 5a for the δ model but now for the large impurity case $\epsilon_0' = 1$. The linear impurity mode is now deep in the gap (dotted line corresponds to the linear transmission coefficient). Note that for frequencies very close to this mode the switching intensities become extremely small.

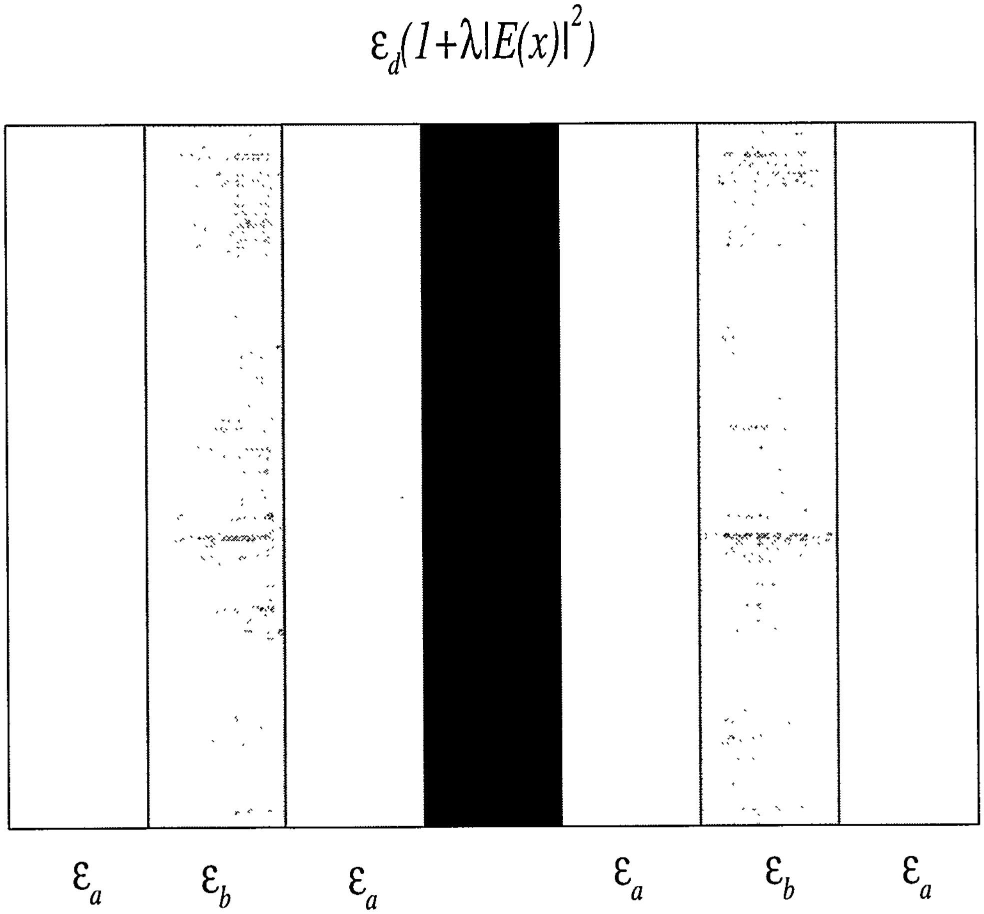

Figure 9 The model superlattice used in this section. A nonlinear layer of dielectric constant $\epsilon_d(1+\lambda|E(x)|^2)$ and thickness ℓ centered at $x=0$ is sandwiched between two infinitely extended superlattices of alternating layers with dielectric constants ϵ_a and ϵ_b, and widths a and $a-d$ respectively.

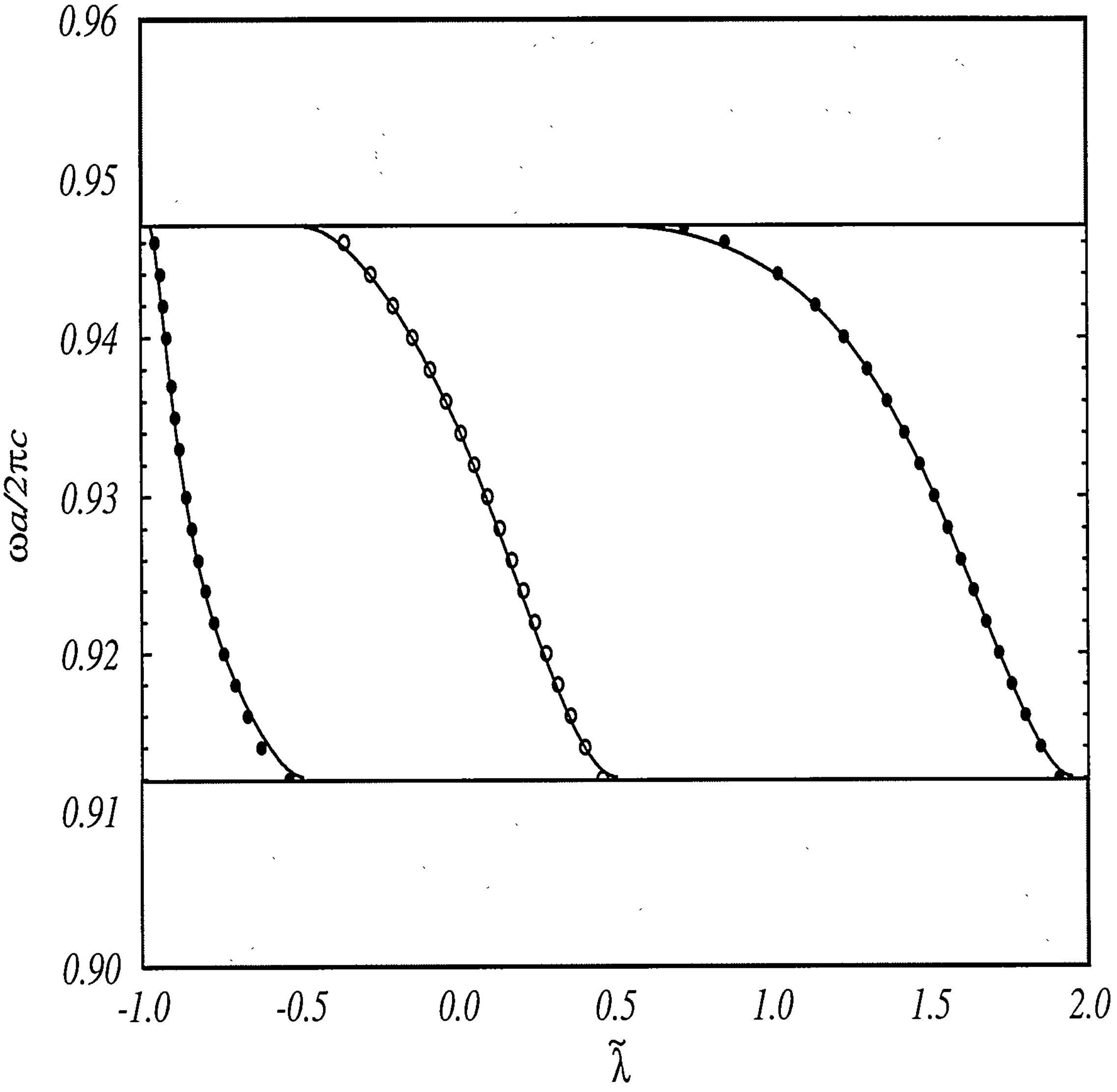

Figure 10 The resonance state frequencies as a function of the effective nonlinearity $\tilde{\lambda}$ inside the third band gap . The linear superlattice consists of equal thickness layers of alternating dielectric constants $\epsilon_a = 1$ and $\epsilon_b = 5$, while the nonlinear layer has $\epsilon_d = 8$, $\ell = d$ and $\lambda = 1$. Solid lines correspond to the analytical results while circles correspond to the results of a numerical simulation using 20 bilayers on each side of the nonlinear layer. Filled circles correspond to states with even parity, while open circles correspond to states with odd parity. The gray areas correspond to parts of the third and fourth transmission bands.

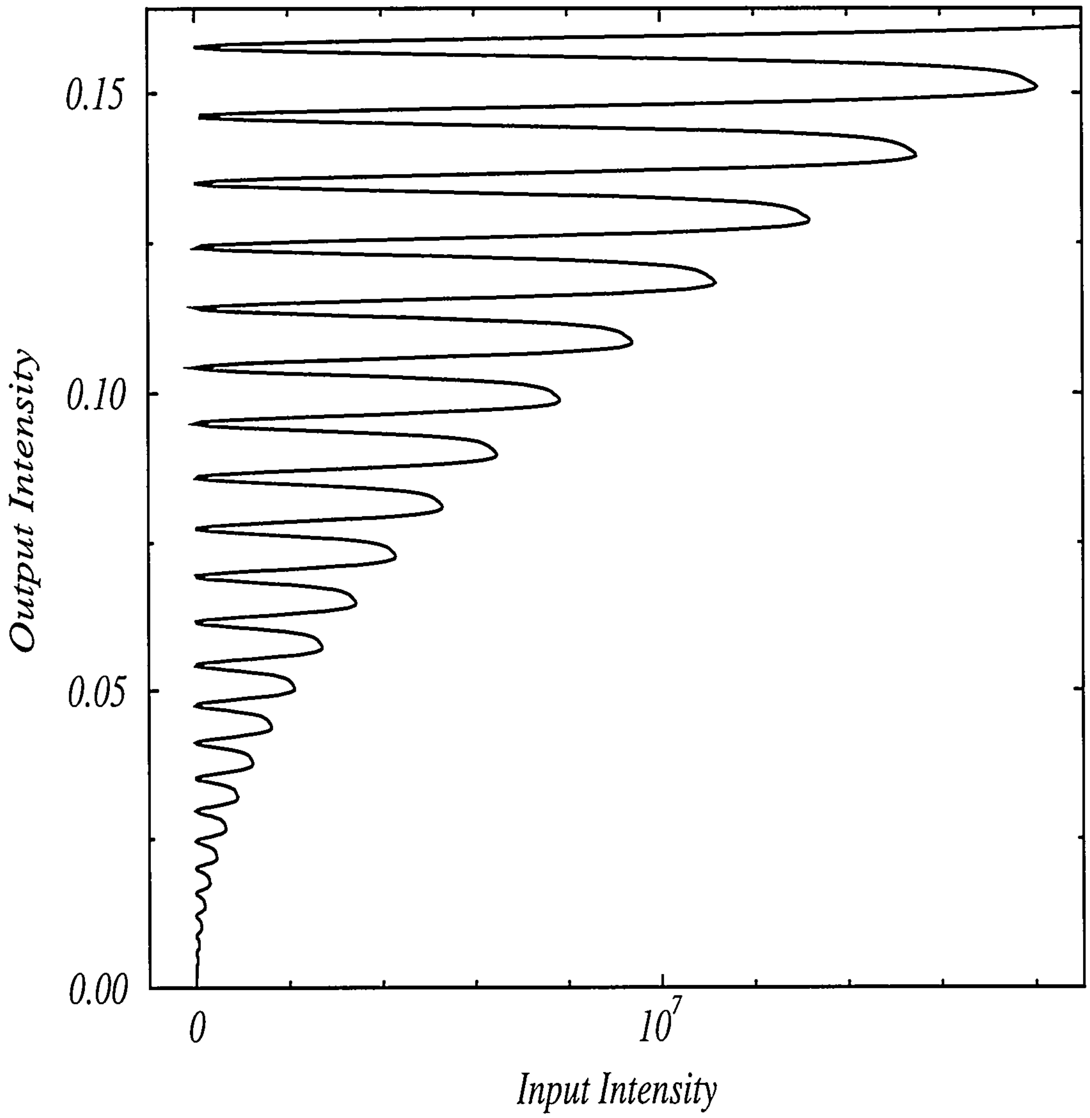

Figure 11 Transmitted intensity versus incident intensity for the same system described in Fig. 10. We used a model of 20 bilayers on each side of the nonlinear layer with $\lambda = 1$ and frequency $\omega a/2\pi c = 0.93$. Every resonance point in this diagram (output=input) will yield a point in the resonance frequency diagram in Fig. 10, with alternating parity. The very first resonance (not distinguishable in this picture) corresponds to an open circle in Fig. 10 for $\omega a/2\pi c = 0.93$ and will have an odd parity.

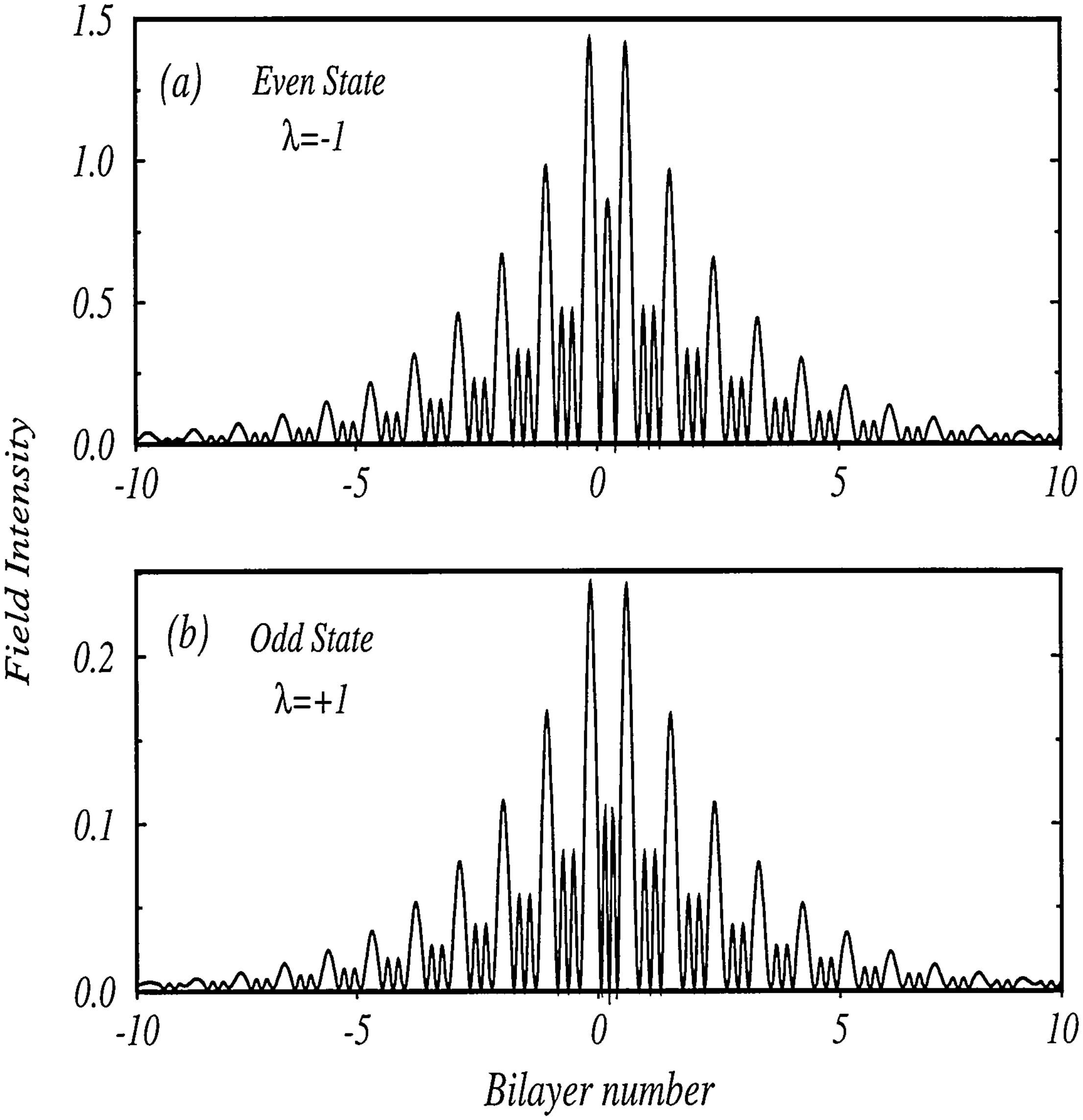

Figure 12 We plot the intensity configuration for the same model described in Fig. 10, for $\omega a/2\pi c = 0.93$. a) Even parity state with $\lambda = -1$, corresponding to the branch on the left (filled circles) in Fig. 10. b) Odd parity state with $\lambda = 1$, corresponding to the branch in the middle of Fig. 10. The later is actually the very first resonance state described in Fig. 11.

CHAPTER 4. PULSE DRIVEN SWITCHING IN ONE-DIMENSIONAL NONLINEAR PHOTONIC BAND GAP MATERIALS: A NUMERICAL STUDY

A paper to be submitted for publication in the journal of Physical Review E

E. Lidorikis and C. M. Soukoulis

Abstract

We examine numerically the time-dependent properties of nonlinear bistable multilayer structures for constant wave illumination. We find that our system exhibits both steady-state and self-pulsing solutions. In the steady state regime, we examine the dynamics of driving the system between different transmission states by injecting pulses, and we find the optimal pulse parameters. We repeat this work for the case of a linear periodic system with a nonlinear impurity layer.

Introduction

Nonlinear dielectric materials [1] exhibiting a bistable response to intense radiation are key elements for an all-optical digital technology. For certain input optical powers there may exist two distinct transmission branches forming a hysteresis loop, which incorporates a history dependence in the system's response. Exciting applications involve optical switches, logic gates, set-reset fast memory elements etc [2]. Much interest has been given lately to periodic nonlinear structures [14], in which because of the distributed feedback mechanism, the nonlinear effect is greatly enhanced. In the low intensity limit, these structures are just Bragg reflectors characterized by high transmission bands separated by photonic band gaps [1]. For high intensities and frequencies inside the transmission band, bistability results from the modulation of transmission by an intensity-dependent phase shift. For frequencies inside the gap bistability originates from gap soliton formation [5], which can lead to much lower switching thresholds [6].

The response of nonlinear periodic structures illuminated by a constant wave (CW) with a frequency inside the photonic gap is generally separated into three regimes: i) steady state response via stationary gap soliton formation, ii) self-pulsing via excitation of solitary waves, and iii) chaotic. Much theoretical work has been done for systems with a weak sinusoidal refractive index modulation and uniform nonlinearity [14, 7, 15, 9, 10], or deep modulation multilayered systems [5, 11, 12], as well as experimental [13, 14]. One case of interest is when the system is illuminated by a CW bias and switching between different transmission states is achieved by means of external pulses. Such switching has already been demonstrated experimentally for various kinds of nonlinearities [13, 15, 16], but to our knowledge, a detailed study of the dynamics, the optimal pulse parameters and the stability under phase variations during injection, has yet to be performed.

In this paper we use the Finite-Difference-Time-Domain (FDTD) [10] method to study the time-dependent properties of CW propagation in multilayer structures with a Kerr type nonlinearity. We find our results generally in accord to those obtained for systems with weak linear index modulation [15], which were solved with approximate methods. We next examine the dynamics of driving the system from one transmission state to the other by injecting a pulse, and try to find the optimal pulse parameters for this switching. We also test how these parameters change for a different initial phase or frequency of the pulse. Finally, we will repeat all work for the case of a linear multilayer structure with a nonlinear impurity layer.

Formulation

Electromagnetic wave propagation in dielectric media is governed by Maxwell's equations

$$\mu\frac{\partial\vec{H}}{\partial t} = -\vec{\nabla}\times\vec{E} \qquad\qquad \frac{\partial\vec{D}}{\partial t} = \vec{\nabla}\times\vec{H} \tag{1}$$

Assuming here a Kerr type saturable nonlinearity and an isotropic medium, the electric flux density $\vec{D}$ is related to the electric field $\vec{E}$ by

$$\vec{D} = \epsilon_0 \vec{E} + \vec{P}_L + \vec{P}_{NL} = \epsilon_0 \left(\epsilon_r + \frac{\alpha |\vec{E}|^2}{1 + \gamma |\vec{E}|^2} \right) \vec{E} \tag{2}$$

where $\gamma \geq 0$. $\vec{P}_L$ and $\vec{P}_{NL}$ are the induced linear and nonlinear electric polarizations respectively. Here we will assume zero linear dispersion and so a frequency independent ϵ_r. Inverting this to obtain $\vec{E}$ from $\vec{D}$ involves the solution of a cubic equation in $|\vec{E}|$. For $\alpha \geq 0$ there is always only one real root, so there is no ambiguity. For $\alpha < 0$ this is true only for $\gamma > 0$. In our study we will use $\alpha = -1$ and $\gamma = (\epsilon_r - 1)^{-1}$ so that for $|\vec{E}| \to \infty$, $\vec{D} \to \epsilon_0 \vec{E}$.

The structure we are considering consists of a periodic array of 21 nonlinear dielectric layers in vacuum, each 20 nm wide with $\epsilon_r = 3.5$, separated by a lattice constant a =200 nm. The linear, or low intensity, transmission coefficient as a function of frequency is shown in Fig. 1a. In the numerical setting each unit cell is divided into 256 grids, half of them defining the highly refractive nonlinear layer. For the midgap frequency, this corresponds to about 316 grids per wavelength in the vacuum area and 1520 grids per effective wavelength in the nonlinear dielectric, where of course the length scale is different in the two regions. Stability considerations only require more than 20 grids per wavelength [10]. Varying the number of the grids used we found our results to be completely converged. On the two sides of the system we apply absorbing boundary conditions. Between the left "absorbing wall" and the beginning of the structure there is an artificial "source" surface separating space into two regions; the "total fields" region on its right and the "reflected fields" region on its left. The incident wave is incorporated as a boundary condition on that surface and it travels to the right, leaving only the reflected fields on the far left side of the system.

We first study the structure's response to an incoming constant plane wave of frequency close to the gap edge $\omega a/2\pi c = 0.407$. For each value of the amplitude, we wait until the system reaches a steady state and then calculate the corresponding transmission and reflection coefficients. If no steady state is achievable, we approximate them by averaging the energy transmitted and reflected over a certain period of time, always checking that energy conservation is satisfied. Then the incident amplitude is increased to its next value, which is done adiabatically over a time period of 20 wave cycles, and measurements are repeated. This procedure continues until a desired maximum value is reached, and then start decreasing the amplitude, repeating backwards the same routine. The form of the incident CW defined only on the "source" surface is

$$E_{CW}(0,t) = \left(A_{CW} + dA_{CW} \frac{min\{(t-t_0), 20T\}}{20T} \right) e^{i\omega t} \tag{3}$$

where t_0 is the time when the amplitude change started, A_{CW} is the last amplitude value considered and dA_{CW} the amplitude increment. One wave cycle T involves about 2000 time steps.

Response to a CW bias

The amplitude of the CW is varied from zero to a maximum of 0.7 with about 40 measurements in between. Results are shown in Fig. 1b, along with the corresponding one from a time-independent approximation. The agreement between the two methods is exact for small intensities, however, after a certain input the output waves are not constant any more but pulsative. This is in accord with the results obtained with the slowly varying envelope approximation for systems with a weak refractive index modulation [15]. It is interesting that the averaged output power is still in agreement with the time-independent results, something not mentioned in earlier work. For higher input values, the solution will again reach a steady state just before going to the second nonlinear jump, after which it will again become pulsative. This time though, the averaged transmitted power is quantitatively different from the one predicted from time-independent calculations.

The nonlinear transmission jump originates from the excitation of a stationary gap soliton when the incident intensity exceeds a certain threshold value. Due to the nonlinear change of the dielectric constant, the photonic gap is shifted locally in the area underneath the soliton, which becomes effectively transparent, resembling a quantum well with the soliton being its bound state solution [18]. This effectively transparent area and the output fields are shown as a function of time during switching in Fig. 2. We obtain a maximum switching time of the order of 100 T_r, or a frequency of 360 GHz, where $T_r = 2L/c$ is roundtrip time in vacuum (the large response time during switch-up is because the input intensity at the jump was very close to the switching threshold).

The incident radiation coupled to that soliton tunnels through the structure and large transmission is achieved. Increasing further the intensity makes the soliton narrower and so the required tunneling length larger. At some point the incident radiation cannot tunnel any more, an instability occurs, and the soliton becomes unstable, ie. it becomes a solitary wave, and it propagates down the structure. Upon hitting the right end of the structure it is destroyed and its light energy leaves in the form of a pulse, while a new soliton is excited in the structure, etc. This is an alternative way of propagation and is something that time-independent theory can not account for. Repeating the calculations for various structure sizes and frequencies we verified [15] that changing the structural parameters so that the ratio of the soliton's width over the structure's length decreases, eg. using more layers or a higher frequency, decreases the threshold intensity for which the solution first becomes pulsative.

The small stable area before the second jump approximately corresponds to the lower transmission branch of the second bistable loop. Here, the intensity at the left front of the structure has become large enough to make it an effectively transparent area decreasing the required tunneling length, so that the wave can once more couple to the soliton and tunnel through the structure. However, for larger systems or frequencies deeper in the gap it may not be observed. The second transmission jump is related to the excitation of two gap solitons, which however, are not stable and so transmission is pulsative. The Fourier transform of the output shows that, after the second transmission jump, the system pulsates at a frequency $\omega a/2\pi c = 0.407 \pm n \times 0.024$, exactly three times the one of the first pulsating solution $\omega a/2\pi c = 0.407 \pm n \times 0.008$, where n is an integer. The system's response in these two areas is summarized in Fig. 3. For much higher input values the response eventually becomes chaotic.

Pulse driven switching

We next turn to the basic objective of this work. We assume a specific constant input amplitude $|A_{CW}| = 0.185$ corresponding to the middle of the first bistable loop. Depending on the system's history, it can be either in the low transmission state I, shown in Fig. 1c, or in the high transmission state II, shown in Fig. 1d, which are both steady states. We want to study the dynamics of a pulse injected into a system like that. More specifically, if it will drive the system to switch from one state to the other, how the fields change in the structure during switching, for which pulse parameters this will happen and if these parameters change for small phase and frequency fluctuations. We assume Gaussian envelope pulses

$$E_P(0,t) = A_P e^{-(t-t_0-5t_w)^2/t_w^2} e^{i\omega t} \tag{4}$$

where A_P is the pulse amplitude, t_0 the time when injection starts, and $W = 2t_w c$ is the pulse's full width at $1/e$ of maximum amplitude. The beginning of time t is the same as for the CW, so there is no phase difference between them. After injection we wait until the system reaches a steady state again and then measure the transmission and reflection coefficients to determine the final state. During this time we save the field values inside the structure every few time steps, as well as the transmitted and reflected waves. This procedure is repeated for various values of A_P and t_w, for both possible initial states. Our results are summarized in Fig. 4. White areas indicate the pulse parameters for which the intended switch was successful while black are for which it failed. In Fig. 4a, or the "Switch" graph, the intended switching scheme is for the same pulse to be able to drive the system from state I to state II and *vise versa.* Fig. 4b, or "Switch All Up", is for a pulse able to drive the system from I to II, but fails to do the opposite, ie. the final state is always II independently from which the initial state was. Similarly, Fig. 4c or "Switch All Down", is for the pulse whose final state is always I, and Fig. 4d or "No Switch", for the pulse that does not induce any switch for any initial state.

We find a rich structure on these parameter planes. Note also that there is a specific cyclic order as one crosses the curves moving to higher pulse energies: → d → b → a → c → etc. This indicates that there must be some kind of energy requirements for each desired switching scheme. After analyzing the curves it was found that only the first one in the "Switch" graph could be assigned to a simple constant energy curve $\mathcal{E} \sim W|A_p|^2$. Since any switching involves the creation or destruction of a stationary soliton, then this should be its energy. In order to put some numbers, if we would assume a nonlinearity $|\alpha| = 10^{-9}$ cm^2/W, then we would need a CW of energy $\simeq 34$ MW/cm^2 and a pulse of width W/c of a few tenths of femtoseconds and energy $\mathcal{E} \simeq 2.5\mu$J/cm^2. These energies may seem large, but they can be sufficiently lowered by increasing the number of layers and using an incident frequency closer the the gap edge.

In order to find more about how the switching occurs, we plotted in Fig. 5 the effective transparent areas and the output fields as a function of time, for the first three curves of Fig. 4a. As expected, for the pulse from the first curve, the energy for the soliton excitation is just right, and the output fields are small compared to the input. For the other curves however, there is an excess of energy. The system has to radiate this energy away before a stable gap soliton can be created. It is interesting to note that this energy goes only in the transmitted wave, not the reflected, and it consists of a series of pulses [14]. For the second curve in Fig. 4a there is one pulse, for the third there are two etc. The width and frequency of the pulses are independent of the incident pulse, they are the known pulsating solutions we found earlier. So the system temporally goes into a pulsating state to radiate away the energy excess before settling down into a stable state. If this energy excess is approximately equal to an integer number of pulses (the solitary waves from the unstable solutions), then we will have a successful switch, otherwise it will fail. A similar picture is found in Fig. 6 when plotting the system's response during switch down for the first three curves in Fig. 4a. We note again that we use here the exactly same pulses as before for the switch up. So the same pulse is capable of switching the system up, and if reused, switching the system back down. Using the numbers assumed before for α, the pulses used in Figs. 5 and 6 are (a) $W/c = 14$ fs, $\mathcal{E}$=2.5 μJ/cm^2, (b) $W/c = 28$ fs, $\mathcal{E}$=12 μJ/cm^2, (c) $W/c = 42$ fs, $\mathcal{E}$=32 μJ/cm^2.

Up to now, the injected pulse has been treated only as an amplitude modulation of the CW source, ie. they had the same exactly frequency and there was no phase difference between them. The naturally rising question is how an initial random phase between the CW and the pulse, or a slightly different frequency affect our results. We repeated the simulations for various values of an initial phase difference, first keeping them with the same frequency. Results are shown in Fig. 7, where we plot only the "Switch" graph for four values of phase difference. We see that although the graphs are qualitatively the same, they have quantitative differences. The result is that there is not a set of pulse parameters that would perform the desired switching successfully for any initial phase difference. The same holds for the other switching operations of Fig. 4 as well. Thus the pulse can not be incoherent with the CW, ie. generated at different sources, if a controlled and reproducible switching mechanism is desired, but rather it should be introduced as an amplitude modulation of the CW. However, if this phase could be controlled, then the switching operation would be controlled, and a single pulse would be able to perform all different operations.

The picture does not change if we use pulses of slightly different frequency from the source. We used various pulses with frequencies both higher and lower than the CW, and we found a sensitive, rather chaotic, dependence on the initial phase at injection time. The origin of this complex response, if it is an artifact of the simple Kerr-type nonlinearity model that we used, and if it should appear for other kinds of nonlinearities, is not yet clear to as. More work is also needed on how these results would change if one used a different $|A_{CW}|$ not in the middle of the bistable loop, a wider or narrower bistable loop etc., but these would go more into the scope of engineering.

Linear lattice with a nonlinear impurity layer

Besides increasing the number of layers to achieve lower switching thresholds, one can use a periodic array of linear layers $\epsilon = \epsilon_0 \epsilon_r$ with a nonlinear impurity layer [19, 20, 21, 22] $\epsilon = \epsilon_0(\epsilon_r' + \alpha|\vec{E}|^2)$ where $\epsilon_r \neq \epsilon_r'$ and we will use $\alpha = +1$ and $\gamma = 0$. This system is effectively a Fabry-Perot cavity with the impurity (cavity) mode inside the photonic gap, as shown in Fig. 8a. The bistable response originates from its nonlinear modulation with light intensity. The deeper this mode is in the gap, the stronger the linear dispersion for frequencies close to it. Because of the high Q of the mode, we can use frequencies extremely close to it achieving very low switching thresholds [22]. Here however we only want to study the switching mechanism, so we will use a shallow impurity mode.

The bistable input-output diagram, the output fields during switching and the field distributions in the two transmission branches are also shown in Fig. 8. We observe a smaller relaxation time and of course the absence of pulsating solutions. The parameters used are $\epsilon_r' = 1$ and $\omega a/2\pi c = 0.407$ which corresponds to a frequency between the mode and the gap edge. We want to test if a pulse can drive this system in switching between the two different transmission states, and again test our results against phase and frequency perturbations. The two states shown in Fig. 8 are for an input CW amplitude of $|A_{CW}| = 0.16$. The results for coherent, pulse and CW, are shown in Fig.9. We see that any desired form of switching can still be achieved, but the parameter plane graphs no more bare any simple explanations as the ones obtained for the nonlinear superlattice. Repeating the simulations for incoherent beams and different frequencies we obtain the same exactly results as before. Only phase-locked beams can produce controlled and reproducible switching.

Conclusions

We have studied the time-dependent switching properties of nonlinear dielectric multilayer systems for frequencies inside the photonic band gap of the corresponding linear structure. The system's response is characterized by both stable and self-pulsing solutions. We examined the dynamics of driving the system between different transmission states by pulse injection, and found correlations between the pulse, the stationary gap soliton and the unstable solitary waves. A small dependence on the phase difference between the pulse and the CW is also found, requiring coherent beams for fully controlled and reproducible switching. Similar results are also found for the case of a linear periodic structure with a nonlinear impurity.

Acknowledgments

Ames Laboratory is operated for the U. S. Department of Energy by Iowa State University under contract No. W-7405-ENG-82. This work was supported by the Director of Energy Research office of Basic Energy Science and Advanced Energy Projects.

Bibliography

[1] A. C. Newell and J. V. Moloney, *Nonlinear Optics* (Addison-Wesley, Redwood CA, 1992).

[2] H. M. Gibbs, *Optical Bistability: Controlling Light with Light* (Academic, Orlando FL, 1985).

[3] H. G. Winful, J. H. Marburger, and E. Garmire, Appl. Phys. Lett **35**, 379 (1979); H. G. Winful, and G. D. Cooperman, Appl. Phys. Lett **40**, 298 (1982).

[4] *Photonic Band Gaps and Localization*, edited by C. M. Soukoulis (Plenum, New York, 1993); *Photonic Band Gap Materials*, edited by C. M. Soukoulis (Klumer, Dordrecht, 1996).

[5] Wei Chen and D. L. Mills, Phys. Rev. B **36**, 6269 (1987); Phys. Rev. Lett. **58**, 160 (1987).

[6] C. Martijn de Sterke and J. E. Sipe, in *Progress in Optics*, edited by E. Wolf (Elsevier, Amsterdam, 1994), Vol. 33.

[7] D. L. Mills and S. E. Trullinger, Phys. Rev. B **36**, 947 (1987).

[8] C. Martijn de Sterke and J. E. Sipe, Phys. Rev. A **42**, 2858 (1990).

[9] A. B. Aceves, C. De Angelis and S. Wabnitz, Opt. Lett. **17**, 1566 (1992).

[10] Sajeev John and Neşet Aközbek, Phys. Rev. Lett. **71**, 1168 (1993); Neşet Aközbek and Sajeev John, Phys. Rev. E **57**, 2287 (1998).

[11] Michael Scalora, Jonathan P. Dowling, Charles M. Bowden, and Mark J. Bloemer, Phys. Rev. Lett. **73**, 1368 (1994).

[12] P. Tran, Opt. Lett. **21**, 1138 (1996).

[13] N. D. Sankey, D. F. Prelewitz, and T. G. Brown, Appl. Phys. Lett. **60**, 1427 (1992).

[14] B. J. Eggleton, C. Martijn de Sterke, R. E. Slusher, J. Opt. Soc. Am. B **14**, 2980 (1997).

[15] S. S. Tarng, K. Tai, J. L. Jewell, H. M. Gibbs, A. C. Gossard, S. L. McCall, A. Passner, T. N. C. Venkatesan, W. Wiegmann, App. Phys. Lett. **40**, 205 (1982).

[16] J. He, M. Cada, M.-A. Dupertuis, D. Martin, F. Morier-Genoud, C. Rolland, A. J. SpringThorpe, Appl. Phys. Lett. **63**, 866 (1993).

[17] Allen Taflove, *Computational Electrodynamics: The Finite-Difference Time-Domain Method* (Artech House, Boston, 1995).

[18] Elefterios Lidorikis, Qiming Li, and Costas M. Soukoulis, Phys. Rev. B **54**, 10249 (1996).

[19] Stojan Radic, Nicholas George, and Govind P. Agrawal, J. Opt. Soc. Am. B **12**, 671 (1995).

[20] Toshiaki Hattori, Noriaki Tsurumachi, and Hiroki Nakatsuka, J. Opt. Soc. Am. B **14**, 348 (1997).

[21] Rongzhou Wang, Jinming Dong, and D. Y. Xing, Phys. Rev. E **55**, 6301 (1997).

[22] E. Lidorikis, K. Busch, Qiming Li, C. T. Chan, and Costas M. Soukoulis, Phys. Rev. B **56**, 15090 (1997).

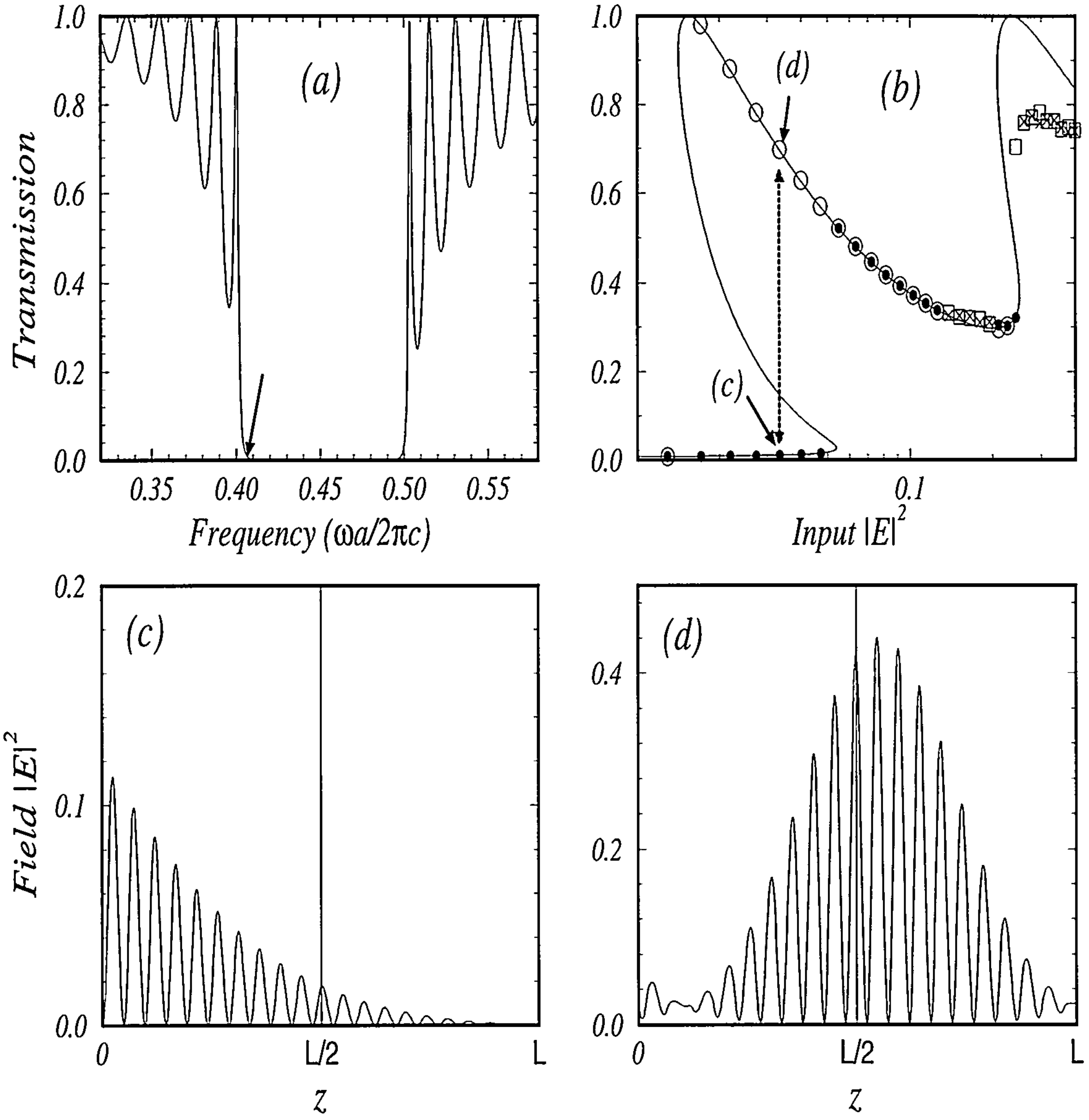

Figure 1 (a) The linear transmission diagram. The small arrow indicates the frequency we used in the nonlinear study. (b) The nonlinear response: closed/(open) circles correspond to steady states when increasing/(decreasing) the intensity and crosses/(open squares) correspond to self-pulsing states when increasing/(decreasing) the intensity. (c) Intensity configuration for low transmission state. (d) Intensity configuration for high transmission state.

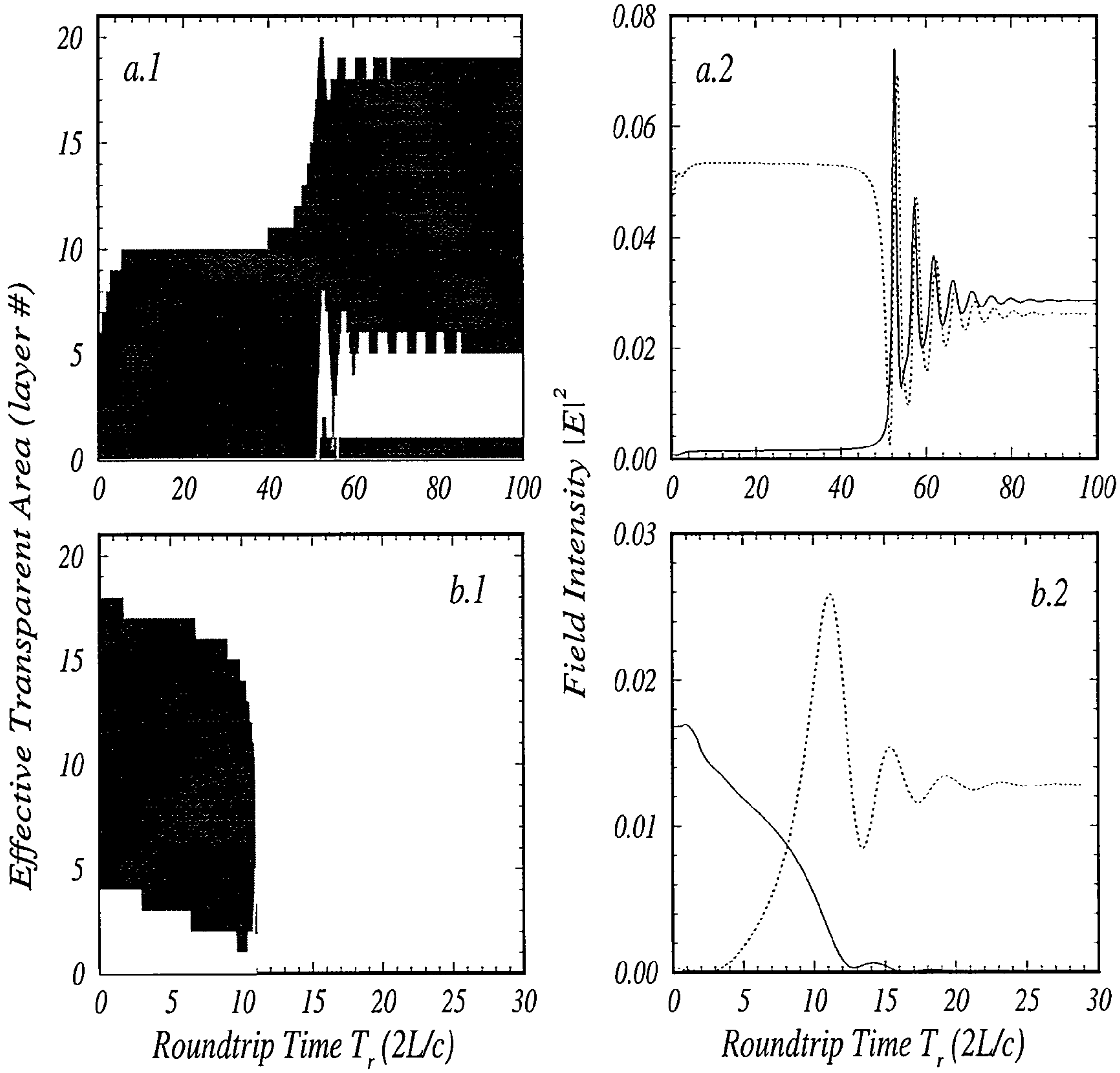

Figure 2 (a) Switch-up and (b) switch-down dynamics. (1) Effective transparent area *vs* time and (2) output fields. Solid and dotted lines correspond to transmitted and reflected waves respectively.

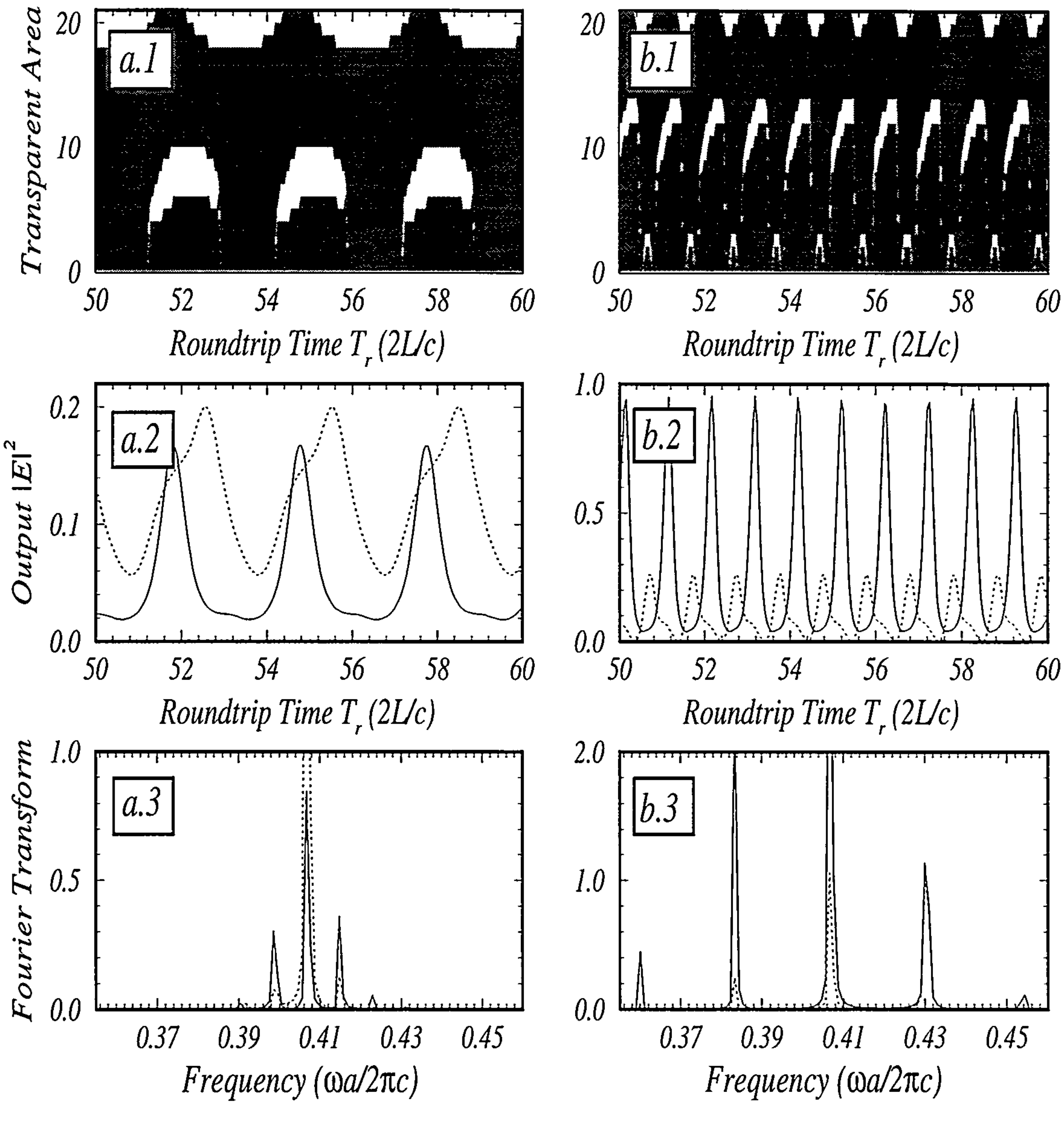

Figure 3 (a) First and (b) second self-pulsing solutions. (1) Effective transparent area, (2) output fields; solid/(dotted) for transmitted/(reflected) waves, (3) Fourier transform of output waves.

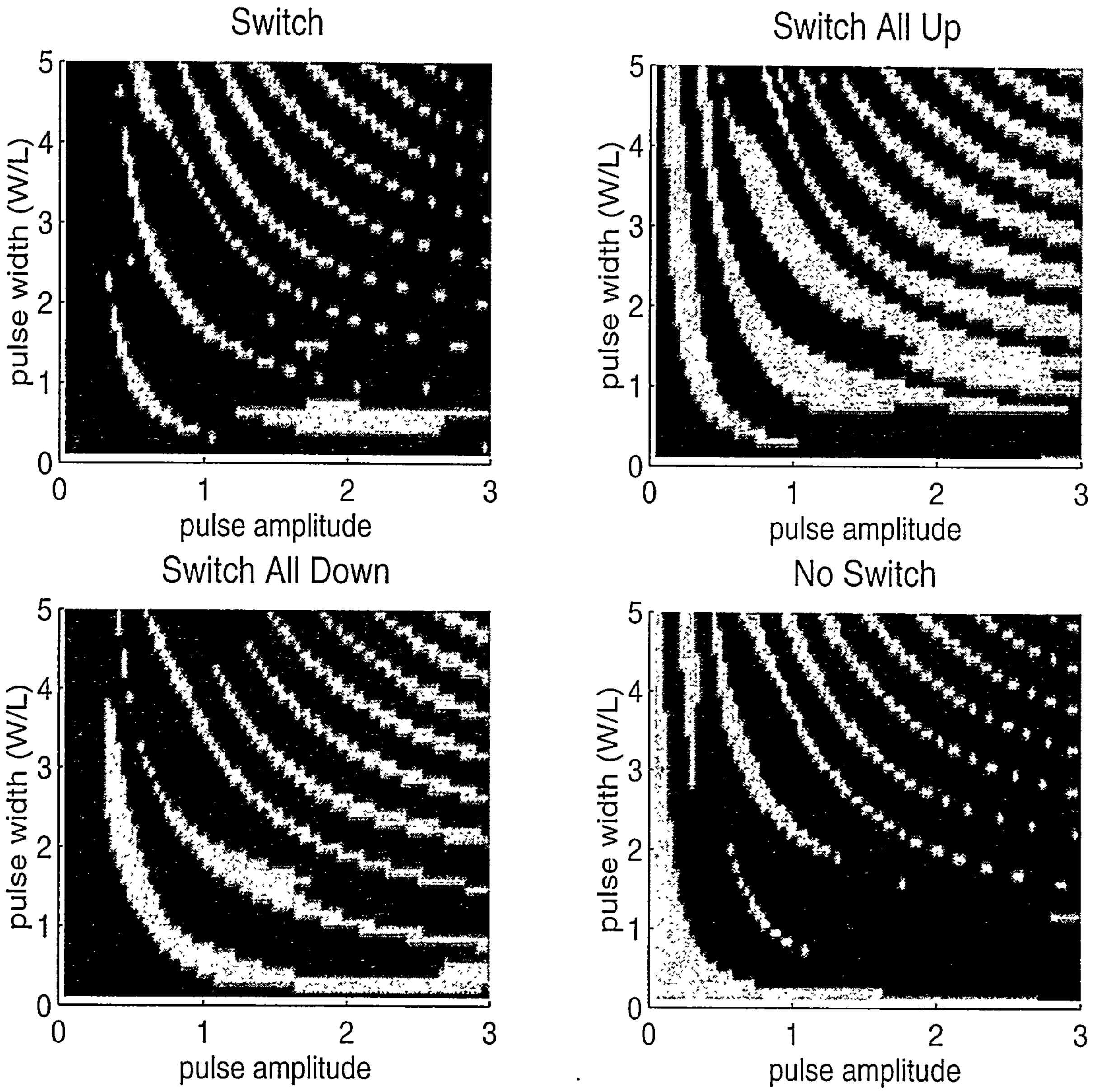

Figure 4 The four different switching schemes: (a) Final state opposite of initial, (b) final state always high transmission state, (c) final state always low transmission state, (d) no change of state. White areas indicate successful operation while black indicate failure.

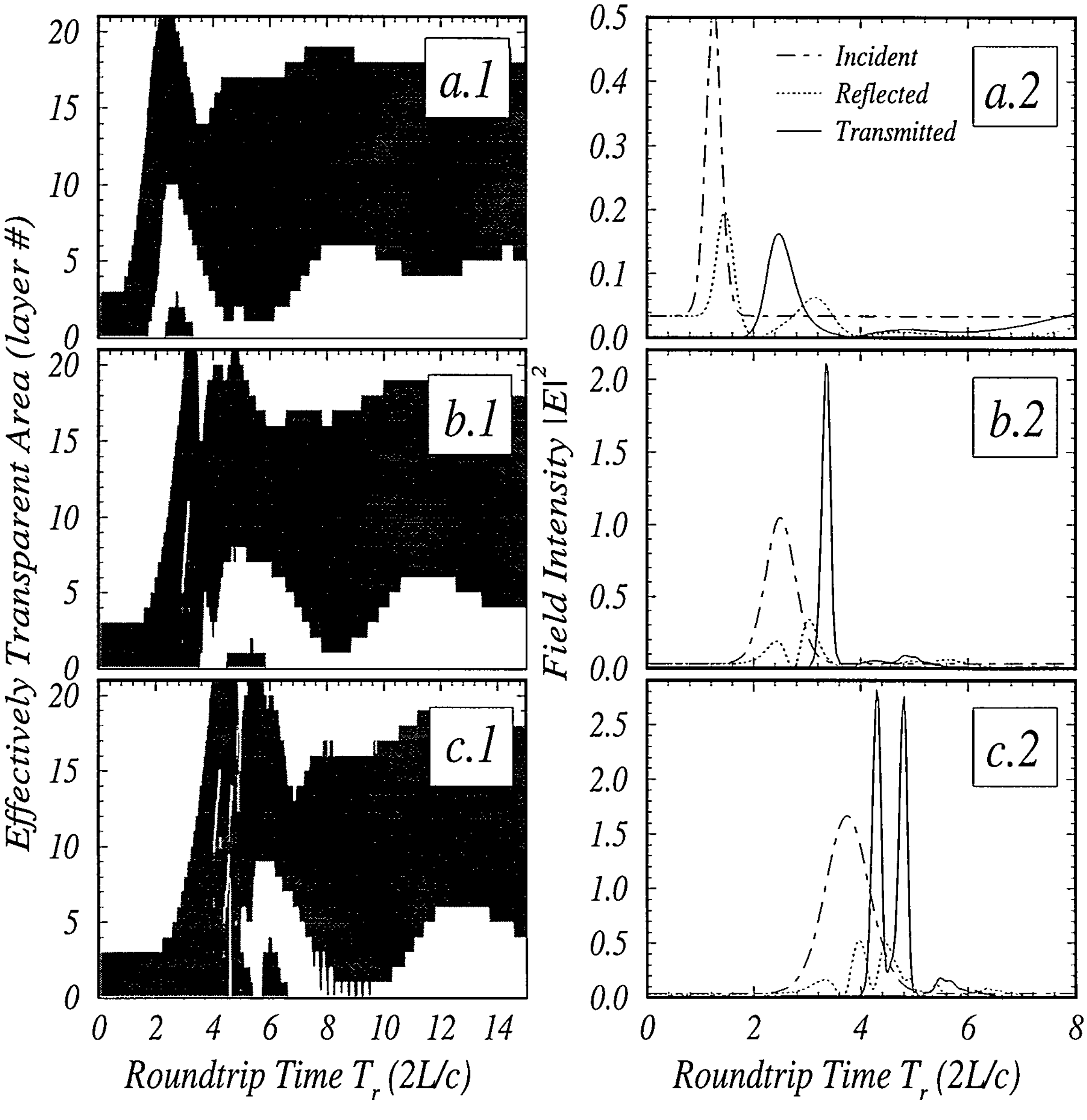

Figure 5 Switch-up dynamics for (a) First, (b) second and (c) third white curves in the "Switch" graph of Fig. 4. (1) Effectively transparent area and (2) input and output waves.

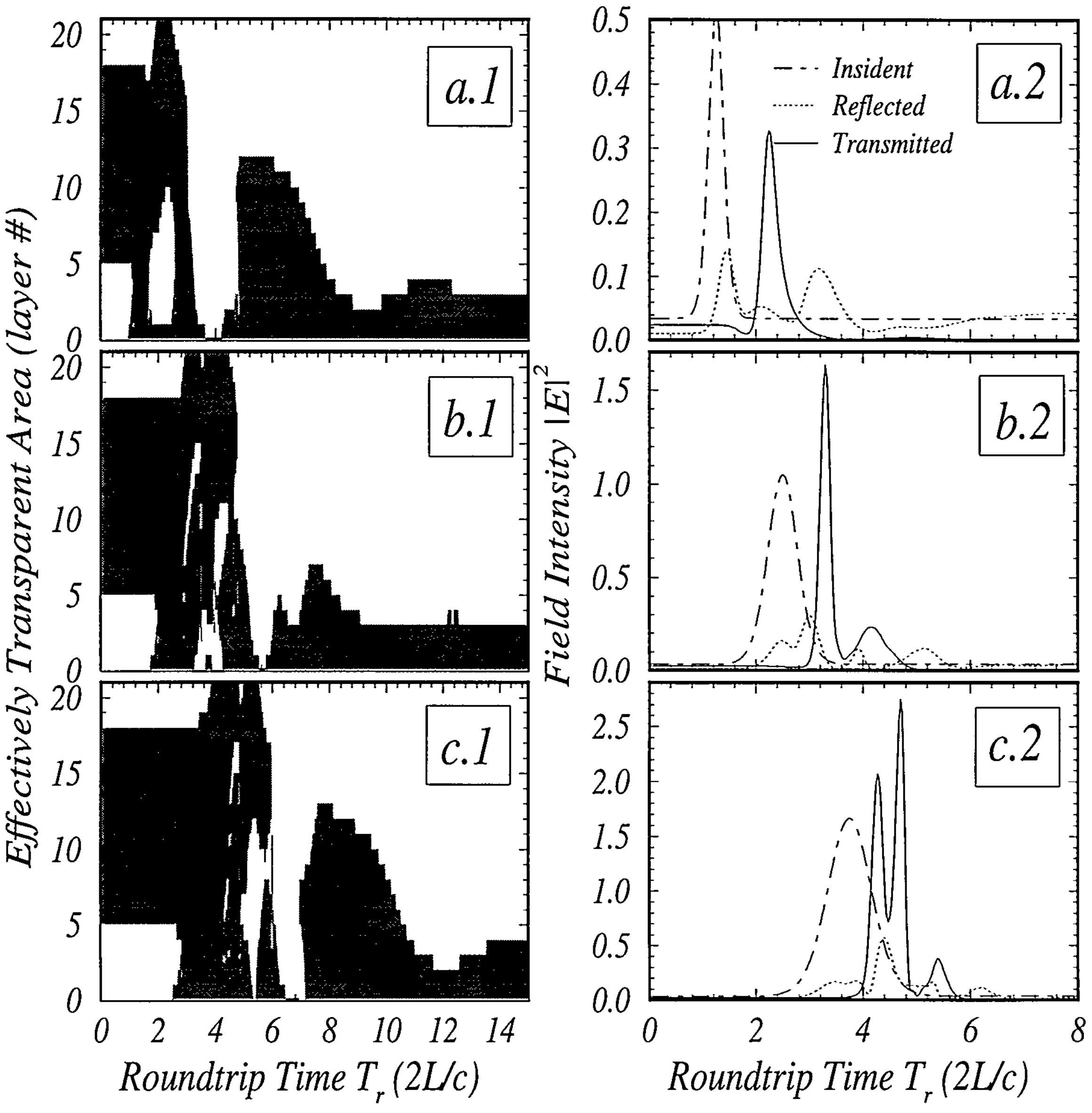

Figure 6 Switch-down dynamics for the first three curves of the "Switch" graph of Fig. 4. Labeling is the same as Fig. 5.

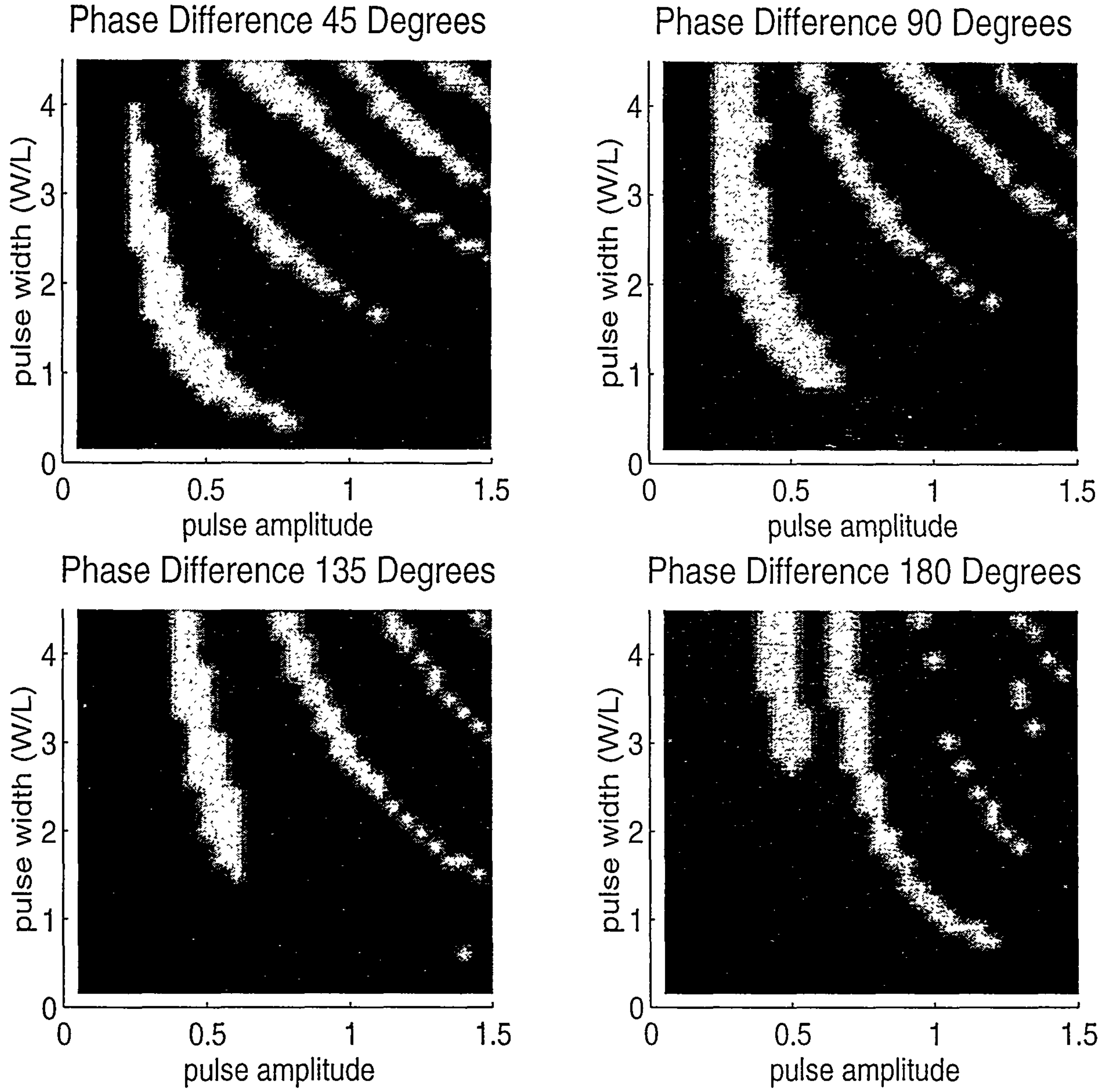

Figure 7 The "Switch" area for four different values of phase difference between CW and pulse. No overlap of these curves is found.

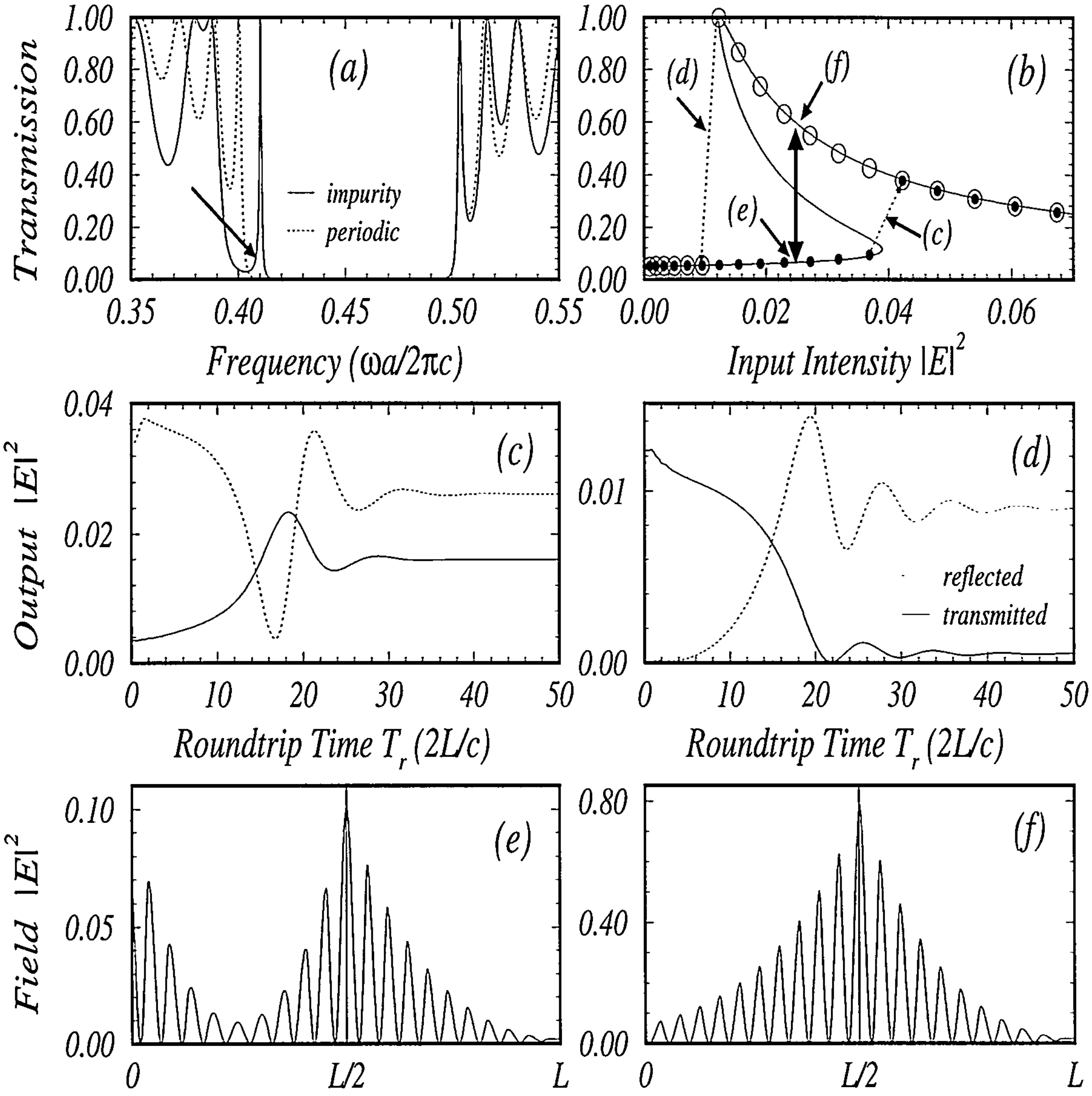

Figure 8 Linear lattice with a nonlinear impurity layer: (a) Linear transmission diagrams, (b) nonlinear response; solid/(open) circles for increasing/(decreasing) CW intensity, (c) output waves during switch-up and (d) switch-down, (e) intensity configuration for the low transmission state and (f) high transmission state.

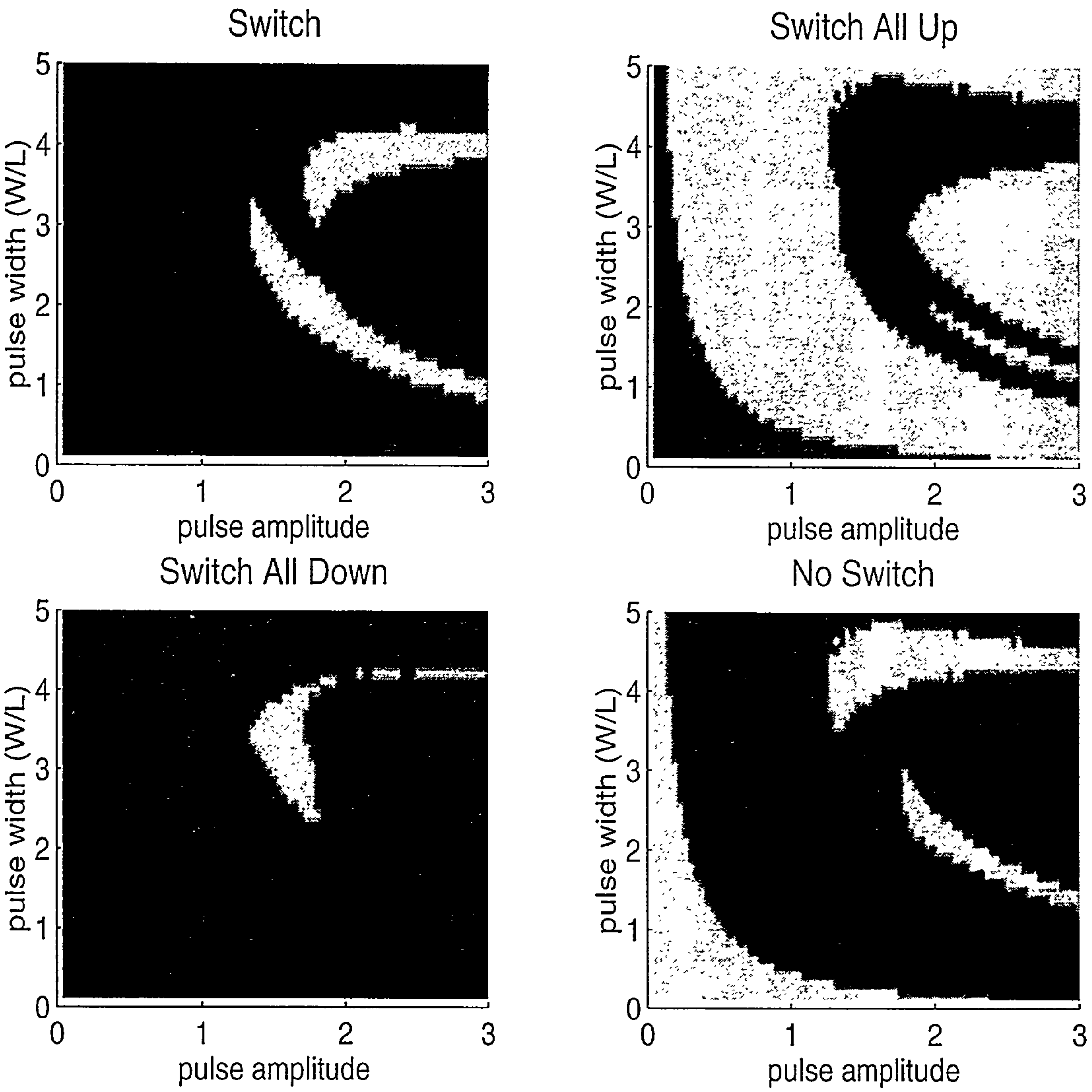

Figure 9 The four switching schemes described in Fig. 4 for the case of a linear lattice with a nonlinear impurity layer. No simple curved structure is found here.

CHAPTER 5. OPTICAL BISTABILITY IN COLLOIDAL CRYSTALS

A paper published in the journal of Physical Review E [1]

Elefterios Lidorikis, Qiming Li, and Costas M. Soukoulis

Abstract

We present a one dimensional model for the nonlinear response of a colloidal crystal to intense light illumination along a high symmetry direction. The strong coupling between light and the colloidal lattice, via the electric gradient force acting upon the particles, induces a novel large optical nonlinearity. We obtain bistable behavior when the incident frequency is inside the stopband of the periodic structure, with decreasing switching intensity as the frequency increases. The transmission characteristics and the magnitude of the switching threshold intensity are also in good agreement with a recent experiment.

Introduction

Photonic band gap (PBG) materials [1] do not allow propagation of electromagnetic waves within a certain frequency range, thereby opening the possibility of studying new physics within the gap. In addition, many novel applications of these PBG crystals have been proposed, with operating frequencies ranging from microwaves to the optical regime[1, 2]. Structures exhibiting full photonic band gaps in the microwave[3], millimeter[4] and submillimeter[5] regimes have already been fabricated, but scaling these structures down to the optical regime has remained a challenge. One way to construct PBG crystals in the optical regime is by growing polystyrene

---

[1] PRE 55, 3613 (1997)

colloidal crystals[3, 4, 5, 9], which have lattice spacing comparable to the wavelength of light. Such colloidal crystals do not exhibit a complete PBG, because the concentration and the index of refraction of the polystyrene spheres relative to water are not yet sufficiently high. However, they are very useful in studying PBG effects seen only in particular directions. In addition, they can be used in nonlinear optical studies. It is expected that the PBG effects can be strongly affected by nonlinear optical effects. In particular, it has been shown that intensity-dependent index of refraction can cause a shift in the locations of the band gap[10]. That is, if the index of refraction of either the suspended polystyrene spheres or water is intensity-dependent, then the width and the position of the stopband (or gap) will change under intense illumination. For example, a decrease of the index of refraction in water upon illumination will widen the gap, and, therefore, inhibits the propagation of the probe beam. Such an optical switching for light control is of great interest to the optics community.

In a recent experiment[4], optical switching and optical bistability were observed, when intense light was transmitted through a colloidal crystal. Simple switching was observed near the low-frequency end of the stopband, whereas bistability and multistability occurred at the center or near the high frequency end. The switching threshold was found to decrease as the incident frequency increased. These aspects are inconsistent with the response of a material with the conventional intensity-dependent nonlinearity[4]. The measured nonlinear coefficient n' inside the transmission band, $4 \times 10^{-10} cm^2/W$, is also several orders of magnitude larger than the electronic nonlinearity of both materials.

In this paper, we present a one dimensional model for the nonlinear response of a colloidal crystal to intense light incident along a high symmetry direction, based on the electrostriction mechanism[4]. Light is strongly scattered by the periodic arrangement of the colloidal particles inside the crystal, thus creating a spatially varying field. The polystyrene spheres, polarized by the electric field, will move in response to the electric gradient force. Such a structure change in turn will alter the propagation of light. The optical response is thus controlled by the the stationary configuration that results from the balance between the elastic and the electric gradient forces. We assume that the electric gradient forces are not strong enough to destroy the polystyrene spheres' crystalline structure and furthermore, that the changes in interparticle separation are small compared to the mean interparticle separation. Assuming the incident wave can be approximated as plane waves due to the large beam spot size, the structural change induced by light incident along a high symmetry direction will be primarily in the propagating direction. We neglect possible transverse effects and describe the three dimensional lattice by a one dimensional harmonic lattice model. Numerical calculations of the transmission characteristics, based on known physical properties of the colloidal crystal and a simplification to a layered structure, show good agreement with experiment. In particular, we find bistable behavior inside the stopband at intensities comparable to the observed switching threshold. The switching threshold is found to decrease as the incident frequency increases. We need to emphasize that such a nonlinearity necessarily depends on the exact stationary configuration of the lattice and therefore cannot be described with a simple effective intensity- and/or frequency-dependent dielectric constant.

This paper is organized as follows. In section II, we introduce our one-dimensional lattice model for the optical nonlinearity in colloidal crystal. In section III, we present results of calculations on the optical bistability and compare them with experiments. Conclusions and discussions are presented in section IV.

One dimensional model of optical nonlinearity

In general, wave propagation in periodic structures is a complex phenomenon. Three dimensional scattering of light plays an important role in determining the nonlinear optical response of a colloidal crystal to incident light. However, simplification is possible if, a) the incident wave is plane-wave-like; b) the light is normally incident upon a high symmetry plane of the crystal lattice, and c) no transverse instability exits. Under these conditions, the structure can be viewed as a layered system. One dimensional modeling of the optical response is expected to be appropriate with correctly calculated physical parameters. The first condition ensures all spheres within one layer are equivalent, hence there should be no lateral lattice displacement, as required by symmetry. The second condition makes the layered structure more distinct since the distance between the layers is large. The third condition essentially requires that the structure is stable under illumination.

The colloidal crystal used in experiment[4] had a face-centered-cubic structure formed by polystyrene spheres (n_1=1.59) of approximately d_1=120 nm in diameter, at concentration f around 7%, dispersed in water (n_2=1.33). Light was normally incident upon the [111] plane which was parallel to the surfaces of the container. Due to the relatively large spot size, we approximate the incident wave as plane-waves. To a low intensity incident wave from the [111] direction, the fcc colloidal crystal acts essentially as a Bragg reflector (linear regime). The system is naturally simplified as a one dimensional bilayer structure consistent of alternating segments of polystyrene sphere layers (a mixture of polystyrene spheres and water with total thickness d_1) and pure water layers. With sphere concentration of 6.9%, the distance between the polystyrene sphere layers[11] is R_0=216 nm. The thickness of the water layer is then d_2=R_0-d_1=96 nm. The average index of refraction of the polystyrene layer is estimated[12] to be 1.36. Since the sample thickness is L=100 μm, the total number of bilayer units is N=L/R_0=463. The linear (zero intensity limit) transmission coefficient versus the wavelength in the [111] direction is shown in Fig. 1, calculated with the parameters mentioned above. Notice that there is excellent agreement[13] between our theoretical results of Fig. 1 and the experimental results of Fig. 2 in Ref. 7. This shows our model parameters describe very well the linear transmission of the colloidal crystal.

To illustrate that the nonlinear response of the colloidal crystal cannot be described by a one dimensional layered model with the conventional Kerr type nonlinearity (intensity-dependent dielectric constant), we show in Fig. 2 the nonlinear response of such a system, assuming that the effective index of refraction n_2 of the "water" has the form, $n_2 = n_2^o + n'|E|^2$. n_2^o=1.33 is the linear index of refraction of the medium and the nonlinear coefficient is taken to be the experimentally measured nonlinearity, $n' = 4 \times 10^{-10} cm^2/W$. Taking the propagation direction to be the z direction, we can solve the propagation of light governed by the following wave equation

$$\frac{d^2E}{dz^2} + \frac{n^2(z)\omega^2}{c^2}E = 0, \tag{1}$$

where n(z) is the index of refraction of our model which consists of alternating layers of linear and nonlinear medium, as specified above. Indeed, bistable behavior is obtained, as can be clearly seen in Fig. 2. The existence of such bistability phenomena in distributed feedback structures with intensity-dependent dielectric constants were predicted[14] theoretically and their properties have been investigated intensively[15]. Similar bistable behavior has been seen[16, 17, 18] in the discrete case of the electronic version of Eq. (2). However, the threshold intensity for the onset of the bistable behavior is in the order of 10 MW/cm^2, at least three orders of magnitude larger than the experimentally measured value of about 5 kW/cm^2. We see that a simple solution of Eq. (1) with an effective intensity-dependent nonlinearity indeed produces bistable behavior, but its predictions for the incident intensity threshold are unrealistically high. Clearly, a novel form of nonlinearity must be in action.

An interesting mechanism due to electrostriction was proposed[4] to be responsible for the nonlinear behavior in the colloidal crystal. In the absence of light illumination, the short-range screened electrostatic repulsive forces[19] between the spheres balances the weak long-range attractive force of Van der Waals type and produces an equilibrium configuration for the polystyrene spheres, with nearest neighbor separation $S_0 = \alpha/\sqrt{2}$ where α is the fcc lattice constant. When intense electromagnetic (EM) wave is incident upon the crystal, the dielectric spheres get polarized by the electric field and move in response to the gradient force [19] from the spatially varying field. This in turn alters the propagation of EM wave. Consequently, optical nonlinearity result. Ultimately, the optical response under a given illumination is controlled by the steady state lattice configuration which has to be determined by the balance of the elastic and electric gradient forces.

To determine whether the electrostriction mechanism is indeed responsible for the experimental observations, we have to solve simultaneously wave propagation equations and lattice dynamics incorporating both elastic and electric gradient forces. Here we propose a simple one dimensional lattice model that can be solved straightforwardly but still contains the essential physics to account for the optical bistability observed in experiment. We have argued that under the experimental condition, a one dimensional layered model is appropriate to describe the transmission of wave along the propagation direction. The linear transmission property of this one dimensional lattice, consisting of alternating layers of polystyrene and water, has already been described (Fig. 1). To model the nonlinear response, we need knowledge of the lattice dynamics which is governed by the elastic and electric gradient forces.

We assume that for small fluctuations around the equilibrium configuration, the harmonic approximation is correct. We can then describe the motion of polystyrene spheres as if they were connected with each other with ideal springs. The force constant k of the springs can be roughly estimated by linearizing the screened electrostatic repulsive force[22],

$$F_{el} = \frac{(Ze)^2}{4\pi\epsilon R^2}\frac{1+\kappa R}{1+\kappa a}\exp[-\kappa(R-a)], \tag{2}$$

at the layer equilibrium position $R = R_0$. This leads to an expression $F_{el} = F_{harm} = k\Delta R$, where $\Delta R = R - R_0$ is the displacement from the equilibrium position. Z is the number of charges on the particle, κ is the inverse screening length, and a is the radius of the particle. Using $\epsilon = 1.33\epsilon_0$, $a = 60$ nm, $R_0 = 216$ nm, and assuming typical values[19] of Z=1000e$^-$ and $\kappa = 5 \times 10^7 m^{-1}$, we obtain k = 1.8×10^{-4}N/m. This corresponds to a bulk moduli B$\sim$ k/R_0 $\sim$1000 N/M^2, a reasonable value for colloidal crystals[19]. As we will see later, the electrostriction nonlinearity is inversely proportional to k. Only the order of the magnitude of k is relevant for our purpose. For definiteness, we take k = 1.8×10^{-4}N/m in the following calculations.

The gradient force on a sphere F$_{gr}$ along the propagation direction z, can be calculated by taking the spatial derivative of it's polarization energy, i. e., $F_{gr} = -d(U_p)/dz$. A crude estimate of this force is

$$F_{gr} \simeq 4\pi n_1^2\epsilon_0 \frac{m^2-1}{m^2+2}a^3\frac{1}{2}\frac{\Delta|E|^2}{2a} \tag{3}$$

where $m^2 = (n_1/n_2)^2$ is the dielectric contrast between polystyrene spheres and water, a is the radius of the spheres, and the factor $\frac{1}{2}$ comes from averaging over a time period. $\Delta|E|^2$ is the field intensity difference across a sphere's diameter. For our model's parameters this gives $F_{gr} \simeq C\Delta|E|^2$, $C = 2.2 \times 10^{-26} Nm^2/V^2$.

The optical response of the colloidal crystal is determined by the steady state configuration. In our one dimensional model, this is reflected as the steady state lattice configuration representing the configuration of the layers. Taking nearest neighbor interactions only and denoting by ΔR_n the change from the equilibrium separation of particles n and n+1, we have for the steady state that

$$F_{gr} = -F_{harm} = -k(\Delta R_n - \Delta R_{n-1}). \tag{4}$$

The gradient force F_{gr} on each polystyrene layer has to be calculated from the electric field distribution via Eq. (3) for the given lattice configuration $\{R_n\}$.

The transmission characteristics are obtained by solving Eqs. (1) and (4) self-consistently through iteration, for a given input. In actual calculations, however, this is done for a given output because the presence of bistable or multistable behavior. In a nonlinear one-dimensional model, each output corresponds to exactly one solution, while a given input may correspond to more than one output solutions (bistability). The input intensity can be reconstructed once the transmission coefficient is calculated after solving Eq. (1). We start with the equilibrium configuration in the absence of light in which all the layers is equally spaced with distance R_0. The wave field E(z) is then calculated from Eq. (1), with n(z) given by the exact one-dimensional lattice configuration $\{R_n\}$. n(z) equals to 1.36 if z is in the polystyrene layer and 1.33 otherwise. The gradient force and the elastic force is then calculated and R_n is increased or decreased depending the direction of the total force. The wave field is then recalculated and accordingly $\{R_n\}$ readjusted. This iteration procedure continues until the total force vanishes on each polystyrene layer. The final configuration will be the steady state configuration, and the corresponding field represents the actual optical response of the system. Twenty iterations are usually required before a steady state self-consistent configuration is achieved.

We point out that the present situation is analogous to the problem of an electron moving in a one-dimensional harmonic lattice with electron-lattice interactions. Such an analogy may help to understand the nonlinear optical response when the frequency is inside the stopband. We comment that neither in the polystyrene spheres nor in the water have we assumed any intrinsic nonlinearity. The nonlinear response of the colloidal crystal is entirely due to the coupling between the light and the lattice. In principle, such coupling exists in all materials. But the extreme softness of colloidal lattices relative to conventional crystals, reflected in the small value of the effective spring constant k, makes the observation of nonlinear effects possible in these materials.

Optical bistability

As a first check of our model, we have numerically calculated the sign and the strength of the effective nonlinearity for a frequency (λ=514 nm) inside the transmission band. We found that the colloidal crystal linearly expands with the incident intensity of the EM wave, with a slope of about $1nm$ per $30kW/cm^2$. This corresponds to a relative linear expansion of the order $\Delta L/L \simeq 10^-5$, which is quite small as required by our harmonic assumption. The resulted phase shift in the transmitted wave can be related to an effective positive nonlinear index of refraction by

$$\frac{\omega}{c}(n_2 - 1)\Delta L \simeq \frac{\omega}{c} n' |E_0|^2 L \tag{5}$$

where $|E_0|$ is the incident intensity. For our system we estimate n$'$ $\simeq$ $10^{-10} cm^2$/W. This is in excellent agreement with the experimental value[4] of $n' \simeq 4 \times 10^{-10} cm^2$/W, considering that the value of the force constant is only estimated with typical values of physical properties for colloidal crystals. We find that within the transmission band, the nonlinearity n$'$ scales almost linearly with 1/k, but with no appreciable frequency dependence. The experimentally observed nonlinearity can be matched with the choice k$\simeq 4.4 \times 10^{-5} N/m$ and a corresponding bulk moduli B$\sim 250 N/m^2$. For definiteness we continue to use the initial estimated value of k. Changing value of k amounts to rescale the light intensities, since the actual contraction or expansion is controlled by the ratio of the elastic force and the gradient force, ie, only the ratio of the k and light intensity matters.

Multistability and switching threshold intensities are also correctly predicted within our model for frequencies inside the band gap. The local expansions and contractions of the lattice under illumination are the origin of the bistable behavior. Normally, transmission is forbidden in the gap of a periodic system. However, lattice distortion allows the existence of localized modes in the gap. Under appropriate conditions, the coupling of these localized modes with the radiation can produce resonant transmission. This is clearly seen in Fig. 3, where the local lattice expansion (a), the field intensity averaged in each sphere (b), and the intensity gradient (c), are shown as a function of the lattice plane, exactly at a transmission resonance for a frequency inside the stopband. Notice that there is a strong lattice deformation (solid curve in Fig. 3a) at the middle of the crystal, sustained by the strong field intensities (solid curve in Fig. 3b) and the intensity gradient. Similar behavior is seen for the case of the second transmission resonance (dotted lines in Fig. 3). This work clearly shows that there exists a strong light-lattice interaction, giving rise to lattice deformations which in turn produces localized solutions as "soliton-like" objects[20, 21]. When these "soliton-like" objects appear symmetrically in the crystal, a transmission resonance is expected. Also, the longer the wavelength and the higher the multistability order are, the larger the maximum values of these deformations become. The bistable behavior originates from these field-distribution-specific structure changes. We point out that the total expansion of the lattice is still relatively small, generally in the order of 80 to 200 nm for each "soliton-like" object present in the structure.

The transmission characteristics are shown in Fig. 4, for four different wavelengths as were indicated in Fig. 1. We see that our model captures the most essential features of the nonlinear response of the colloidal crystal, as compared with the experimental results presented in Fig. 3 of Ref. 7. Notice that this model correctly predicts the magnitude of the switching threshold intensities, they are of the order of (20-40) kW/cm^2 and not of the order of 10^4 kW/cm^2 that the simple model with an intensity-dependent dielectric constant predicts (see Fig. 2) . The switching threshold intensities get smaller as we move from the long to the short wavelength side of the stopband, in agreement with experiment[4]. Bistability is observed when the lattice is distorted enough so to sustain a localized mode. This will happen if the local expansion is large enough to locally shift the effective gap to longer wavelengths [22]. Thus, the closer the incident frequency is to the small wavelength side of the gap, the smaller the lattice distortion needed to onset bistability, and thus the smaller the switching powers are.

Discrepancy with the experimental data is found for large incident intensities and in the low frequency side of the gap. Multistability was observed only in the high frequency side while for midgap frequencies the crystal is bistable and for low frequencies it is non bistable [4]. Also, at high intensities only instabilities were observed experimentally, in contrast to our model that predicts multistable behavior for all gap frequencies and all intensities. However, it is for the long wavelengths and the high intensities that the required lattice expansions get unrealistically large. The total lattice expansion versus the transmitted intensity are shown in Fig. 5, for the four wavelengths indicated in Fig. 1. Every local maximum in these curves corresponds to a transmission resonance. Since the crystal can not expand more than a certain maximum limit, an external pressure must be inserted into our model to limit its expansion. Numerical studies incorporating an external pressure show that while multistability is still predicted for all frequencies, the required local expansions and contractions, (with total expansion being constant and limited), and light intensities are much larger, making the starting assumption of a slightly perturbed harmonic lattice invalid. With large lattice distortions, approximation to a one dimensional structure also becomes questionable, and this may be the main reason for the discrepancy. The neglect of light absorption in water may also be a contributed factor to the discrepancy. Absorption reduces the light intensity nonuniformly, and thus may affect the nonlinear response.

Discussions and Conclusions

We have shown that several essential features of the nonlinear response in colloidal crystals can be accounted for by a simple one dimensional model that incorporates the lattice distortions under intense light illumination. In this one dimensional model, the colloidal crystal is simplified as a one-dimensional layered system consisting of alternating layers of polystyrene spheres and water. The polystyrene layers represent high symmetry planes of the colloidal crystal normal to the propagating direction and are modeled as elastic media deforming under the act of the gradient force from the electric field. Based on physical properties of the colloidal crystal, we are able to estimate the effective elastic spring constant. The wave equation of the electric field and the lattice dynamics of this one dimensional systems is then solved simultaneously to obtain the steady state response. We are able to obtain the correct order of magnitude of the effective nonlinearity within the transmission band and the switching intensity for optical bistability within the stopband. The trend that this switching intensity decreases as the frequency increases across the stopband is also reproduced. Although it seems surprising that a simple one-dimensional model works when three-dimensional scattering of light plays an important rule, detail considerations suggest this simplification should be appropriate under the experimental condition.

In conclusion, we have established with a simple one dimensional model that the light-lattice coupling via electric gradient force underlies the large optical nonlinearity observed recently in colloidal crystals. Such a coupling alone can produce bistability and multistability with switching threshold intensities and transmission characteristics in good agreement with experiment. Given the unique large nonlinear response, colloidal crystals may prove to be very useful for future studies of nonlinear effects in PBG materials in the optical regime.

Acknowledgments

Ames Laboratory is operated for the U.S. Department of Energy by Iowa State University under Contract No. W-7405-Eng-82. This work was supported by the director for Energy Research, Office of Basic Energy Sciences, and NATO Grant No. CRG 940647.

Bibliography

[1] For a recent review, see C. M. Soukoulis, ed., "Photonic Band Gap Materials," (Kluwer, Dordrecht, 1996).

[2] For an excellent introduction to the PBG field, see J. Joannopoulos, R. D. Meade and J. N. Winn, "Photonic Crystals," (Princeton University Press, Princeton, 1995).

[3] E. Yablonovitch, T. J. Gmitter, and K. M. Leung, Phys. Rev. Lett. **67**, 2295 (1991); E. Özbay et al., Phys. Rev. B **50**, 1945 (1994).

[4] E. Özbay, E. Michel, G. Tuttle, et al., Appl. Phys. Lett. **64**, 2059 (1994).

[5] E. Özbay, E. Michel, G. Tuttle, et al., Opt. Lett. **19**, 1155 (1994).

[6] J. Martorell and N. M. Lawandy, Phys. Rev. Lett. **66**, 887 (1991).

[7] C. J. Herbert and M. S. Malcuit, Opt. Lett. **18**, 1783 (1992).

[8] I. I. Tarhan and G. H. Watson, Phys. Rev. Lett. **76**, 315 (1996).

[9] A. Imhof, J. K. G. Dhont, Phys. Rev. Lett. **75**, 1662 (1995).

[10] M. Scalora, J. P. Dowling, C. M. Bowden, and M. J. Bloemer, Phys. Rev. Lett. **73**, 1368 (1994).

[11] For an fcc lattice of spheres of filling ratio f, with diameter d_1 and lattice constant α, the following relation is obeyed, $f=4\frac{(4\pi/3)(d_1/2)^3}{\alpha^3}$. The distance between the [111] planes in an fcc lattice is $R_0 = \alpha/\sqrt{3}$, and since d_1=120 nm, one easily gets that R_0=88.64/$f^{1/3}$ nm. So for f=6.9%, $R_0 \simeq$216 nm.

[12] The polystyrene layer is a mixture of polystyrene spheres with diameter d_1 and water. To better approximate the experimental system, it is appropriate to use an average index of refraction $\bar{n}_1$. The volume fraction f_1 of the spheres within the polystyrene layer is $f_1 = R_0 f/d_1$ = 12.4%. From $\bar{n}_1 = n_1 f_1 + n_2(1 - f_1)$, we determine $\bar{n}_1 \simeq$1.36.

[13] The attenuated transmission in Figs. 2 and 3 in Ref. 7 is due to absorptions in water which we neglect in this study.

[14] H. Winful, J. Marburger, and E. Garmire, Appl. Phys. Lett. **35**, 379 (1979).

[15] C. Martine De Sterke and J. Sipe, in *Progress in Optics*, Vol. 33, edited by E. Wolf, (Elsevier, Amsterdam, 1994).

[16] F. Delyon, Y. Levy, and B. Souillard, Phys. Rev. Lett. **57**, 2010 (1986).

[17] Yi Wan and C. M. Soukoulis, Phys. Rev. B **41**, 800 (1990).

[18] D. Henning, H. Gabriel, G. P. Tsironis, and M. Molina, Appl. Phys. Lett. **64**, 2934 (1994).

[19] C. L. Adler and N. M. Lawandy, Opt. Comm. **91**, 354 (1992).

[20] W. Chen and D. L. Mills, Phys. Rev. Lett. **58**, 160 (1987).

[21] Qiming Li, C. T. Chan, K. M. Ho, and C. M. Soukoulis, Phys. Rev. B **53**, 15577 (1996).

[22] E. Lidorikis, Qiming Li, and C. M. Soukoulis, Phys. Rev. B **54**, 10249 (1996)

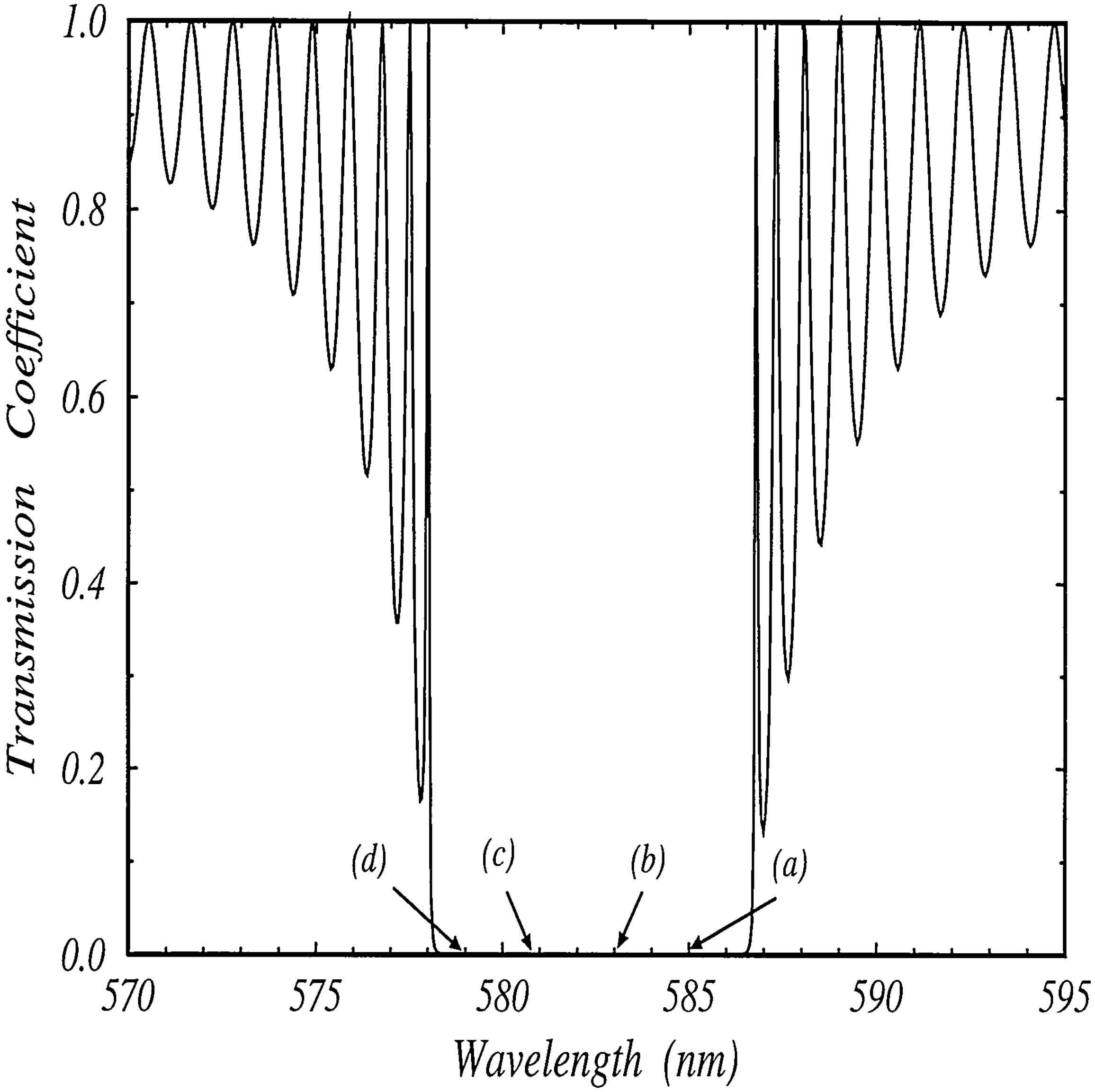

Figure 1 Transmission coefficient versus the wavelength in the [111] direction of a colloidal crystal. The width of the polystyrene sphere layer is d_1=120 nm, with an effective [12] index of refraction $\bar{n}_1 \simeq 1.36$, while the width of the water layer is d_2=96 nm with $n_2 = n_2^o = 1.33$. The number of bilayer units is N=463, which gives a sample thickness L=100μm. All the parameters used are in agreement with experiment. The arrows indicate the wavelengths of the incident light at which the transmission plots in Fig. 4 were obtained.

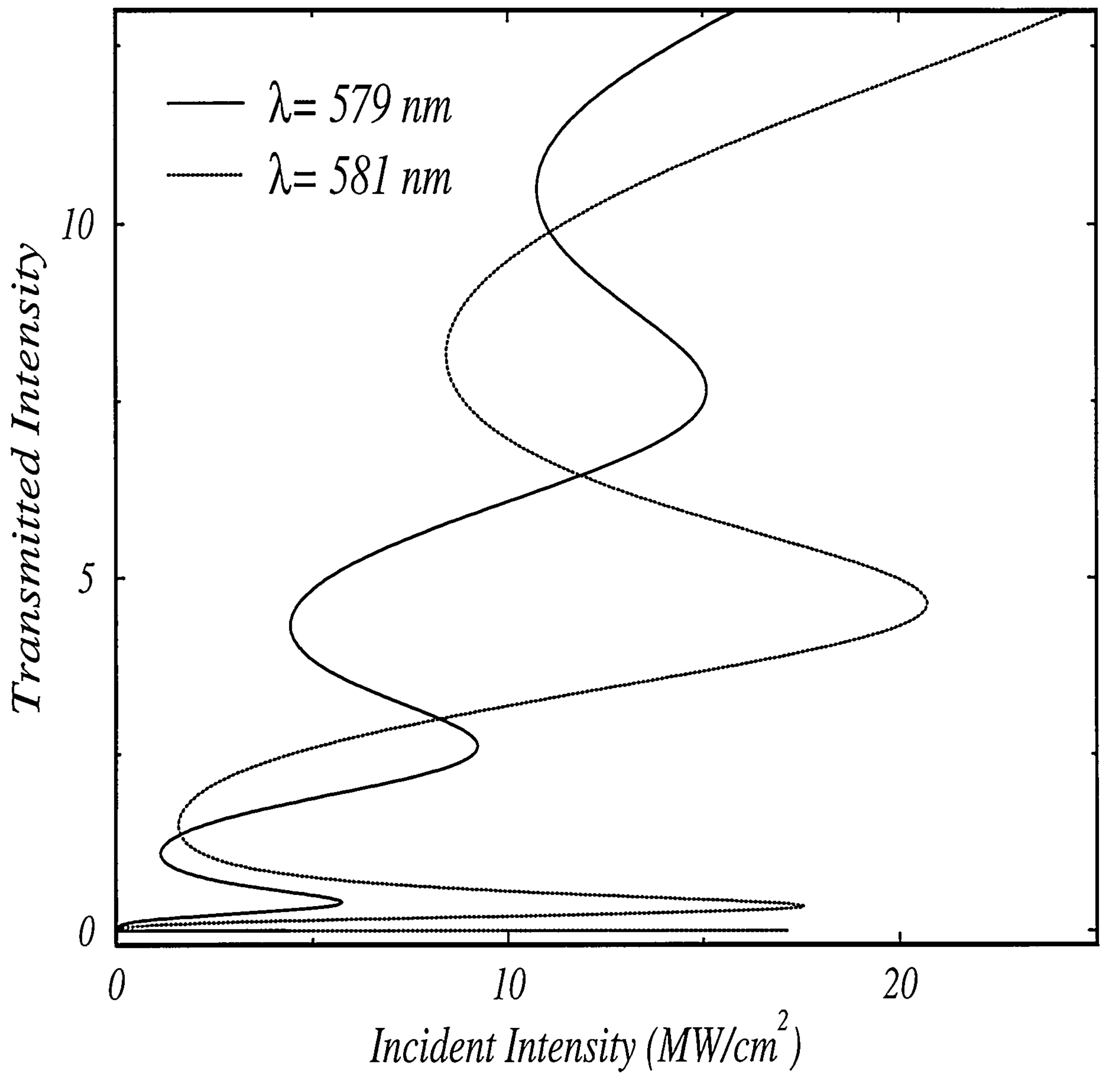

Figure 2 Transmitted intensity versus incident intensity for a simple nonlinear bilayer system with n′ = $4 \times 10^{-10}\mathrm{cm}^2/\mathrm{W}$ (in water) for two values of the incident wavelength. This model gives unrealistically high values for the threshold incident intensities.

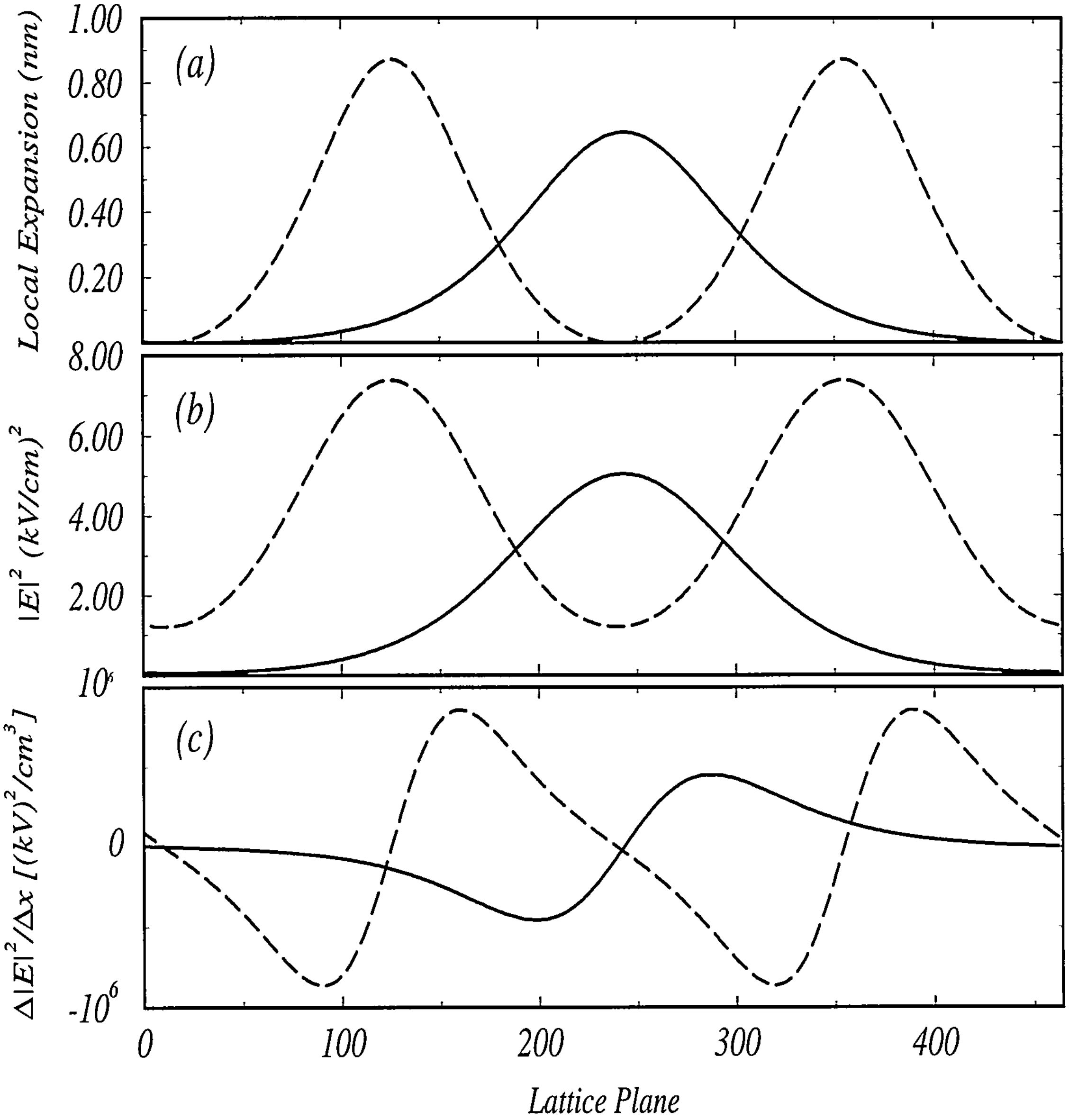

Figure 3 Local lattice expansion (a), Field intensity averaged in each sphere (b), and Field intensity gradient (c), as a function of the lattice plane for λ=579 nm. Solid and dashed curves correspond to the first and second transmission resonances.

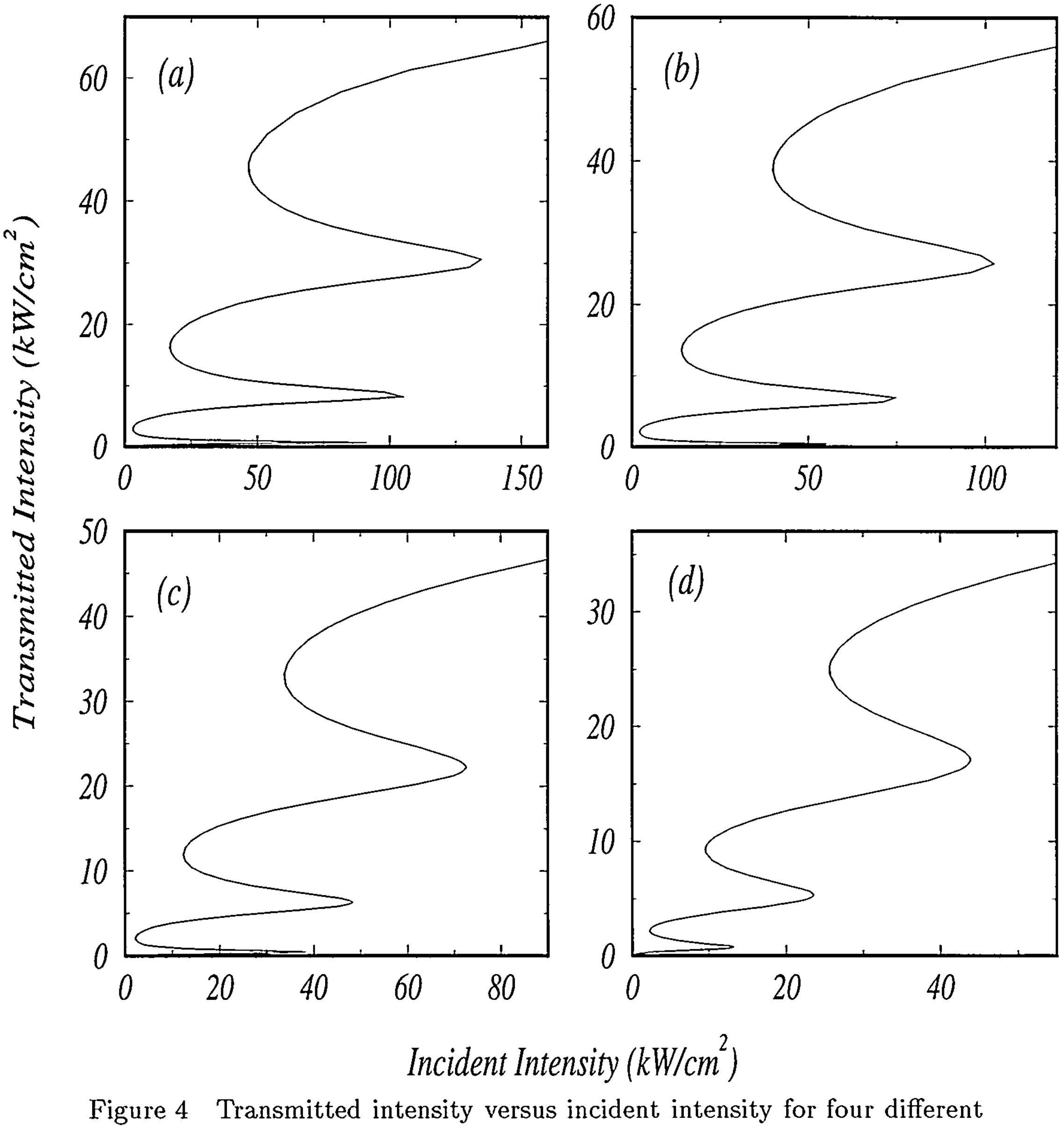

Figure 4 Transmitted intensity versus incident intensity for four different wavelengths as were indicated in Fig. 1.

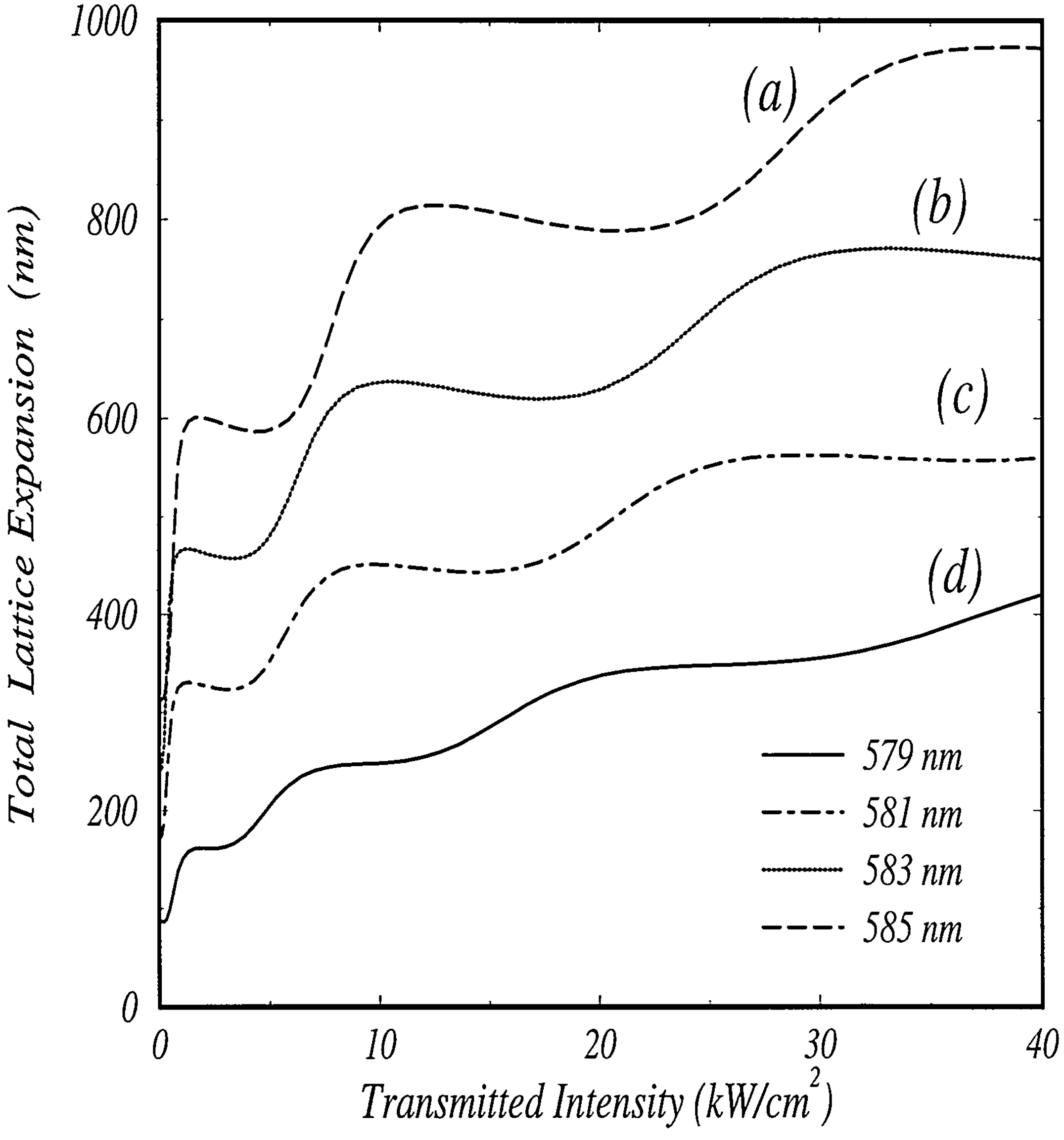

Figure 5 Total lattice expansion versus transmitted intensity for the four wavelengths indicated in Fig. 1. No external pressure is assumed.

CHAPTER 6. TIGHT-BINDING PARAMETERIZATION FOR PHOTONIC BAND GAP MATERIALS

A paper published in the journal of Physical Review Letters [1]

E. Lidorikis, M. M. Sigalas, E. N. Economou [2], and C. M. Soukoulis

Abstract

The idea of the linear combination of atomic orbitals (LCAO) method, well known from the study of electrons, is extended to the classical wave case. The Mie resonances of the isolated scatterer in the classical wave case, are analogous to the atomic orbitals in the electronic case. The matrix elements of the two-dimensional tight-binding (TB) Hamiltonian are obtained by fitting to *ab initio* results. The transferability of the TB model is tested by reproducing accurately the band structure of different 2D lattices, with and without defects, and at two different dielectric contrasts.

Introduction

In recent years experimental and theoretical studies of artificially manufactured periodic dielectric media called photonic band gap (PBG) materials or photonic crystals, have attracted considerable attention [1, 2]. PBG materials can have a profound impact in many areas in pure and applied physics. PBG materials are often considered as analogous to electronic semiconductors. The existence of spectral gaps in periodic PBG materials or localized states in

---

[1] PRL 81, 1405 (1998)

[2] Research Center of Crete, Greece

disordered systems, in analogy with what happens to the electronic materials, is of fundamental importance. Two different mechanisms, single scatterer resonances and macroscopic Bragg-like multiple scattering, contribute to the formation of gaps and localized states. Preliminary results [3, 4] have shown that there is a direct correspondence between the gaps calculated by plane wave expansion and the Mie resonances [5] of an isolated sphere. It is surprising that the positions of the Mie resonances approximately coincide with the center of the bands. It is tempting to suggest that the Mie resonances of an isolated scatterer play the role of the energy levels of an isolated atom in a crystal. This opens up the possibility to formulate the problem in a simpler way, similar to the tight-binding (TB) formulation of the electronic problem.

It is well known that the TB method has proven to be very useful in studying the electronic properties of solids [6, 7, 8, 9]. In an empirical TB approach, matrix elements of the Hamiltonian between orbitals centered on different sites are treated as parameters which are adjusted to obtain the band structure and the band gaps, which have been determined by other more accurate methods. The parameters obtained in this way are then used to study other properties of the systems, such as surface states, impurities and properties of disordered systems. The success of the TB formulation has been tested in the studies of all kinds of materials including Si, C and hydrogenated amorphous systems [7, 8, 9, 10].

In this paper, we show that it is possible to extend the ideas of the LCAO method to the classical wave case. The Mie resonances of the isolated scatterer in the classical case play the same role as the atomic orbitals in the electronic case. However, there exist two important differences. First, Mie resonances' states are not localized, in fact they decay too slowly, as $1/r$ as $r \to \infty$ and this may lead to divergences in some matrix elements. However, in a lattice environment they may be taken as localized, with a localization length comparable to the interparticle dimension. Second, in the classical wave case, as opposed to the electronic case, the host medium supports propagating solutions for every frequency. For large wavelengths, this is the dominant propagation mode since no resonances have been excited yet, while for wavelengths comparable to the particle dimension, transmission is achieved mainly through transfer between neighboring localized resonances. Thus, we may assume that the lowest frequency band is plane wave-like, while the higher bands are TB-like. This picture is more easily justified in the case of wide gaps and narrow bands, but its validity seems to be much wider. Within the framework of the systems we studied, we verified this picture. Furthermore, we were able to show that the TB matrix elements, after an appropriate rescaling, are functions of the distance only.

Formalism

We will consider the scalar case of a 2-D periodic array of N infinitely long dielectric cylinders in vacuum, with periodic boundary conditions and with the incident plane wave E-polarized. We assume the normalized electric field for each band to be given by

$$E_n(\vec{r},\vec{k}) = \frac{c_n^1(k)}{\sqrt{N}} e^{i\vec{k}\vec{r}} + \frac{c_n^2(k)}{\sqrt{N}} \sum_{\vec{R}} \Psi_n(\vec{r}-\vec{R}) e^{i\vec{k}\vec{R}} \tag{1}$$

where $n = 0, 1, 2, ...$ is the band's index and $\Psi_n(\vec{r}-\vec{R})$ with an angular symmetry $\Psi \sim \cos(n\theta)$ stands for the wavefunction of the n'th resonance localized at $\vec{R}$. $c_n^1 = 0$, $c_n^2 = 1$ for $n \neq 0$, and are functions of the frequency ($k \equiv |\vec{k}|$) only for $n = 0$ with $|c_0^1|^2 + |c_0^2|^2 = 1$. $\vec{r}$, $\vec{R}$, $\vec{k}$ are 2-D vectors, and we have assumed a unit area unit cell. In order to simplify the problem and make a better correspondence with the electronic case, we take the Ψ_n's to be orthonormal to each other and orthogonal to e^{ikr} so that $\int E_m^* E_n d\vec{r} = \delta_{mn}$. This will turn out to be a good approximation for our case. For the lowest frequency band, we should expect $c_0^1 \to 1$, $c_0^2 \to 0$ for $|\vec{k}| \to 0$ and $c_0^1 \to 0$, $c_0^2 \to 1$ for $|\vec{k}| \to |\vec{G}|/2$.

The "Hamiltonian" for the scalar wave equation is $H = -\vec{\nabla}^2/\epsilon(\vec{r})$ and the eigenfrequencies ω^2/c^2 of the system can be found by diagonalizing the Hamiltonian matrix $H_{mn} = \int E_m^* H E_n d\vec{r}$. For a square lattice with lattice constant a, using the standard notation [6, 7, 8] and taking up to second nearest neighbors into account, the H_{00} matrix element will be:

$$H_{00} = |c_0^1|^2 |k|^2/\langle\epsilon\rangle + |c_0^2|^2 [\varepsilon_s + 2V_{ss\sigma}^{(1)}(\cos\phi_x + \cos\phi_y) + 4V_{ss\sigma}^{(2)} \cos\phi_x \cos\phi_y] \tag{2}$$

where $\phi_x = k_x a$, $\phi_y = k_y a$, $|k| = \sqrt{k_x^2 + k_y^2}$, $\langle\epsilon\rangle$ is the average dielectric constant, $\varepsilon_s = \int \Psi_0^*(\vec{r}) H \Psi_0(\vec{r}) d\vec{r}$ and $V_{ss\sigma}^{(1),(2)} = \int \Psi_0^*(\vec{r}) H \Psi_0(\vec{r}-\vec{R}^{(1),(2)}) d\vec{r}$; the superscripts (1) and (2) stand for first and second neighbors. We argue that the functional form of $|c_0^2(k)|^2$ is similar to the form of the scattering cross section of a single cylinder [5] for the $n = 0$ (or s-wave) case, so that $|c_0^1(k)|^2 \simeq e^{-\lambda(f)\omega_r^{\mu}}$. Here $\omega_r = |\vec{k}|c/(\omega_0\sqrt{\langle\epsilon\rangle})$, ω_0 is the single cylinder Mie resonance frequency, $\lambda(f)$ is a function of the filling ratio f of the form $\lambda(f) = h_1/f^{h_2}$. The exponent μ has to be larger than 2 in order to preserve the correct slope at $|\vec{k}| \to 0$. For simplicity, we choose $\mu = 4$.

The second band ($n = 1$ or p-like) has a $\Psi \sim \cos\theta$ symmetry, and will consist of two linearly independent polarizations, p_x and p_y. The Hamiltonian matrix elements are:

$$\begin{aligned} H_{p_xp_x} &= \varepsilon_{p_x} + 2V^{(1)}_{pp\pi}\cos\phi_y + 2V^{(1)}_{pp\sigma}\cos\phi_x + 2\left(V^{(2)}_{pp\sigma} + V^{(2)}_{pp\pi}\right)\cos\phi_x\cos\phi_y \qquad (3) \\ H_{p_xp_y} &= 2\left(V^{(2)}_{pp\pi} - V^{(2)}_{pp\sigma}\right)\sin\phi_x\sin\phi_y \qquad (4) \end{aligned}$$

where all quantities are defined the same way as in Eq. (2). The matrix element $H_{p_yp_y}$ is similar to $H_{p_xp_x}$ with $x \longleftrightarrow y$; $H_{p_yp_x} = H^*_{p_xp_y}$. In this work we consider only these two bands. We take also the dielectric constant of the cylinders to be $\epsilon = 100$. This large value of ϵ ensures that the matrix element H_{sp} is negligible. However, even smaller values of ϵ (*e.g.* $\epsilon = 13$) seem to give $H_{sp} \simeq 0$.

Results and discussion

We have fitted the V and ε matrix elements, as well as the value of λ, to the band structure of five different rectangular lattices with large/small axis ratios: 1, 1.05, 1.1, 1.15, 1.2 as well as to a hexagonal lattice, for six different filling ratios: $f = .1 - .6$. Taking into account up to third nearest neighbors for the rectangular lattice involves 13 (9 V's, 3 ε's and the value of λ) adjustable parameters, while for the hexagonal we considered only first nearest neighbors and so used only 6 adjustable parameters. The quality of these fits can be seen in Fig. 1 where we plot the bands as found numerically by the plane wave expansion (PWE) method along with the TB fit, for a square and a hexagonal lattice for two filling ratios. The excellent fit is an indication of the potential usefulness of the TB method.

We plot next some of the fitted matrix elements. The square root of the diagonal ε_{p_x}

and ε_{p_y} matrix elements are plotted (Fig. 2a) as a function of the filling ratio f, while the off diagonal $V_{pp\pi}$ matrix elements are plotted (Fig. 2c) as a function of the dimensionless separation distance $d_{ij} = r_{ij}/\alpha$, where r_{ij} is the separation distance between cylinders i and j and α is the cylinders' radius. Obviously the matrix elements, especially $V_{pp\pi}$, do not depend on a single parameter (*e.g.* d_{ij}). Apparently the lattice environment [10] has to be included, hopefully through rescaling functions.

The proposed simple rescaling function $(D_n^{on})_i$ for the diagonal matrix elements of cylinder i, that takes into account the filling ratio and the different symmetries is of the form:

$$\frac{1}{(D_n^{on})_i} = \sum_{j \neq i} \frac{\tau \cos^2(n\theta_{ij})}{d_{ij}^{\nu_n}} \tag{5}$$

where θ_{ij} is the angle between the symmetry axis of the p resonance on cylinder i and the $\hat{r}_{ij}$ direction, n=0,1,.. for the s,p,.. resonances, and the sum runs over the nearest neighbors of cylinder i. The power on the angular function was chosen so that the p_x and p_y resonances in the hexagonal lattice to be the same. The only choices were 2 and 4, and it was found that 2 gives better results. Eq. 5 is similar to what was used in Ref. [10] for the atomic orbitals, except for two differences: (a) here we take into account the resonance's angular symmetry, and (b) the exponentially decaying part is missing, reflecting the non-localized character of the EM resonances. Finally, $\tau = \left[\pi\alpha^2/(a^2 f)\right]^2$ takes into account that different structures, with the same a and α, have different filling ratios. $\tau = 1$ for the rectangular structures and $\tau = 3/4$ for the hexagonal. We will use this parameter only for the diagonal matrix elements.

For the periodic case, the function $(D_n^{on})_i$ is the same for every i. We find that the diagonal matrix element depends on $(D_n^{on})_i$ as follows: $\sqrt{\varepsilon_n} = a_0^n + a_1^n (D_n^{on})^{-a_2^n} + a_3^n (D_n^{on})^{-a_4^n}$ where $a_0^n = \omega_0 \alpha / c$ is the corresponding dimensionless Mie resonance frequency and the a_j^n's ($j = 1, ..., 4$) are constants. In Fig. 2b we plot $\sqrt{\varepsilon_p}$ *vs* the environment function $(1/D_p^{on})$. We can see that $\sqrt{\varepsilon_p}$ now scales very well, having a larger value for increasing lattice density. The same dependence is found for all bands.

In order to rescale the off diagonal V matrix element between two neighboring resonances i and j, we need contributions from the neighbors that are close to the line joining i and j. Contributions have to be projected on the $\hat{r}_{ij}$ direction for the s resonance, while for the p

resonance we have to project on its symmetry axis. Only first nearest neighbors will contribute. At the end, we have to normalize with the sum of all projection weights.

A simple formula that describes the environment of the n resonance on cylinder i, along the $\hat{r}_{ij}$ direction is:

$$\frac{1}{(D_n^{off})_{ij}} = \frac{\sum_l (\cos^2 \theta_{ilj}^n / d_{il}^{\nu_n})}{\sum_l \cos^2 \theta_{ilj}^n} \tag{6}$$

where l runs over i's nearest neighbors (including j). θ_{ilj}^n is the angle between the $\hat{r}_{il}$ and $\hat{r}_{ij}$ directions for the s resonance ($n = 0$), and for the p resonance ($n = 1$), it is the angle between the i'th resonance's symmetry axis and the $\hat{r}_{il}$ direction . Both angles are taken to have a range from $-\pi/2$ to $\pi/2$ [11]. Finally, if we include screening in our considerations, then the actual matrix element V to be used in a particular problem, can be obtained by the fully rescaled one $\mathcal{V}$, by $V^{ij} = \mathcal{V}^{ij}(1 - S^{ij})/[(D^{off})_{ij}^{-1} + (D^{off})_{ji}^{-1}]$ where S^{ij} is the same screening function used in Ref. [10]: $S^{ij} = \tanh\left(b_1 \sum_{l \neq i,j} e^{-b_2[(d_{il}+d_{jl})/d_{ij}]^{b_3}}\right)$, and is different for different matrix elements. The fully rescaled matrix elements are found to scale with separation distance as $\mathcal{V}^{ij} = c_1 d_{ij}^{-c_2} + c_3 d_{ij}^{-c_4}$ where $c_1, ..., c_4$ are constants. In Fig. 2d we plot the rescaled $\mathcal{V}_{pp\pi}$ matrix element. We see now that it is a smooth function of separation distance, except for the second nearest matrix elements which do not scale very well for large filling ratios (small distances). Apparently an improved screening function that depends on the filling ratio as well is needed.

The constants in the expressions for the ε's and the $\mathcal{V}$'s are given in tables I and II. We have also found $\nu_n = 1.65$ for all n, and $h_1 = .068$, $h_2 = 1.23$ for $\lambda(f)$.

TABLE I. The parameters for the ε elements.

	a_0	a_1	a_2	a_3	a_4
$\sqrt{\varepsilon_s}$	0.0804	0.0460	0.716	-0.0121	5.000
$\sqrt{\varepsilon_p}$	0.2371	0.0890	1.640	0.0020	0.320

TABLE II. The parameters for the V elements.

	b_1	b_2	b_3	c_1	c_2	c_3	c_4
$V_{ss\sigma}$	0.075	0.0008	10.0	-0.108	4.00	-0.00096	1.30
$V_{pp\sigma}$	0.100	0.00008	13.5	0.425	6.14	0.0550	3.22
$V_{pp\pi}$	0.700	0.0015	10.0	-0.076	5.40	-0.0044	2.32

To check the transferability of our results we study first the defect case shown in the insert graph of Fig. 3a. There the central cylinder of a 3 × 3 supercell is displaced as shown. For $\vec{k}a = (0, 1/3)$ we plot in Fig. 3a the three edge eigenfrequencies of the first two bands, and directly compare our results with the ones obtained numerically by the PWE method for exactly the same system. The agreement is excellent. Thus our TB parameterization works very well for the defect case too. It is worth noting that the PWE method takes a factor of 10^4 more CPU time than the TB method.

The second test checks the transferability of our parameters for different dielectric contrasts. We fitted the TB parameters for a square lattice of $\epsilon = 13$ for 5 different filling ratios. The quality of the fit can be seen in Fig. 3b where we plot the PWE bands along with the TB fit for the $f = 20\%$ case. We find that the matrix elements are rescaled by the same functions with the same parameters except only for a different power ν, and scale with distance with the same c parameters as obtained from Table II, except for a multiplication constant. In the $\epsilon = 13$ case, we find that $\nu = 4.37$ and the multiplicative constants are $c = 3.88$ for $\mathcal{V}_{pp\sigma}$ and $c = 4.46$ for $\mathcal{V}_{pp\pi}$. A larger rescaling power ν can be easily understood since less contrast produces less localized resonances and so the environmental effect will be larger. The rescaled $\mathcal{V}_{pp\sigma}$ and $\mathcal{V}_{pp\pi}$ are ploted in Fig.'s 3c1 and 3c2. We see that our TB parameters are transferable to other, more realistic dielectric contrasts, with minor changes.

Conclusions and acknowledgments

In conclusion, we have obtained a successful TB formulation of light propagation in 2D PBG structures with transferable matrix elements. Thus we provide an efficient scheme for handling not only periodic systems but defects and disordered cases as well. Hopefully this scheme can be extended to 3D structures as well.

We would like to thank C. Z. Wang and K. M. Ho for useful discussions. Ames Laboratory is operated for the U.S. Department of Energy by Iowa State University under Contract No. W-7405-Eng-82. This work was supported by the Director for Energy Research office of Basic Energy Sciences and Advanced Energy Projects, by NATO Grant No. 940647, by a ΠΕΝΕΔ grant and by an EU grant.

Bibliography

[1] a) See for example, *Photonic Band Gaps and Localization*, edited by C. M. Soukoulis (Plenum, New York, 1993); b) J. Opt. Soc. Am. B **10**, 208-408 (1993); c) *Photonic Band Gap Materials*, edited by C. M. Soukoulis (Kluwer, Dordrecht, 1996).

[2] J. Joannopoulos, R. D. Meade and J. Winn, *Photonic Crystals*, (Princeton University, Princeton, N. J. 1995).

[3] S. Datta, C. T. Chan, K. M. Ho, C. M. Soukoulis and E. N. Economou in Ref. 1a p. 289.

[4] M. Kafesaki, E. N. Economou and M. M. Sigalas in Ref. 1c p. 143.

[5] G. Mie, Ann. Phys. **25**, 377 (1908); C. F. Bohren and D. R. Huffman, *Absorption and Scattering of Light by Small Particles* (J. Wiley, New York, 1983, ch. 4).

[6] J. C. Slater and G. F. Koster, Phys. Rev. **94**, 1498 (1954).

[7] D. A. Papaconstantopoulos, *Handbook of the Electronic Structure of Elemental Solids*, (Plenum Press, New York, 1986).

[8] W. A. Harrison, *Electronic Structure and the Properties of Solids*, (Freeman, San Francisco, 1980).

[9] G. C. Fletcher, *The Electron Band Theory of Solids*, (North-Holland Publishing Company, London, 1971).

[10] M. S. Tang, C. Z. Wang, C. T. Chan, and K. M. Ho, Phys. Rev. B **53**, 979 (1996).

[11] Note however, that for $V_{pp\pi}$ matrix elements, since both lobes of the p resonance are involved, θ^1_{ilj} must take all possible values, but we will have to average over the contributions to each lobe. Also note, that for the non-periodic case, certain $H_{p_xp_y}$ and $H_{p_yp_x}$ matrix elements will not be complex conjugates if the formula is applied explicitly. In this event we have to average over the two possibilities, in order to keep the Hamiltonian matrix Hermitian.

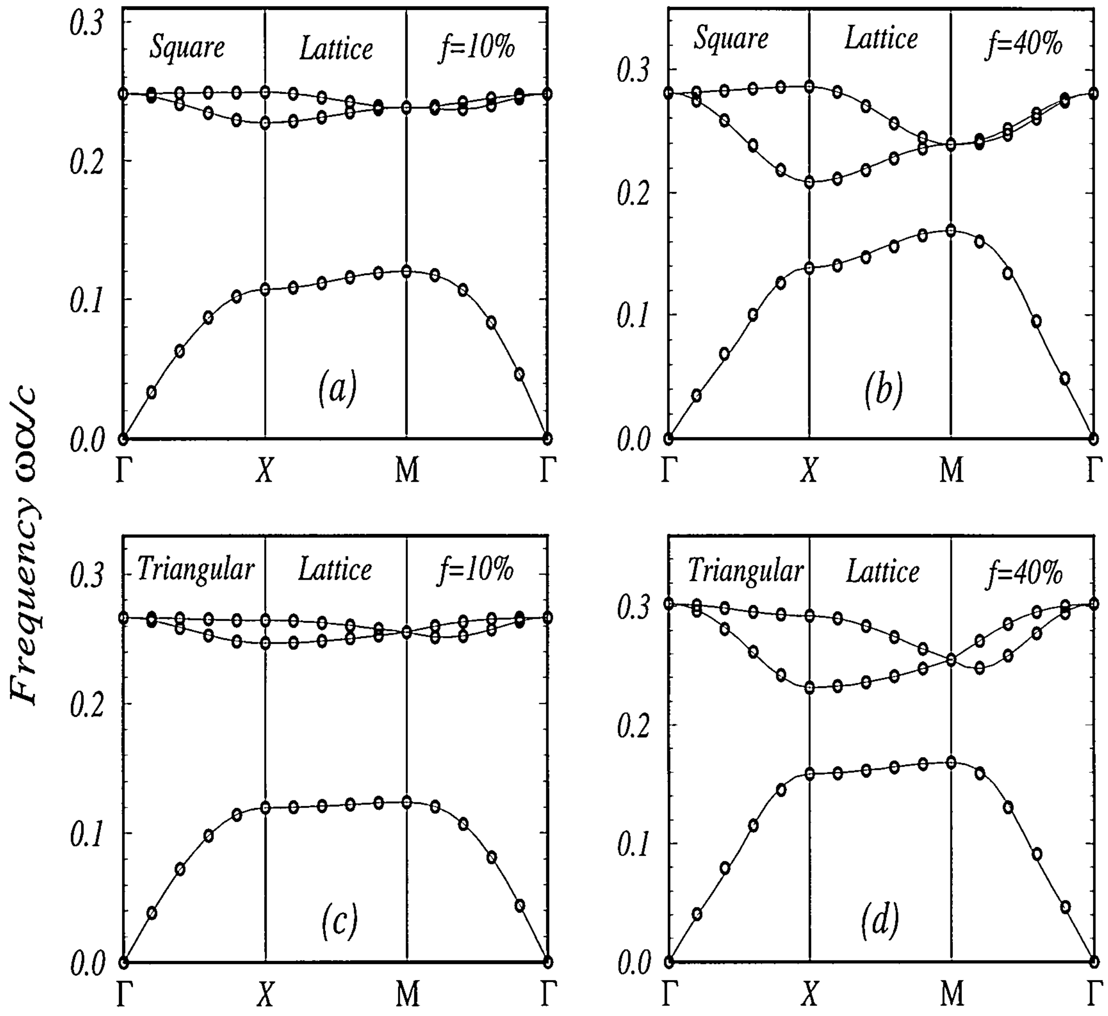

Figure 1 The first two frequency bands for a square lattice with filling ratio $f = .1$ (a) and $f = .4$ (b), and for a hexagonal lattice with $f = .1$ (c) and $f = .4$ (d). Circles correspond to numerical results from the PWE method, while solid lines correspond to the TB fit.

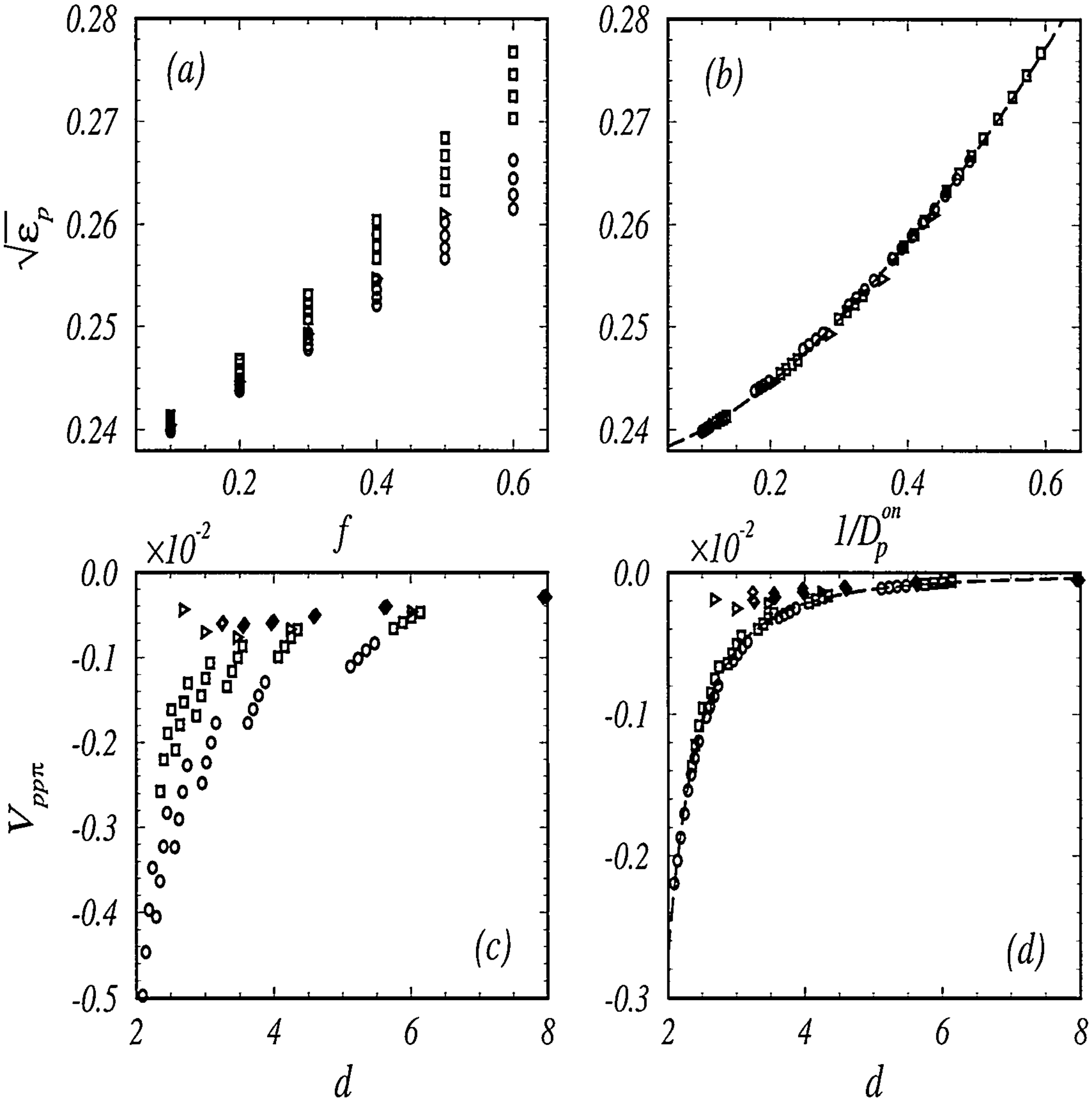

Figure 2 Fitted TB parameters for the second (p-like) frequency band. (a) $\sqrt{\varepsilon_p}$ *vs* f. (b) $\sqrt{\varepsilon_p}$ *vs* the rescaled environment function $1/D_p^{on}$. Circles and squares correspond to $\sqrt{\varepsilon_{p_x}}$ and $\sqrt{\varepsilon_{p_y}}$ respectively of a rectangular lattice with the big axis along $\hat{x}$, and triangles to a hexagonal lattice. (c) $V_{pp\pi}$ *vs* the dimensionless separation d. (d) The rescaled $\mathcal{V}_{pp\pi}$ *vs* d. Circles, squares and diamonds correspond to a rectangular lattice's $V_{pp\pi}$ elements along the small axis, the large axis and the diagonal, and triangles to a hexagonal lattice. All matrix elements are expressed in the dimensionless units of $(\omega\alpha/c)^2$.

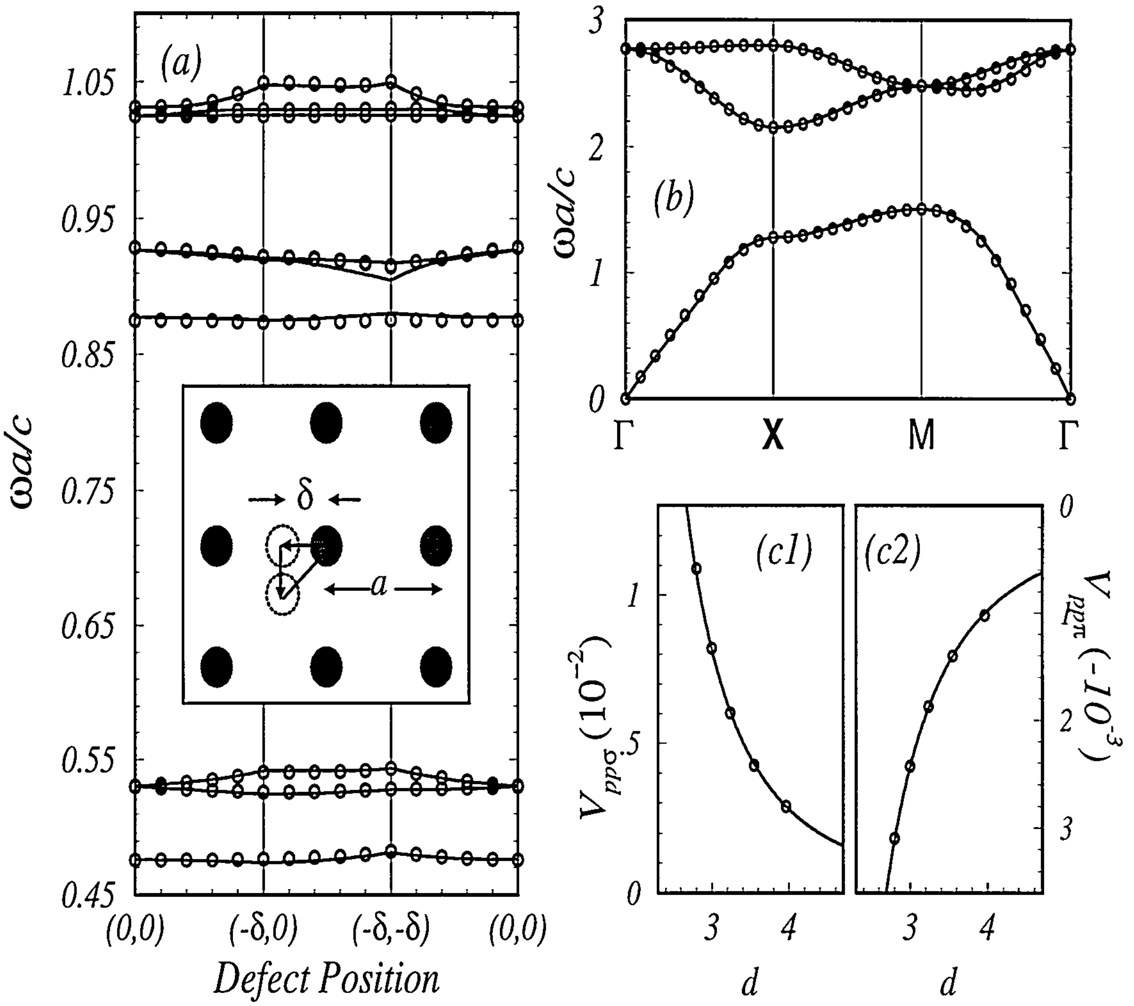

Figure 3 a) The three edge eigenfrequencies (circles for PWE, solid line for TB) for each band for a 3 × 3 supercell including a defect with $f = 20\%$. All cylinders are identical, w ith the midlle one moving from the equilibrium position, as pointed in the insert graph with $\delta = a/4$. The wave vector is always constant $\vec{k}a = (0, 1/3)$. The first band gap extends approximately from $\omega a/c \simeq .53$ to $\omega a/c \simeq .87$, while the second starts at $\omega a/c \simeq 1.03$. b) PWE bands (circles) along with the TB fit (solid line) for $\epsilon = 13$ and $f = 20\%$. c) The fully rescaled $V_{pp\sigma}$ (circles in c1) and $V_{pp\pi}$ (circles in c2) for the system in b) *vs* the dimensionless separation d. The solid line is the fit using the parameters from Table II and a multiplicative constant.

CHAPTER 7. GAP DEFORMATION AND CLASSICAL WAVE LOCALIZATION IN DISORDERED TWO-DIMENSIONAL PHOTONIC BAND GAP MATERIALS

A paper to be submitted for publication in the journal of Physical Review B

E. Lidorikis, M. M. Sigalas, E. N. Economou [1], and C. M. Soukoulis

Abstract

By using two *ab initio* numerical methods we study the effects that disorder has on the spectral gaps and on wave localization in two-dimensional photonic band gap materials. We find that there are basically two different responses depending on the lattice realization (solid dielectric cylinders in air or *vise versa*), the wave polarization, and the particular form under which disorder is introduced. Two different pictures for the photonic states are employed, the "nearly free" photon and the "strongly localized" photon. These originate from the two different mechanisms responsible for the formation of the spectral gaps, ie. multiple scattering and single scatterer resonances, and they qualitatively explain our results.

Introduction

Electromagnetic waves traveling in periodic dielectric structures will undergo multiple scattering. For the proper structural parameters and wave frequencies, all waves may backscatter coherently; the result is total inhibition of propagation inside the structure. Such structures

---

[1] Research Center of Crete, Greece

are called photonic band gap (PBG) materials [1, 2] or photonic crystals, and the corresponding frequency ranges, for which propagation is not allowed, photonic band gaps or stop bands. PBG materials can be artificially made in one, two, or three dimensions. For example, a periodic lattice of dielectric spheres embedded in a different dielectric medium would work as a three-dimensional PBG material, for the proper choice of lattice symmetry, dielectric contrast, and sphere volume filling ratio. In two dimensions, a periodic array of parallel, infinitely long, dielectric cylinders could work as a two-dimensional PBG material, prohibiting propagation in a direction perpendicular to the cylinders' axis for some frequency range(s). The absence of optical modes in a photonic band gap is often considered as analogous to the absence of electronic energy eigenstates in the semiconductor energy gap. The ability of PBG materials to modulate electromagnetic wave propagation, in a similar way semiconductors modulate the electric current flow, can have a profound impact in many areas in pure and applied physics. It is then of fundamental importance to study the effects of disorder [3, 4] on the transmission properties of such materials.

Besides the non-resonant, macroscopic Bragg-like multiple scattering, there is also a second, resonant mechanism, that contributes to the formation of the spectral gaps. This is [5, 6, 7] the excitation of single scatterer Mie resonances [8]. In a previous publication [7] it was shown that for two-dimensional PBG materials, for the E polarization scalar wave case (electric field parallel to the cylinders' axis), these Mie resonances are analogous to the electronic orbitals in semiconductors. The idea of the linear combination of atomic orbitals (LCAO) method was extended to the classical wave case as a linear combination of Mie resonances (LCMR), leading to a successful tight-binding (TB) parameterization for photonic band gap materials. This moves the picture for the photon states, from a one analogous to the nearly free electron model, to the one analogous to the strongly localized electron whose transport is achieved only by hopping (tunneling) from atom to atom. Depending then on which mechanism is dominant for the formation of the photonic gaps, we expect different changes to the system's properties when disorder is introduced. If the Bragg-like multiple scattering mechanism is the dominant one, the photonic gaps should close quickly with increasing disorder, while if it is the excitation of Mie resonances, the photonic gaps should survive large amounts of disorder, in a similar way the electronic energy gap survives in amorphous silicon.

In this paper we will use two *ab initio* numerical methods to study the effects of disorder on photonic gap formation and wave localization in two-dimensional PBG materials. The first is the finite difference time domain (FDTD) spectral method [9, 10], from which we obtain the photonic density of states for an infinite, disordered PBG material, and the second is the transfer matrix technique [11], from which we obtain the transmission coefficient for a wave incident onto a finite slab of the disordered PBG material. From the transmission coefficient we can obtain the localization length for the photonic states of the disordered material [4]. The study will be on both PBG material realizations (solid high dielectric cylinders in air and cylindrical air holes in high dielectric), for both wave polarizations, and it will incorporate three different disorder realizations: disorder in position, radius, and dielectric constant (these systems, though, will still be periodic on the average). We will find that only the case of solid dielectric cylinders in air with the wave E_z-polarized exhibits the behavior expected from the strongly localized photon picture, while for all other cases, the nearly free photon picture seems to be the dominant one.

Numerical methods

Electromagnetic wave propagation in lossless composite dielectric media is described by Maxwell's equations

$$\mu\frac{\partial\vec{H}}{\partial t} = -\vec{\nabla}\times\vec{E}, \qquad \epsilon(\vec{r})\frac{\partial\vec{E}}{\partial t} = \vec{\nabla}\times\vec{H}, \tag{1}$$

where the dielectric constant $\epsilon(\vec{r})$ is a function of position. In two dimensions, the two independent wave polarizations are decoupled. We assume the variation of the dielectric constant, as well as the propagation direction, along the xy plane, and so, the cylinders along the z axis. One of the polarizations is with the electric field parallel to the z axis and the magnetic field on the xy plane (E_z or TM polarized) and obeys a scalar wave equation. The other one with the magnetic field parallel to the z axis and the electric field on the xy plane (H_z or TE polarized) and obeys a vector wave equation.

The first method we will use, to study disordered PBG materials, is the FDTD spectral method [12, 13]. In our FDTD scheme, we first discretize the xy plane into a fine uniform grid. Each grid point is centered in a unit cell which is further discretized into a 10×10 subgrid, on which an arithmetic average of the dielectric constant is performed. In our problem we will assume dispersionless and lossless materials. For the E_z polarization case we define the electric field on this grid and the magnetic field on two additional grids, one tilted by $(d/2, 0)$, on which H_y is defined, and one tilted by $(0, d/2)$, on which we define H_x. d is the side of the grid cell. The corresponding finite-difference equations for the space derivatives that are used in the curl operators are then central-difference in nature and second-order accurate. The electric and magnetic fields are also displaced in time by a half time step $\Delta t/2$, resulting in a "leapfrog" arrangement and central-difference equations for the time derivatives as well. If one initialize the electric and magnetic fields at $t = t_0$ and $t = t_0 + \Delta t/2$ respectively, then updating the values of the electric field for each grid point (i, j) at $t = t_0 + \Delta t$ is done by

$$\begin{aligned} E_z|_{i,j}^{t_0+\Delta t} = E_z|_{i,j}^{t_0} \quad &+ \quad \frac{\Delta t}{d\ \epsilon_{i,j}}(H_y|_{i+1/2,j}^{t_0+\Delta t/2} - H_y|_{i-1/2,j}^{t_0+\Delta t/2} - \\ &- \quad H_x|_{i,j+1/2}^{t_0+\Delta t/2} + H_x|_{i,j-1/2}^{t_0+\Delta t/2}) \end{aligned} \tag{2}$$

where $\epsilon_{i,j}$ is the averaged dielectric constant for the grid point (i, j). Similar equations follow for updating the magnetic field components at $t = t_0 + 3\Delta t/2$, then again Eq. (2) for E_z at $t = t_0 + 2\Delta t$ etc. This way the time evolution of the system can be recorded. For numerical stability and good convergence the number of grid points per wavelength λ/d must be at least 20, and also $\Delta t \leq d/\sqrt{2}c$, where c the speed of light in vacuum. Similar equations, with the roles of the electric and magnetic fields interchanged, apply for the H_z polarization case.

In order to find the eigenmodes of a particular periodic (or disordered) system, we first initialize the electric and magnetic fields in the unit cell (or a suitable supercell) using periodic boundary conditions: $\vec{E}(\vec{r}+\vec{a}) = e^{i\vec{k}\vec{a}}\vec{E}(\vec{r})$ and similarly for $\vec{H}(\vec{r})$, where $\vec{k}$ is the corresponding Bloch wave vector and $\vec{a}$ the lattice vector. These fields must have nonzero projections with the modes in search. We choose a superposition of Bloch waves for the magnetic field and set zero the electric field:

$$\vec{H}(\vec{r}) = \sum_{\vec{g}} \hat{v}_{\vec{g}} e^{i(\vec{k}+\vec{g})\vec{r}+i\phi_{\vec{g}}}, \qquad \vec{E}(\vec{r}) = 0, \tag{3}$$

where $\phi_{\vec{g}}$ is just a random phase and the unit vector $\hat{v}$ is perpendicular to both $\vec{E}$ and $(\vec{k}+\vec{g})$, ensuring that $\vec{H}$ is transverse and that $\vec{\nabla}\vec{H} = 0$. Once the initial fields are defined, we can evolve them in time using the "leapfrog" difference equations, while recording the field values as a time series for some sampling points. As the electric fields "builds" up, some particular modes dominate while most are depressed, reflecting the underline lattice symmetries. Here we record only the E_z field for the E_z polarization case, and the H_z field for the H_z polarization. At the end of the simulation, the time series are Fourier transformed back into frequency space, and the eigenmodes $\omega(\vec{k})$ of the system appear as sharp peaks. The length of the simulation determines the frequency resolution while the time difference between successive recordings determines the maximum frequency considered. This method scales linearly with size: a larger system will still need the same number of time steps for the same frequency resolution, thus sometimes referred to also as an "order-N" method [12].

Here we will use this method to obtain the system's density of states (DOS). If one chooses a large supercell instead of the unit cell, then for each $\vec{k}$ point inside it's first Brillouin zone, the Fourier transformed time series will consist of a number of peaks. Adding all contributions from all $\vec{k}$'s will result to a smooth function for the DOS. This is in contrast to older methods that where using random fields as initial boundary conditions [4]. Random initial fields will ensure the condition for nonzero projections to all of the system's eigenmodes, but in order to get coupled with them during "built" up, a large simulation time is required. Furthermore, the produced DOS is not a smooth function of frequency, still consisting of a large collection of peaks, and thus being useful only as an indication for the existence of spectral gaps. In our method, the underline symmetries of the modes are already in the initial fields and so they couple easier with them. Also, the larger the supercell, the smaller is its first Brillouin zone, and so the smaller the frequencies we initialize through the various $\vec{k}$. This is why we can get smooth results even for very low frequencies. In Figs. 1 and 2, we show the calculated density of states for the case of solid dielectric cylinders in air and cylindrical air holes in dielectric respectively, both for a square lattice arrangement, and for both polarizations. Along with them we also plot the corresponding band structure as obtained with the plane wave expansion method. Our study is going to be based on these two photonic structures.

The second method we will use is the transfer matrix technique in order to obtain the transmission coefficient for a wave incident along the xy plane on a slab (or a slice) of the photonic material. The slice is assumed uniform along the z axis, and periodic along the x direction through application of periodic boundary conditions, while in the y direction it has a finite width L. In this method one first constructs the transmitted waves at one side of the slice and then integrates numerically the time-independent Maxwell's equations to the other side. There, the waves are projected into incident and reflected waves, and so a value for the transmission coefficient T can be obtained. Here, we are interested in the wave localization in disordered photonic band gap materials, and in particularly in the localization length $\ell \sim -2L/\ln T$.

A few remarks about the results of this method are in order. Waves with different incidence directions will have different reflection and transmission coefficients, so if one is looking for an average transmission, all directions should be included. It is shown, however, that there is also a large dependence on the surface plane along which the structure is cut. More specifically, a wave normally incident on a (1,0) surface will have different transmission characteristics than a wave incident with 45^o on a (1,1) surface. This is because certain modes can not always get coupled with the incident wave. One should then also average for the two different surface cuts, otherwise it will not be a true average. This is shown in Figs. 3 and 4 where we plot the (1,0) and the (1,1) cuts, each with both incidence directions (normal and 45^o with respect to the surface) averaged. We see that taken individually, none of them corresponds to the true gaps as shown in Figs. 1 and 2, but rather, to wider and generally displaced gaps. For example, in the E_z polarization case in the first spectral gap (Figs. 3a and 4a), with the (1,0) cut, the incident waves fail to couple with the the M modes of the first band, while with the (1,1) cut, the incident waves fail to couple with the X modes of the second band.

This is expected to be lifted once disorder is introduced into our system, since the sense of direction will be somehow lost. Disorder can be introduced as a random displacement, a random change in the radius, or, a random change in the dielectric constant of the cylinders. It is not clear however what amount of disorder would be needed for this. We repeated the calculations for small enough amounts of disorder so that the spectral gaps, as found from the FDTD method, remain almost unchanged, for all three different disorder mechanisms. As seen in Figs. 3 and 4, indeed, in some cases the coupling is achieved. For example, for the first gap in the E_z-polarization case, with the (1,0) cut, the M modes of the first band are now coupled with the incident waves and appear in the transmission diagram. These could be easily mistaken for disorder-induced localized states entering the gap, but they are not, since for the values of disorder used, the first gap is virtually unchanged. On the other hand, with the (1,1) cut, the coupling to X modes of the second band is not yet achieved, still yielding a wrong picture for the gap. Increasing the disorder further will eventually destroy any sense of direction and there will be no distinction between the two cases. Figs. 3 and 4 will be useful as a guide of which results can be trusted and which can not, if one uses only one surface cut and small values of disorder. As a general rule, we can deduce that the (1,0) cut should be used for the E_z polarization case, while the (1,1) cut would be better for the H_z polarization case.

Results and discussion

We first looked into the spectral gaps' dependence on disorder using the FDTD spectral method. Our system consisted of a 8×8 supercell, each cell discretized into a 32×32 grid. We studied two systems: a square lattice array of solid cylinders, with dielectric constant ϵ_a=10, in air (ϵ_b=1) with a filling ratio f=0.28%, and a square lattice array of air cylinders (ϵ_a=1) in dielectric material ϵ_b=10, with air filling ratio f=0.71%, as described in Figs. 1 and 2. We divided the supercell's first Brillouin zone into 10×10 grid, which for the irreducible part yields 66 different $\vec{k}$ points. For each particular disorder realization and disorder strength, we run the simulation for all these 66 $\vec{k}$'s. At each $\vec{k}$ however we use a different disordered configuration, and so a large statistical sample is automatically included in our result. In each case the effective disorder is measured by the rms error of the dielectric constant $< \epsilon >$, which is defined as [12, 4]

$$\epsilon^2 = \frac{1}{N}\sum_{i=1}^{N}(\epsilon_i^d - \epsilon_i^p)^2, \tag{4}$$

where the sum goes over all $N = 8\times8\times32\times32 = 65536$ grid points, ϵ_i^d and ϵ_i^p are the dielectric constants at site i in the disordered and periodic case respectively, and $< \ldots >$ means the average over different configurations (different $\vec{k}$'s in our case). In both settings (dielectric cylinders in air and *vise versa*) the filling ratio of the high dielectric material is similar, and so $< \epsilon >$ is expected to have the same meaning and weight.

Four different disorder realizations are studied: 1) disorder in position, without though allowing any cylinders to overlap with each other, 2) disorder in position allowing cylinder overlapping to occur, 3) disorder in radius, and 4) disorder in dielectric constant (the last one only in the solid cylinder case). For each different realization we consider various disorder strengths, and thus different effective disorders $< \epsilon >$, for which we record the upper and lower gap edges for the first two photonic band gaps (if they exist). Results are summarized in Figs. 5 and 6, for the solid and air cylinder cases respectively. We note that the E_z polarization case for the solid cylinders is very different from all other cases: the gaps survive very large amounts of positional disorder, especially if no overlaps are allowed. In fact, once the disorder becomes large enough for overlaps to be possible, the gap quickly closes, as shown in Fig. 5. The actual DOS graphs for the two different realizations of the positional disorder are shown in Fig. 7, for three different values of the effective disorder. On the other hand, if the disorder is of the third or fourth kind, the gaps close very quickly, even for modest values of the effective disorder.

The picture is very different in the other cases, as seen in Fig. 6. The effect of the positional disorder is the same, independent of whether overlaps are allowed or not. This is most clearly seen in Fig. 8, where the actual DOS graphs are plotted for the air cylinder case for both polarizations, and for both positional disorder realizations. Allowing the air cylinders to overlap, though, means that the connectivity of the background material will break. Our results, thus, indicate that there is no connection between the connectivity of the background material and the formation of the spectral gaps in this 2D case. Most importantly, however, we note that the disorder in radius has a similar effect with that of the positional disorder in closing the gaps. In fact, it is also similar to the effect of the disorder in radius for the E_z-solid-cylinder case. So, in the case of air cylinders, the type of the disorder that is introduced into the system does not play a significant role, but rather, it is only the effective disorder (measured through the dielectric constant's error function) that determines the effect on the spectral gaps. On the other hand, for the E_z-solid-cylinder case, the type of disorder plays a profound role: if the "shape" of the individual scatterer is preserved, the gaps can sustain large amounts of disorder, while if it is not preserved, the gaps collapse in a manner similar to the air cylinder case.

We next go over the localization length results, which were obtained with the transfer matrix technique. Here, our system consisted of a 3×7 supercell (3 along the x axis), with each cell discretized into a 18×18 grid (a small supercell was used in order to ease the computation burden). In the x direction we applied periodic boundary conditions, while in the y direction the supercell was repeated 4 times, to provide a total length L for the slab of L=28 unit cells. The structures studied are exactly the same as described before. The lattice was cut along one only symmetry direction, the (1,0), since for large disorders we expect all "hidden" modes to be coupled with the incident wave (in any case, we know from Figs. 3 and 4 which results can be completely trusted and which can not). For each disorder realization and strength, we used 11 different $\vec{k}$ values uniformly distributed between normal and 45^o angle incidence, and for each $\vec{k}$ we used a different disordered configuration, so these will constitute our statistical sample. For each $\vec{k}$ we find the minimum transmission coefficient inside each gap, from which we find the minimum localization length, and then average over all $\vec{k}$'s, ie. $\ell \sim -2L/ < \ln T >$ (in the periodic case we first averaged over T in order to correctly account for different propagation directions, but in the highly disordered case it is not so much important any more, and so we just average over the localization lengths).

Our results are shown in Figs. 9 and 10 (because of the small statistical sample and the small supercell used, the data points appear very "noisy", especially for large disorders). We note here, as well, the distinct difference between the E_z-solid-cylinder case for positional disorder and all other cases. Especially for the first spectral gap, the localization length not only remains unaffected by the disorder, but it even decreases (this is not an artifact of the averaging procedure). The first conclusion from this, is that the mechanisms responsible for the gap formation in this case are unaffected by the presence of positional disorder, and so they are definitely not macroscopic (long-range) in nature. The fact that the localization length decreases, is attributed to the coupling of more [1,1] symmetry modes with the incident wave as the disorder increases (they provide a smaller ℓ to the average, as seen in Fig. 3a). This decrease should not be mistaken for additional localization induced by the disorder (the classical analog of Anderson localization in electrons), since the latter is macroscopic in nature, and does not apply for strongly localized waves. The decrease in the localization length continues until a fairly large disorder value, and then it increases to a saturation value (the dielectric error function can reach only up to some value for positional disorder). This saturation value is higher for the case where overlaps are allowed, but still is very small compared to other cases, so waves remain strongly localized.

All other cases, on the other hand, show a common pattern of behavior: photon states become quickly de-localized with increasing disorder. The localization length is increased, until the point where the localization induced by the disorder becomes dominant. After this it starts decreasing, until finally it reaches some saturation point. Note also that there is an almost quantitative agreement between some cases that was not really expected, eg. for the disorder in radius in the first gap with the wave E_z-polarized, for both lattice settings, as seen in Figs. 9a and 10a. Only the case of disorder in the dielectric constant seems to deviate, having very quickly a very large effect, with the localization length directly saturating to some constant value. So, for air cylinders in dielectric with any type of disorder, and for the E_z-solid-cylinder case with disorder that does not preserve the scatterer's "shape", the behavior under disorder is similar.

All these results can be understood if we adopt two different "pictures" for the photon states, depending on which is the dominant mechanism that is responsible for the formation of the spectral gaps in each case. The first is the “nearly free” photon picture, in which the gap forming mechanism is the non-resonant macroscopic Bragg-like multiple scattering, while the second is the “strongly localized” photon picture, in which the gap forming mechanism is the microscopic (short-range) excitation of single scatterer Mie resonances.

Sharp Mie resonances appear only for the solid cylinder case, and they can be thought as analogous to the atomic orbitals in semiconductors. Using this analogy, a tight-binding model, based on a linear combination of Mie resonances, was recently developed for the photonic states in the E_z-solid-cylinder case [7]. But if a tight-binding model can give a satisfactory description of the photonic states, then it is expected that certain behavioral patterns found in semiconductors should apply in our case too. So, positional disorder should have a small effect on the gaps, in a similar way the energy gap survives in amorphous silicon. Also, changing the scatterer should have a similar effect as changing the atoms in the semiconductor, yielding a large amount of impurity modes that quickly destroys the gap. This pattern is definitely confirmed here for the E_z-solid-cylinder case. In this case, multiple scattering and interference can only help to make the gaps wider, but are definitely not decisive on the existence of a gap.

For the macroscopic Bragg-like multiple scattering mechanism, the lattice periodicity is a very important factor for the existence of a spectral gap. If it is destroyed, then coherence in the backscattered waves will be destroyed, and so will the spectral gaps. It is of small consequence the exact way that the periodicity is destroyed, and so different disorder realizations will have similar effects. Also, since the gaps close more easily, it will be easier to observe the localization induced on the waves by the disorder itself, ie. the classical analog of Anderson localization in electrons. All these are recognized in the case of air cylinders in dielectric.

Finally, in the H_z-solid-cylinder case, there were no gaps to begin with, and so we can have no results about it. However, sharp Mie resonances appear for this case as well, and if their excitation was the dominant scattering mechanism, a gap would be expected here as well. The difference with the E_z is that the former is described by a vector wave equation, while the latter by a scalar one (and thus closer to the electronic case). The form of the wave equation must, then, be an important factor in determining the relative strength of the two gap forming mechanisms.

Conclusions

We have shown that several results in periodic and random photonic band gap materials can be understood in terms of two distinct photonic states: (a) The "local" states, based on a single scatterer Mie resonance, with the multiple scattering playing a minor role; these states are more conveniently described in terms of an LCAO-type of approach and are the analog of the d-states in transition metals. "Local" photonic states appear in the case of high dielectric cylinders surrounded by a low-dielectric host and for E-polarized waves. (b) The "nearly free" photonic states, where Bragg-like multiple scattering is the dominant mechanism responsible for their appearance; these states are more conveniently described in terms of a pseudopotential-type of approach and are the analog of s (or p) states in simple metals.

Each type of photonic states responds differently to the presence of disorder: For the "local" states case, the gap is robust as the periodicity is destroyed, and it is hardly affected by the disorder as long as the identity of each individual scatterer is preserved; however, if the shape, or other characteristics influencing the scattering cross section of each individual scatterer, is altered by disorder, the gap tends to disappear. On the other hand, for the "nearly free" states case, the gap is very sensitive and tends to disappear easily as the periodicity is destroyed.

Acknowledgments

Ames Laboratory is operated for the U. S. Department of Energy by Iowa State University under contract No. W-7405-ENG-82. This work was supported by the Director of Energy Research office of Basic Energy Science and Advanced Energy Projects. It was also supported by a E.U. grant, a NATO grant, and a PENED grant.

Bibliography

[1] For excellent reviews on photonic band gap materials see the proceedings of the NATO ARW, *Photonic Band Gaps and Localization*, ed. by C. M. Soukoulis, (Plenum, N.Y.,

1993); *Photonic Band Gap Materials*, ed. by C. M. Soukoulis, NATO ASI, Series E, vol. 315.

[2] J. D. Joannopoulos, R. D. Meade, and J. N. Winn *Photonic Crystals* (Princeton University Press, Princeton, 1995).

[3] S. Fan, P. R. Villeneuve, and J. D. Joannopoulos, J. Appl. Phys. **78**, 1415 (1995).

[4] M. M. Sigalas, C. M. Soukoulis, C. T. Chan, and D. Turner, Phys. Rev. B **53**, 8340 (1996); M. M. Sigalas, C. M. Soukoulis, C. T. Chan, and K. M. Ho in *Photonic Band Gap Materials*, p. 563, ed. by C. M. Soukoulis (Kluwer, Dordrecht, 1996).

[5] S. Datta, C. T. Chan, K. M. Ho, C. M. Soukoulis, and E. N. Economou, in *Photonic Band Gaps and Localization* [Ref. [1](a)], p. 289.

[6] M. Kafesaki, E. N. Economou, and M. M. Sigalas, in *Photonic Band Gap Materials* [Ref. [1](c)], p. 143.

[7] E. Lidorikis, M. M. Sigalas, E. N. Economou, and C. M. Soukoulis, Phys. Rev. Lett. **81**, 1405 (1998).

[8] G. Mie, Ann. Phys. (Leipzig) **25**, 377 (1908); C. F. Bohren and D. R. Huffman, *Absorption and Scattering of Light by Small Particles* (J. Wiley, New York, 1983).

[9] K. S. Yee, IEEE Trans. Antennas and Propagation **14**, 302 (1966).

[10] Allen Taflove, *Computational Electrodynamics: The Finite-Difference Time-Domain Method* (Artech House, Boston, 1995).

[11] J. B. Pendry and A. MacKinnon, Phys. Rev. Lett. **69**, 2772 (1992).

[12] C. T. Chan, Q. L. Yu, and K. M. Ho, Phys. Rev. B **51**, 16635 (1995).

[13] Kazuaki Sakoda and Hitomi Shiroma, Phys. Rev. B **56**, 4830 (1997).

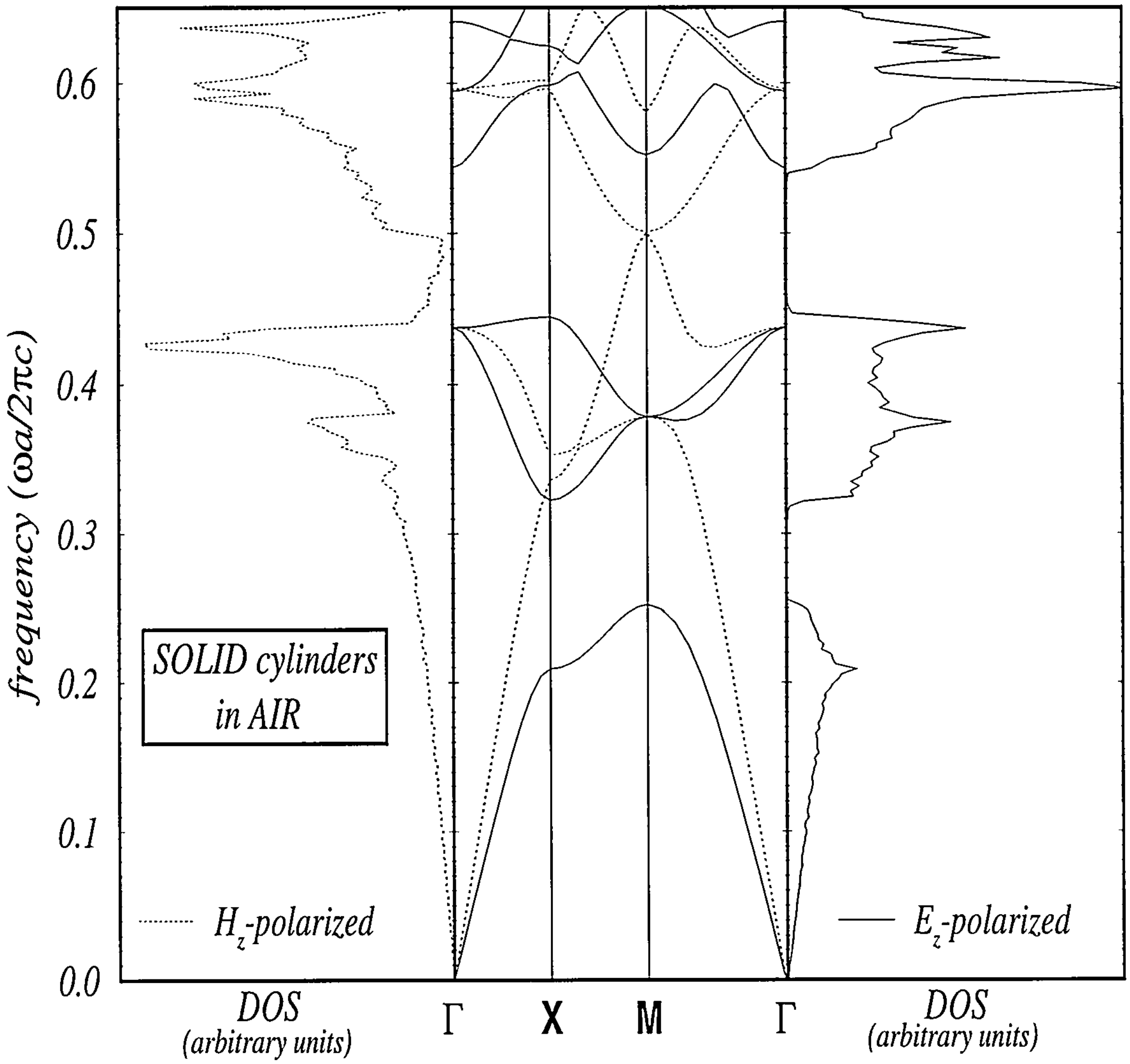

Figure 1 Band structure (obtained with a plane wave method) and density of states (obtained with the FDTD spectral method) for a two-dimensional square lattice array of dielectric cylinders ϵ_a=10 in air ϵ_b=1, with a filling ratio $f \simeq 28\%$.

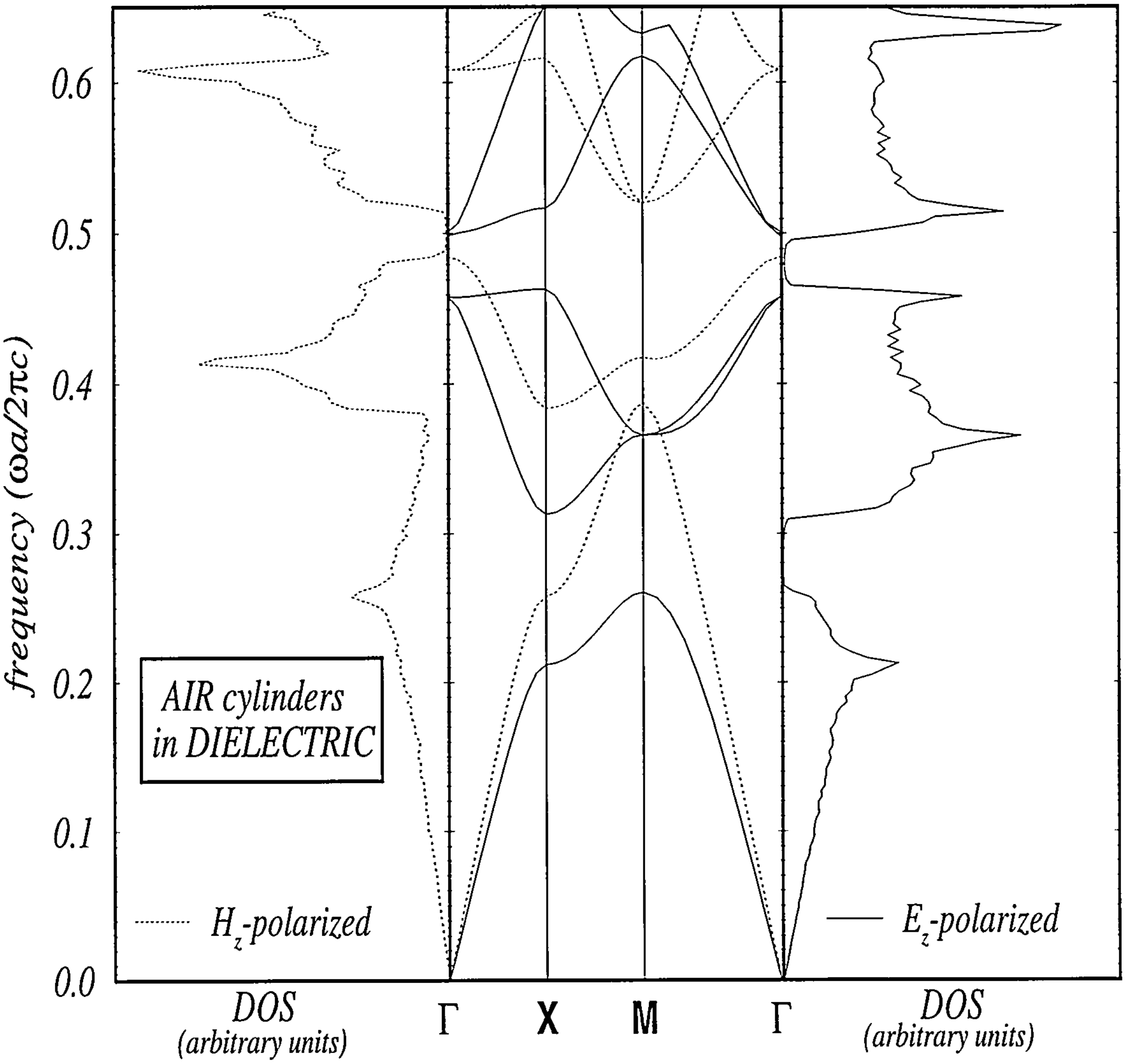

Figure 2 Band structure (obtained with a plane wave method) and density of states (obtained with the FDTD spectral method) for a two-dimensional square lattice array of air cylinders ϵ_a=1 in dielectric ϵ_b=10, with air filling ratio $f \simeq 71\%$.

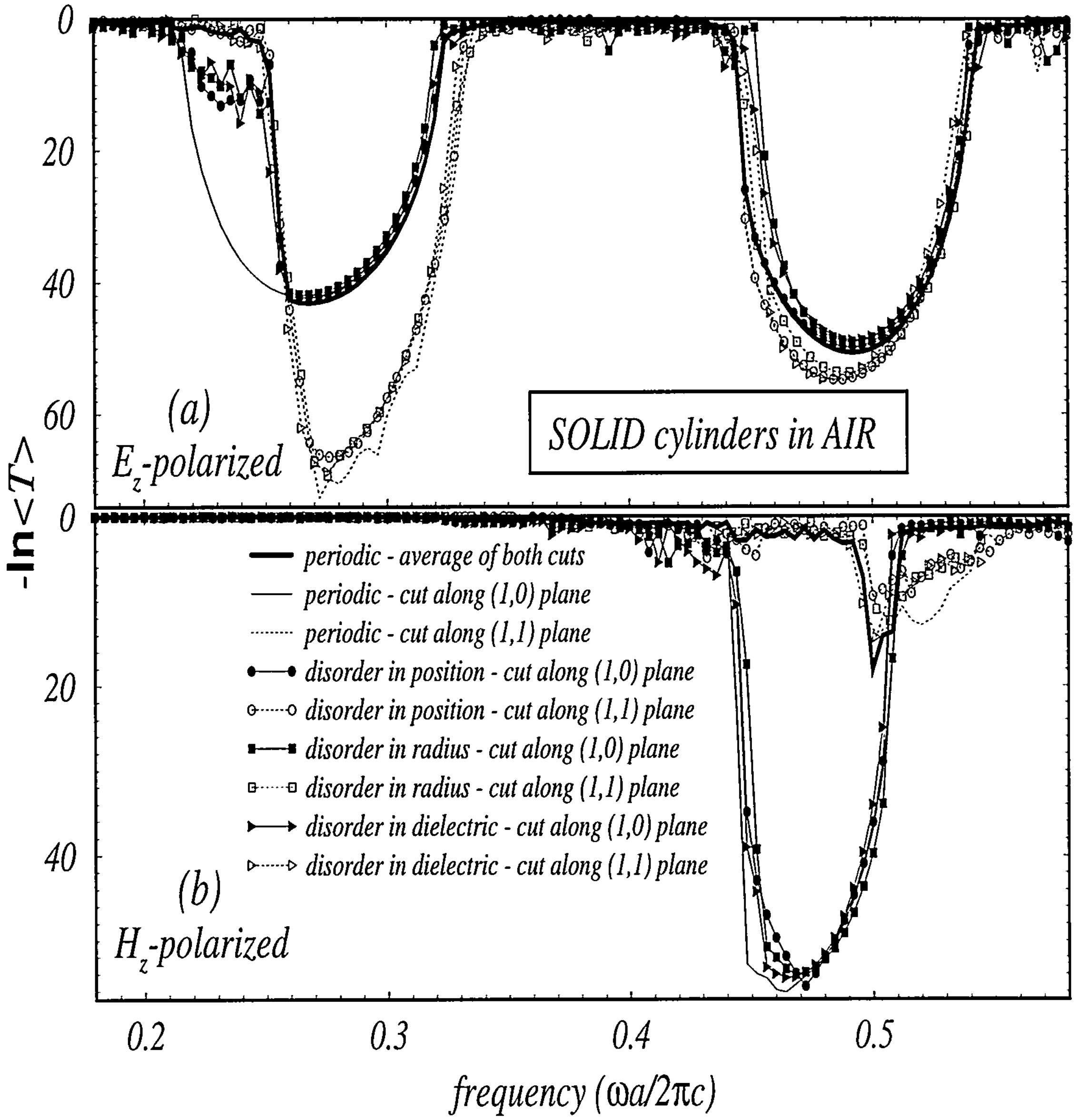

Figure 3 Transmission coefficient for the periodic, and weakly disorder, system described in Fig. 1 (obtained with the transfer matrix technique). Calculations are for two different surfaces along which the sample is cut. Effective disorders used (look Eq. (4)): in position∼1.3, in radius∼0.5, and in dielectric∼0.3.

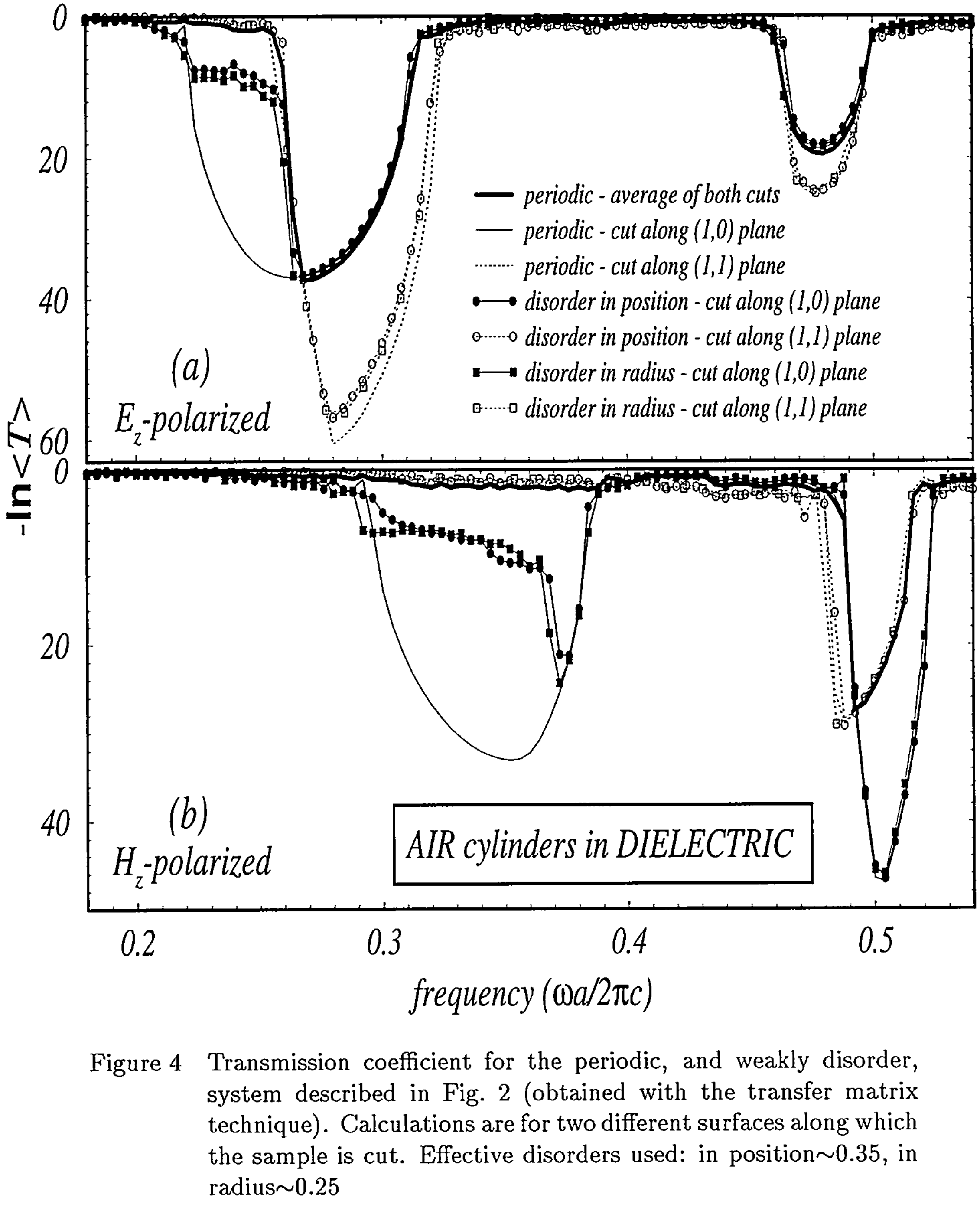

Figure 4 Transmission coefficient for the periodic, and weakly disorder, system described in Fig. 2 (obtained with the transfer matrix technique). Calculations are for two different surfaces along which the sample is cut. Effective disorders used: in position~0.35, in radius~0.25

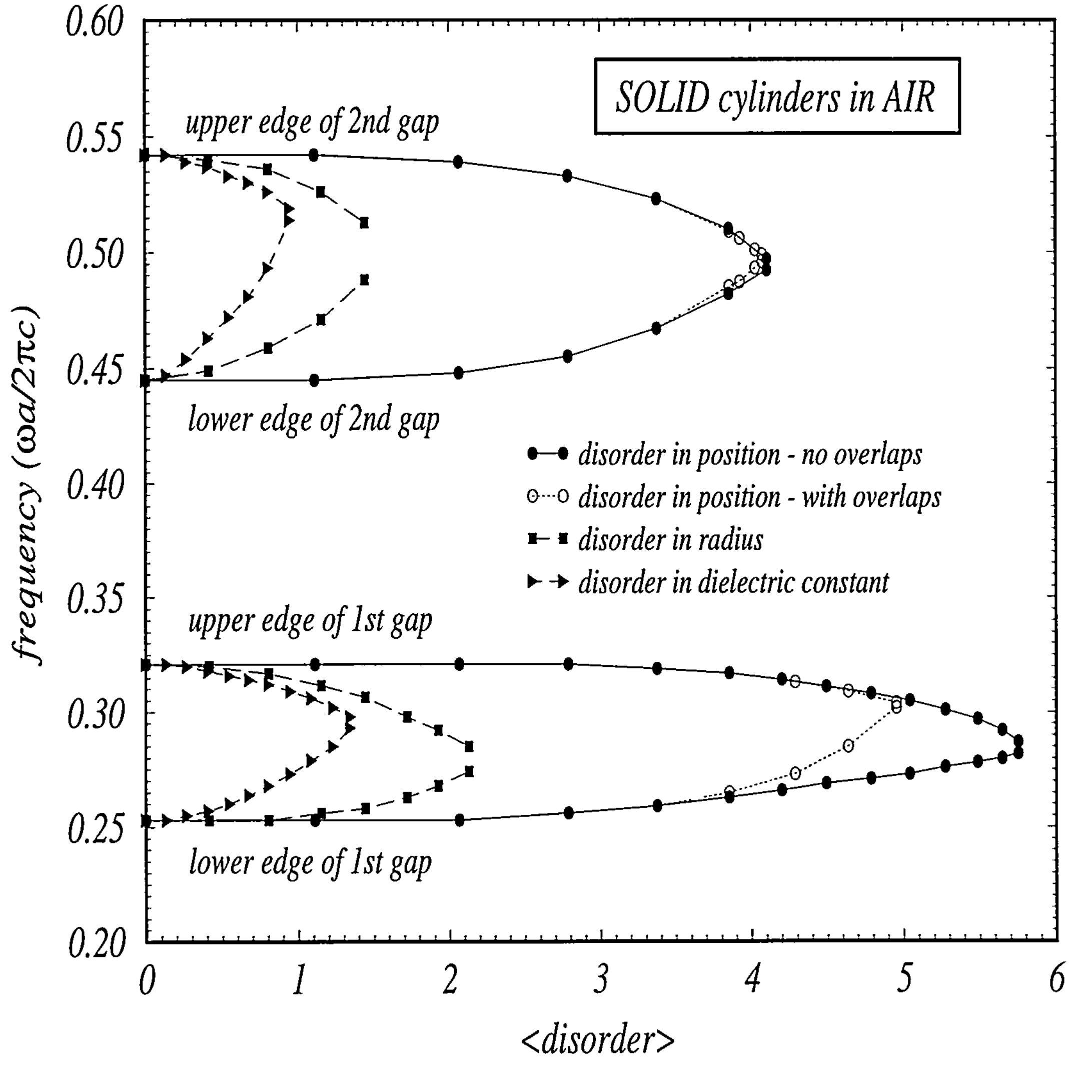

Figure 5 The edges of the photonic band gaps as a function of the effective disorder $< disorder > \equiv < \epsilon >$ (as was defined in Eq. (4)), for the system described in Fig. 1. Four different disorder realizations are studied.

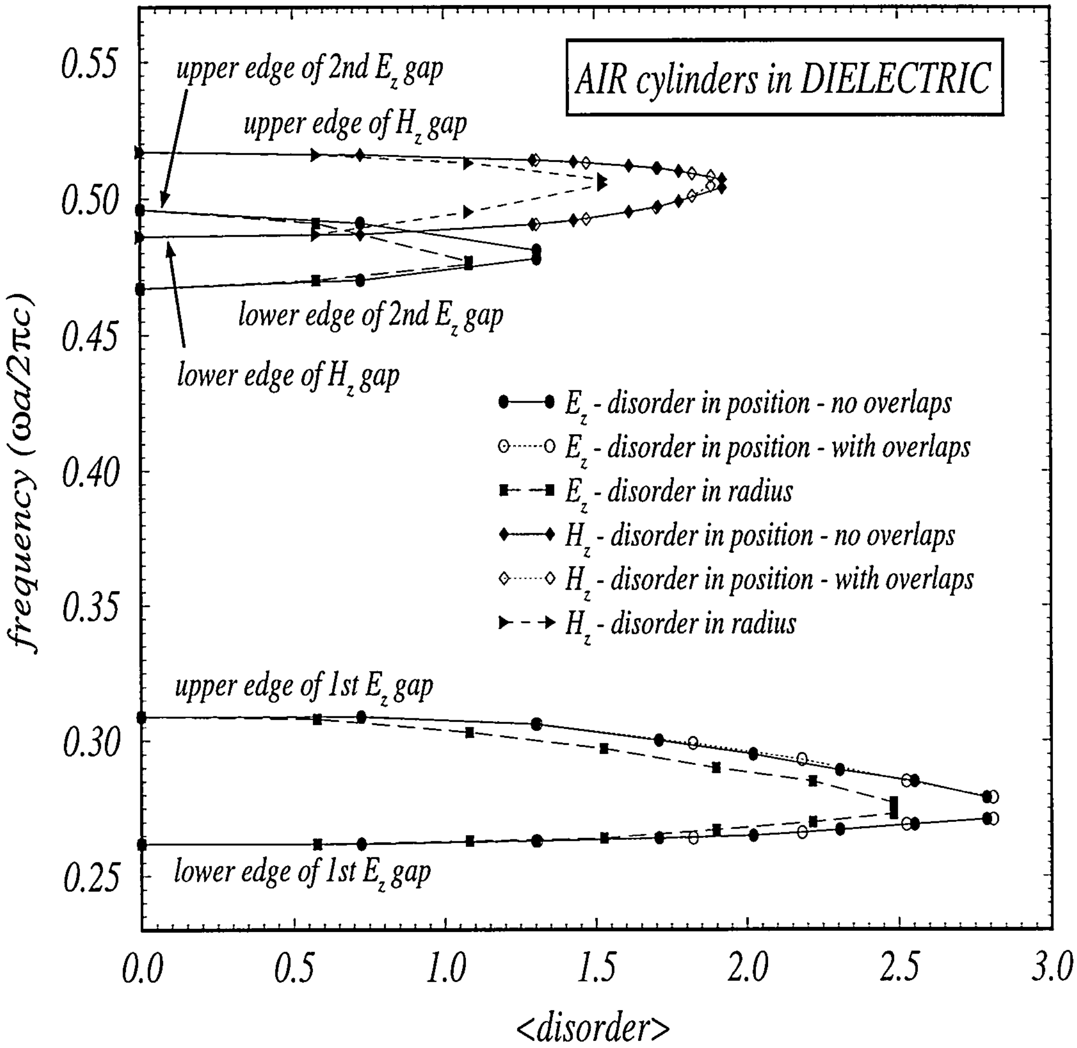

Figure 6 The edges of the photonic band gaps as a function of the effective disorder $< disorder > \equiv < \epsilon >$ (as was defined in Eq. (4)), for the system described in Fig. 2. Three different disorder realizations are studied.

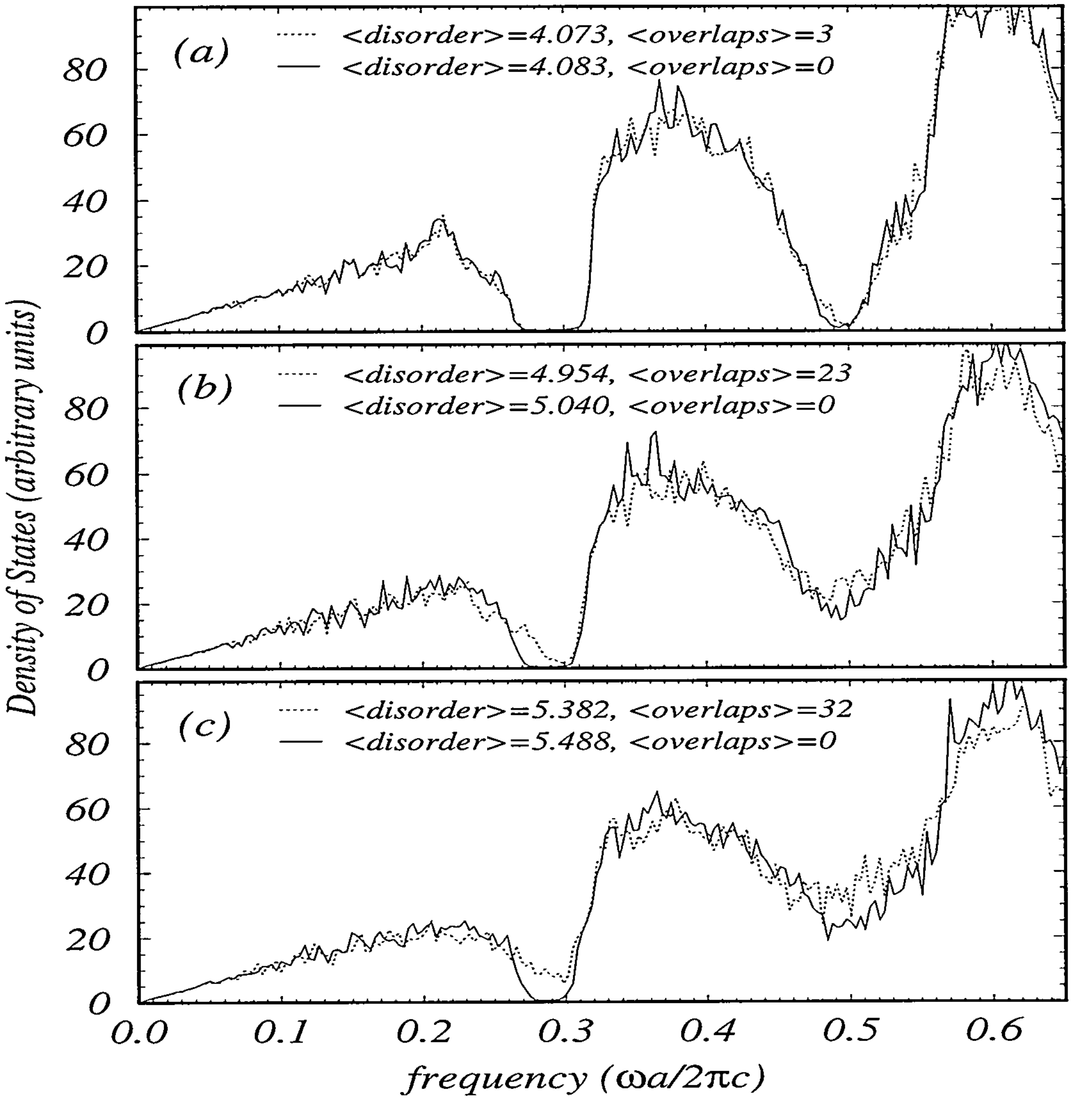

Figure 7 The density of states for the system of Fig. 1 with the E_z polarization, for three different positional disorder strengths. The solid line is when no scatterer overlaps are allowed, while the dotted line is when scatterer overlaps are allowed. $<$ *overlaps* $>$ is the average number of overlapping cylinders.

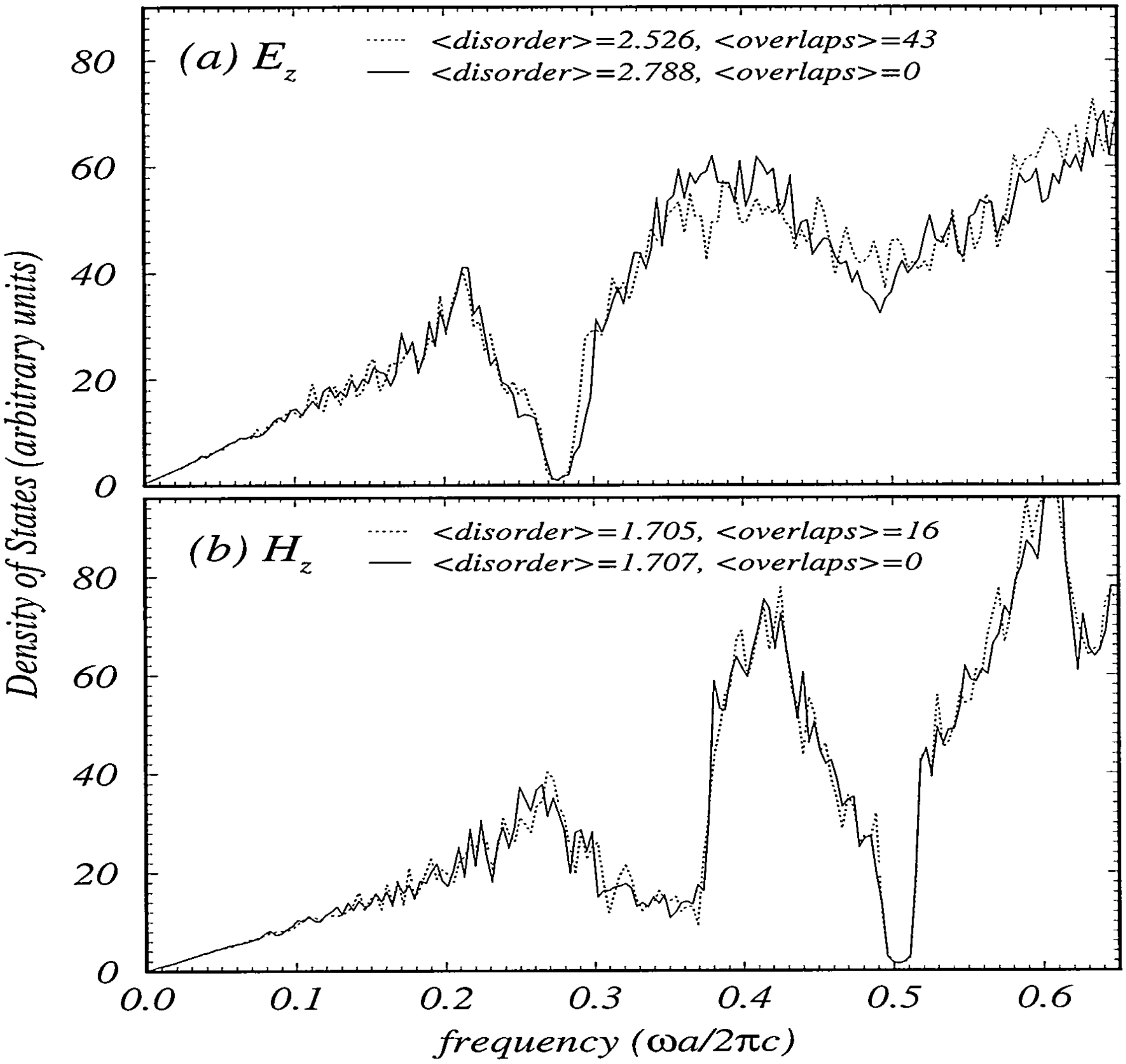

Figure 8 The density of states for the system of Fig. 2 for both field polarizations, for two different positional disorder strengths. The solid line is when no scatterer overlaps are allowed, while the dotted line is when scatterer overlaps are allowed.

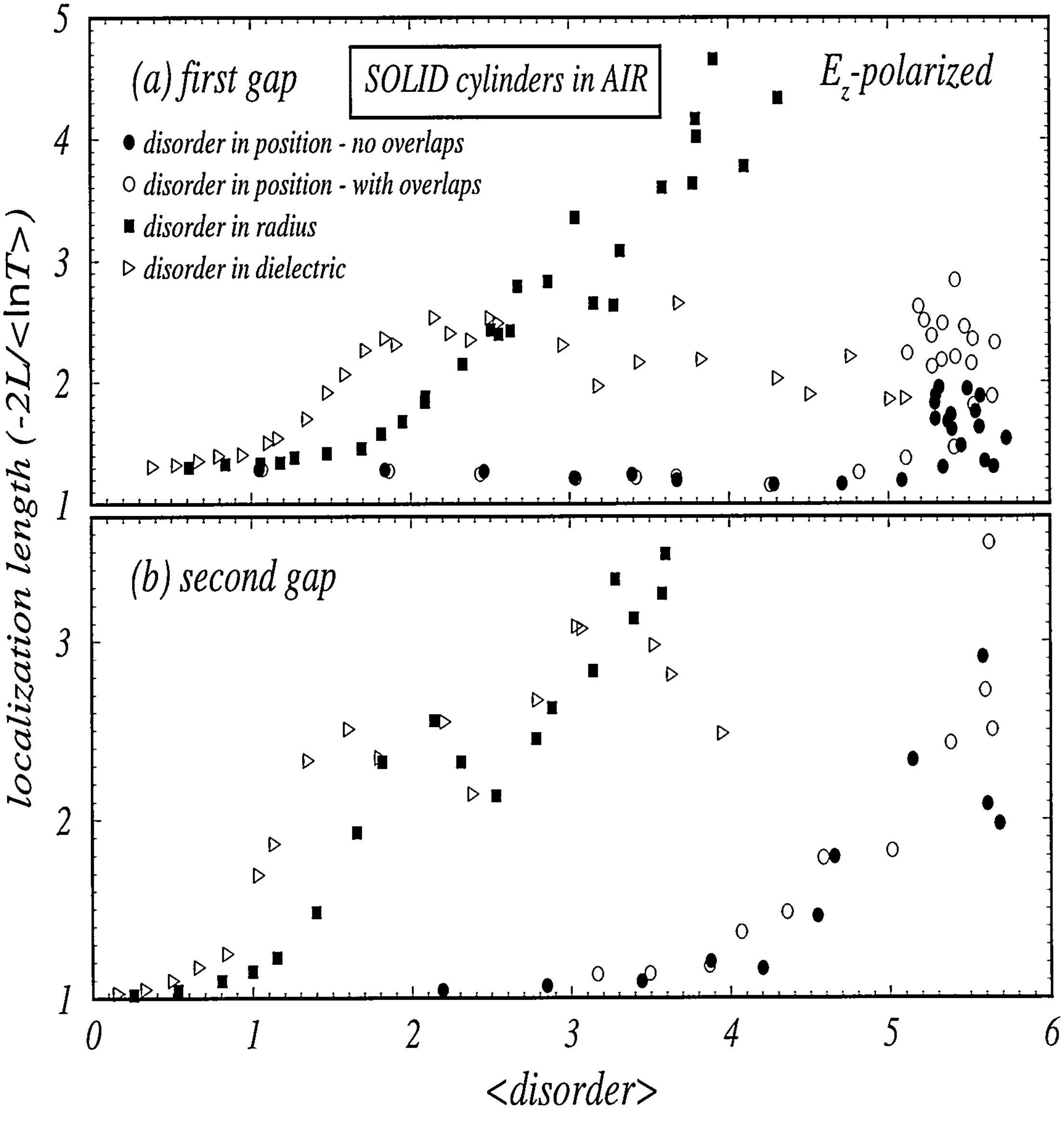

Figure 9 The localization length as a function of the effective disorder for the system described in Fig. 1 with the E_z polarization, for four different disorder realizations.

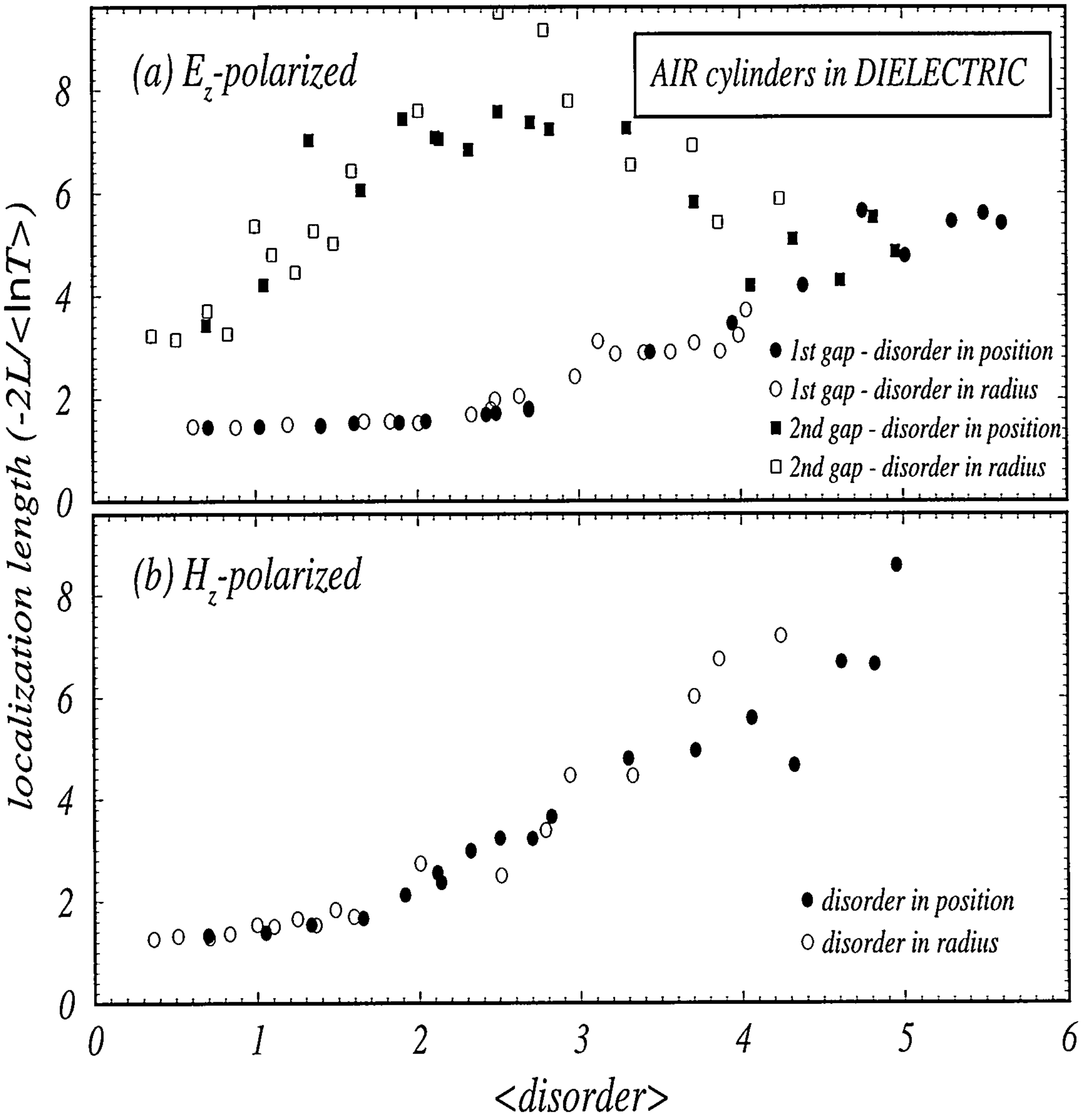

Figure 10 The localization length as a function of the effective disorder for the system described in Fig. 2 for both field polarizations, for two different disorder realizations.

CHAPTER 8. GENERAL CONCLUSIONS

Photonic band gap materials are artificial dielectric structures that give the promise of molding and controlling the flow of optical light the same way semiconductors mold and control the electric current flow. In this dissertation we studied two areas of photonic band gap materials. The first area is focused on the properties of one-dimensional PBG materials doped with Kerr-type nonlinear material, while, the second area is focused on the mechanisms responsible for the gap formation as well as other properties of two-dimensional PBG materials.

We first studied, in Chapter 2, the general adequacy of an approximate structure model in which the nonlinearity is assumed to be concentrated in equally-spaced very thin layers, or δ-functions, while the rest of the space is linear. This model had been used before, but it's range of validity and the physical reasons for it's limitations were not quite clear yet. We performed an extensive examination of many aspects of the model's nonlinear response and comparison against more realistic models with finite-width nonlinear layers, and we found that the δ-function model is quite adequate, capturing the essential features in the transmission characteristics. We found though one exception, coming from the deficiency of processing a rigid bottom band edge, ie. the upper edge of the gaps is always independent of the refraction index contrast. This causes the model to miss-predict that there are no soliton solutions for a positive Kerr-coefficient, something we know that it is not true.

In Chapter 3 we continued testing the δ-function model on an alternative arrangement in which the nonlinear material is concentrated in one only layer, surrounded by a lattice of linear layers. In this arrangement and for gap frequencies, bistability results not from gap soliton formation but, rather, from the nonlinear modulation of an impurity mode. Because of the very high-Q of the impurity mode, we can use frequencies very close to it, and so achieve switching with low input powers. For the δ-function model, we obtained a strictly-bistable cubic equation for the system's nonlinear response at any frequency, with normalized parameters that describe the experimental situation. Tested against realistic finite-width layer models, it is proven excellent, except for high input intensities, where the second deficiency of the δ-function model, it's strictly bistable nature, shows up. For higher input powers, a finite-width nonlinear layer generally exhibits multistability. We have obtained an analytic solution for the localized modes in the gap for a nonlinear impurity of finite extent in an otherwise linear dielectric superlattice, which shows this multistable behavior. Generally, besides the two exceptions found here and in Chapter 2, the δ-function model has proven it's usefulness by capturing the most essential features in the transmission characteristics of both systems, and should be widely used because of it's simplicity.

Next, in Chapter 4, we move into the time-dependent properties of one-dimensional nonlinear PBG materials for frequencies inside the gap of the corresponding linear structure. Here, we found that besides the steady-state solutions already found by time-independent methods, the system can go into self-pulsing and/or chaotic states as well. We studied the dynamics of driving the systems from one transmission state to the other by means of pulse injection, found relationships between the pulse, the stationary gap soliton, and the unstable solitary waves, and found the optimal pulse parameters for the switch to occur. A dependence on the initial phase difference between pulse and CW at injection time, sets a requirement for coherent beams if a fully controlled and reproducible switch is desired. Then we repeated all this work for the case of a nonlinear impurity inside a linear lattice, and found that the pulse can interact with the impurity mode as well and drive the system from one transmission state to the other. All restrictions found in the previous case, however, still apply in this one.

Finally, in Chapter 5, we studied a colloidal crystal that has a bistable response to intense radiation without, though, having any intrinsic type of nonlinearity. In order to explain the experimental results, we developed an one-dimensional approximate structure model, as well as an approximate model for the basic light-particle and particle-particle interactions, without any adjustable parameters. We ended up with a dynamical lattice-light coupling model, a classical analog of the electron-phonon coupling in semiconductors. This model successfully reproduced the experimental results, and thus has captured the nature of the nonlinear response of colloidal crystals.

Next, we go over to two-dimensional PBG materials. In Chapter 6, our goal was to stress the analogy between photons in a PBG structure and electrons in a semiconductor, and to show that in one particular case (solid dielectric cylinders in a low dielectric background and the wave polarized with it's electric field parallel to the cylinder's axis), the mechanism responsible for the gap formation is the excitation of single scatterer resonances and not macroscopic Bragg-like multiple scattering. Therefore, we developed a tight-binding model based on a linear combination of Mie resonances, and fitted it's parameters to *ab initio* results. With the incorporation of a free plane wave to account for the allowed small-frequency background propagation modes, and parameter rescaling to account for the large environment effect on the nearest neighbor matrix elements, the model could successfully reproduce the band structure for any lattice arrangement, with and without defects, and for two different dielectric constants, proving it's validity. Thus, the "strongly localized" photon picture, the analog of the atomic orbitals in semiconductors, has to be incorporated in the photonic band gap materials theory.

In Chapter 7 we studied the two photon pictures, the "nearly free" photon for which the gap forming mechanism is Bragg-like multiple scattering, and the "strongly localized" photon for which the gap forming mechanism is the excitation of single scatterer resonances. Using two *ab initio* numerical techniques, we studied the changes developed under disorder in the gap formation and wave localization, for four different settings (solid cylinders in air and *vise versa* for both wave polarizations). Results were generally classified into two groups attributed to the two photon pictures. Only the solid cylinder E_z-polarized case exhibited the behavior expected from the 'strongly localized" photon picture, while for all other cases, the "nearly free" photon picture seems to be the proper one.

To summarize, this dissertation has contributed the following in the study of photonic band gap materials: in one-dimensional nonlinear structures it showed, the adequacy of the δ-function model, the single nonlinear impurity layer in a linear superlattice as an optimal structure for low switching thresholds, the advantages and limitations of switching by means of externally injected pulses, and the nature and the dynamics of the nonlinear response of colloidal crystals; in two-dimensional photonic band gap materials it showed the existence of two different pictures for the photonic states, and their properties under disorder. One of the two pictures is in very close analogy with it's electronic counterpart, and a theoretical model, inspired from the ones used in electronic band theory, was developed for it. Possible directions for future work are, the study of the nonlinear switching dynamics in two-dimensional nonlinear photonic band gap materials and how the two different photon pictures would enter, extensive study of disorder, impurity states, surface states etc. using the newly developed model in two-dimensional photonic band gap materials, and the development of a similar model (if applicable) for three-dimensional photonic band gap materials.

ACKNOWLEDGMENTS

With great pleasure, I would like to express my deepest gratitude to my academic advisor, Prof. Costas M. Soukoulis, for his inspiration, guidance, and constant encouragement throughout my Ph.D studies, as well as for all the excellent opportunities he offered me.

I would also like to express my gratitude to all of those who helped make this work possible:
My committee members, Profs. Bruce N. Harmon, Constantine Stassis, Kerry Whisnant, and Gary Tuttle. Especially Prof. Harmon for all the opportunities he made possible for me.
Prof. Constantine Stassis, for being a constant stimulus and inspiration, both as a physicist and as a man, throughout my Ph.D years.
Prof. Elefterios N. Economou, for his physical insight and many illuminating discussions and suggestions, as well as for his hospitality in the research center of Crete in Greece.
Dr. Qiming Li, whom I think of as a second advisor, for his physical insight and guidance, and for the excellent opportunities he offered me.
Dr. Kurt Busch, for an excellent collaboration and many illuminating discussions, as well as for carrying out most of the work in the second part of chapter 3.
Dr. Michael Sigalas, for an excellent collaboration and many illuminating discussions, as well as providing some of the computer programs used in this work.
The older Greek Ph.D students, Drs. Athan Petridis, George Kopidakis, Vassilis Charmandaris, and Dimitris Kouzoudis, who helped me in a number of ways.

Finally, I would like to express my gratitude to those who emotionally held me all these years:
My wife, Irene Karantzeni, for her love, inspiration, and support.
To my parents, Stathis and Christina, for without their inspiration and support I would never

be here now. This dissertation is dedicated to them.

This work was performed at Ames Laboratory, which is operated for the U.S. Department of energy by Iowa State University under contract No. W-7405-Eng-82. The United States government has assigned the DOE Report number IS-T 1890 to this thesis.